Summer 2001

Detection of vapor phase mercury species by laser fluorescence methods

Xiaomei Tong
New Jersey Institute of Technology

ABSTRACT

DETECTION OF VAPOR PHASE MERCURY SPECIES BY LASER FLUORESCENCE METHODS

by
Xiaomei Tong

Elemental and compound mercury are often both volatile and air stable. Several mercury species emissions have been identified in off-gases from industrial processes. The high toxicity of mercury species and the presence of mercury species in municipal waste and coal have prompted a demand for a cost-effective, accurate, and rugged technique for real-time, continuous detection of mercury species vapors. Real-time, continuous emission measurements are important for process control, monitoring, and remediation. At present, there is no commercial continuous emission monitoring (CEM) technique or instrumentation to reliably monitor volatile mercury species emissions from industrial stacks. Conventional measurement methods, such as cold vapor trap based techniques for elemental mercury, have difficulty in achieving both high sensitivity and the fast time resolution required for real-time monitoring.

This doctoral research work gives a systematic study of potential methods for real-time trace detection of volatile elemental mercury and mercury compounds in industrial stack gases. It is based on laser-induced fluorescence techniques; photofragment fluorescence spectroscopy for detection of volatile mercury compounds, and resonance fluorescence for detection of elemental mercury. The capabilities and limitations of these detection techniques are investigated in this dissertation.

Detection of mercury compounds is a challenge since they are non-fluorescent. With photofragment fluorescence spectroscopy, target compound concentrations are related to the fluorescence intensity from an excited fragment. In this doctoral research

work, low concentrations of mercuric bromide vapor in an atmospheric pressure flow cell are irradiated by a focused laser beam at 222nm. Photofragment fluorescence is monitored at 253.7nm. Two detection schemes, Charge Coupled Device (CCD) and photomultiplier tube (PMT), are applied for the measurement of photofragment fluorescence. The performances of these two systems are compared in the dissertation.

A supersonic jet is combined with resonance fluorescence for detection of elemental mercury vapor. With test gas expanded into a vacuum, fluorescence quenching and spectral broadening are reduced. In the experiment, the gas jet is crossed with a laser beam at 253.7nm to excite atomic fluorescence, which is distinguished from the elastic background by time gating. The performance characteristics of this measurement technique, including limit of detection, range of linearity, relative accuracy, and response time, are investigated.

In addition, an ultraviolet (UV) interferometer is presented in this dissertation as a spectral discriminator for detection of Hg resonance fluorescence from elastic background. Its capabilities and limitations are discussed. A few suggestions regarding improvement on the current experimental system and measurement techniques for industrial applications of mercury detection are addressed.

DETECTION OF VAPOR PHASE MERCURY SPECIES BY LASER FLUORESCENCE METHODS

by
Xiaomei Tong

A Dissertation
Submitted to the Faculty of
New Jersey Institute of Technology
and Rutgers, the State University of New Jersey - Newark
In Partial Fulfillment of the Requirements for the Degree of
Doctor of Philosophy in Applied Physics

Federated Department of Physics

August 2001

APPROVAL PAGE

DETECTION OF VAPOR PHASE MERCURY SPECIES BY LASER FLUORESCENCE METHODS

Xiaomei Tong

Dr. Robert B. Barat, Dissertation Advisor — Date
Associate Professor of Chemical Engineering , NJIT

Dr. John Federici, Committee Member — Date
Associate Professor of Physics, NJIT

Dr. Anthony M. Johnson, Committee Member — Date
Distinguished Professor of Physics
Chairperson of Physics Department, NJIT

Dr. Daniel E. Murnick, Committee Member — Date
Professor of Physics, Rutgers University, Newark, NJ

Dr. Arthur T. Poulos, Committee Member — Date
President, Optomechanical Enterprise Inc., Allentown, NJ

BIOGRAPHICAL SKETCH

Author: Xiaomei Tong

Degree: Doctor of Philosophy

Date: August 2001

Undergraduate and Graduate Education:

- Doctor of Philosophy in Applied Physics
  New Jersey Institute of Technology, Newark, NJ, 2001

- Master of Science in Optics
  Zhejiang University, Hangzhou, Zhejiang, P.R.China, 1993

- Bachelor of Science in Physics
  Hangzhou Teacher's College, Hangzhou, Zhejiang, P.R.China, 1990

Major: Applied Physics

Presentations and Publications:

X. Tong, R. Barat, A. Poulos,
"Ultraviolet interferometric spectroscopy for real-time detection of elemental mercury" Proceeding of SPIE (International Society for Optical Engineering), Optical Methods for Industrial Process, vol.4201, 2000.

X. Tong, R. Barat, A. Poulos,
"An Ultraviolet interferometer for mercury resonance fluorescence detection", Ninth Annual Uni-tech Conference, April 28, 2000, Newark, NJ.

X. Tong, R. Barat, A. Poulos,
"A CCD based laser photofragment fluorescence spectrometer for detection of mercury compounds", Review of Scientific Instrument, vol. 70, 4180, 1999.

X. Tong, R. Barat, A. Poulos,
"Real-time trace detection of vapor phase elemental mercury and its compounds", Proceedings of SPIE, Environmental Monitoring and Remediation, vol. 3853, 162, 1999.

X. Tong, R. Barat, A. Poulos,
"Detection of Mercuric Bromide in a gas phase flow cell by laser photo-fragment fluorescence spectroscopy", Environmental Science and Technology, vol. 33, 3260, 1999.

X. Tong, R. Barat, A. Poulos,
"Detection of Low Levels of Mercury Species by Laser Fluorescence Methods", 32nd American Chemical Society Middle Atlantic Regional Meeting, May 17-19,1999, Madison, NJ.

X. Tong, L. Cheng, Y. Wang,
"Effect of Si-substrate heating during laser-induced B-doping", Applied Physics A, vol. 59, 189, 1994.

Y. Qian, X. Tong,
"Computer modeling of laser induced boron doping", Chinese J. Quantum Electronics, vol. 11, No. 2, 21, 1994.

X. Tong, L. Cheng, Y. Wang,
"The electronic properties of PN junction made by laser induced Boron doping in silicon". Chinese Proceedings of Eighth National Conference on IC and Si materials, 130, 1993.

To my beloved husband, daughter and parents

ACKNOWLEDGMENT

I would like to express my deepest appreciation to Dr. Barat Robert, who not only served as my research advisor, providing valuable and countless resource, insight, and intuition, but also constantly gave me support, encouragement, and reassurance.

Special thanks are given to Dr.Poulos, who spent a lot of time with me in the laboratory. The experimental skills I learned from him are very precious to me. I am also highly thankful to his constant guidance in my research work.

Appreciation is also extended to Dr.Murnick who always gives me helpful advice when I have tough problems in doctoral research. Special thanks to Dr.Federici and Dr. Johnson for active participation and guidance.

I would like to thank the EPA for providing financial support to the most of research work. My parents deserve my appreciation. They are the constant source of inspiration and encouragement. I thank my husband and our daughter who make me happy every day.

TABLE OF CONTENTS

TABLE OF CONTENTS
(Continued)

TABLE OF CONTENTS
(Continued)

TABLE OF CONTENTS
(Continued)

Chapter **Page**

LIST OF TABLES

LIST OF FIGURES

LIST OF FIGURES
(Continued)

LIST OF FIGURES
(Continued)

LIST OF FIGURES
(Continued)

LIST OF FIGURES
(Continued)

CHAPTER 1

INTRODUCTION

1.1 Background Information

1.1.1 Environmental Concern Over Mercury Emissions

Mercury (element and compounds) pollution emissions are major hazardous air pollutants. It is of particular concern since elemental and compounded mercury have high vapor pressures even at room temperature, and they are known toxins. Long-term (chronic) exposure to mercury can cause loss of muscle control and kidney disease. Some mercury compounds have chronic and acute toxic effects associated with central nervous system disorders [2].

Atomic mercury and selected mercury compounds (e.g. $HgCl_2$ and $Hg(CH_3)Cl$) have been identified in significant quantity during fuel and waste combustion in various industrial processes [1]. The high volatility of these species results in poor mercury species capture in fly and bottom ash. Since the form of the mercury emission will vary with coal composition and combustor operation, any control strategy for lowering total mercury emissions should be based on measurements of both atomic and compound vapor forms.

The US Public Health Service (USPHS) has put forth standards that Maximum Allowable Concentrations (MAC) of atmospheric organic (compound) mercury vapor should not exceed 10 microgram/cubic meter ($\mu g/m^3$) and elemental mercury vapor should not exceed 50 $\mu g/m^3$ [2]. However, generally the total mercury emitted from incinerator ranges from 10-2000 $\mu g/m^3$ and averages about 17 $\mu g/m^3$ [3]. Therefore,

monitoring and control of mercury species emissions in industrial environments are very important tasks.

1.1.2 Importance of Mercury Species Detection in Real-time

The best technology for mercury detection at present uses a collection/concentration step followed by off-line analysis using cold vapor atomic absorption [4-6] or cold vapor atomic fluorescence [7,8]. These methods depend on pre-concentration of the mercury cold vapor onto an absorbent trap of some type, generally for periods of 2 to 6 hours. This is usually followed by subsequent analysis in a laboratory. Absorbents used have included iodized carbon, gold-coated sand and gold-coated quartz wool, gold foil, etc. Some of these techniques have achieved limits of detection in the 10 parts per quadrillion with the pre-concentration step.

The per-concentration step usually required for very high limits of detection can result in significant time lags for emission monitoring. Such lags can hinder any type of emission control strategy. Thus, it is of great interest to develop techniques for real-time or near real-time analysis of emissions of mercury species from industrial stacks. The development of such techniques would constitute a real victory for regulation compliance and industrial process control. With real-time monitoring feature, feedback or feedforward process control of mercury species emissions can proceed with less delay.

Conventional technologies for detection of mercury compounds generally use non-spectroscopic method, such as Mass Spectrometry (MS) and Gas Chromatography (GC). In order to improve detection limit, these techniques sometimes are combined with Cold Vapor Atomic Absorption (CVAA) or Atomic Absorption Spectroscopy (AES) [59, 60].

Among the spectroscopy techniques for GC, Inductively Coupled Plasma Emissions (ICP) and Direct Current Plasma (DCP) emissions have been widely reported [2, 61]. In MS or GC techniques, mercury compounds are first gone through sample preparation and separation procedures, then are converted into mercuric ions/atoms for measurements. Based on these methods, real-time speciation of different mercury compounds becomes impossible. The speciation of mercury compounds in the environment where they are generated is important since the toxicity varies with chemical composition. The need to monitor of both elemental mercury and mercury compounds (all toxic) motivates this research.

1.1.3 Candidate Techniques for Real-time, On-line Monitoring

Direct optical techniques are very attractive since they offer the opportunity of continuous, in-situ, real-time measurements. Advanced laser-based techniques, unlike other existing emission monitoring technologies, offer a new alternative for real-time gas analysis and emission control. These techniques are usually nonintrusive and can have excellent sensitivity and selectivity with no source-to-analyzer time lag, which in turn will much improve process control.

Differential absorption LIDAR (Light Detection And Ranging) has been successfully employed for real-time remote monitoring of atmospheric atomic mercury in recent years by H. Edner et al [9]. In their work, a dye laser followed by frequency doubling produces very narrow laser radiation at 253.7 nm, which is the strongest emission line of atomic mercury. By measuring the decrease in the LIDAR signal over a 300-m path while scanning the laser slowly over the Hg line, they achieved Hg detection

sensitivity as low as 20 nanograms/cubic meter. However, a mature technology for on-line, real-time local (in-situ) monitoring of both mercury and mercury compounds in stack off-gas from waste incinerators and power plants, the common sources for mercury pollutant emissions, is not available.

Potential laser based methods for real-time monitoring include absorption, fluorescence, and plasma emission spectroscopy. To be useful to a wide range of applications, an instrument should be capable of detecting Hg in the range of 1-5000 $\mu g/m^3$ [10], with an ultimate sensitivity limit on the order of 0.1 $\mu g/m^3$ (10 ppt). However, atomic absorption requires very long path lengths to achieve the required sensitivity. Plasma emission spectroscopy is not suitable for mercury compound speciation as all parent mercury compounds are converted to excited mercury atoms in the intense plasma. Thus, due to its better sensitivity, specificity and linearity, laser based fluorescence spectroscopy is the preferred method used here for real-time monitoring purpose.

1.2 A Brief Review of Laser Fluorescence Spectroscopy

1.2.1 Definition of Fluorescence Phenomena

An atom/molecule in an excited state does not remain in that state indefinitely. It will eventually drop to a state of lower energy, even in the absence of any field or other atoms/molecules. This is known from experiments in which collisions are very infrequent, and each atom is effectively free of any external influence. Often associated with this decay of an excited state is the spontaneous emission of a photon. Fluorescence refers to spontaneous emission from an excited state produced by the absorption of light.

In fluorescence spectroscopy, a light source with narrow spectral bandwidth is brought into resonance with a spectroscopic transition to an electronically excited level whose spontaneous radiative decay provides the signal to be observed.

As depicted in Figure 1.1, fluorescence is best viewed as an absorption, followed after some finite period of time, by spontaneous emission from the excited states. The fluorescence observed may not be from the directly pumped upper state. If the fluorescence is at the same wavelength as the excitation, it is termed resonance fluorescence. With laser as strong excitation light source, fluorescence intensity can be increased significantly.

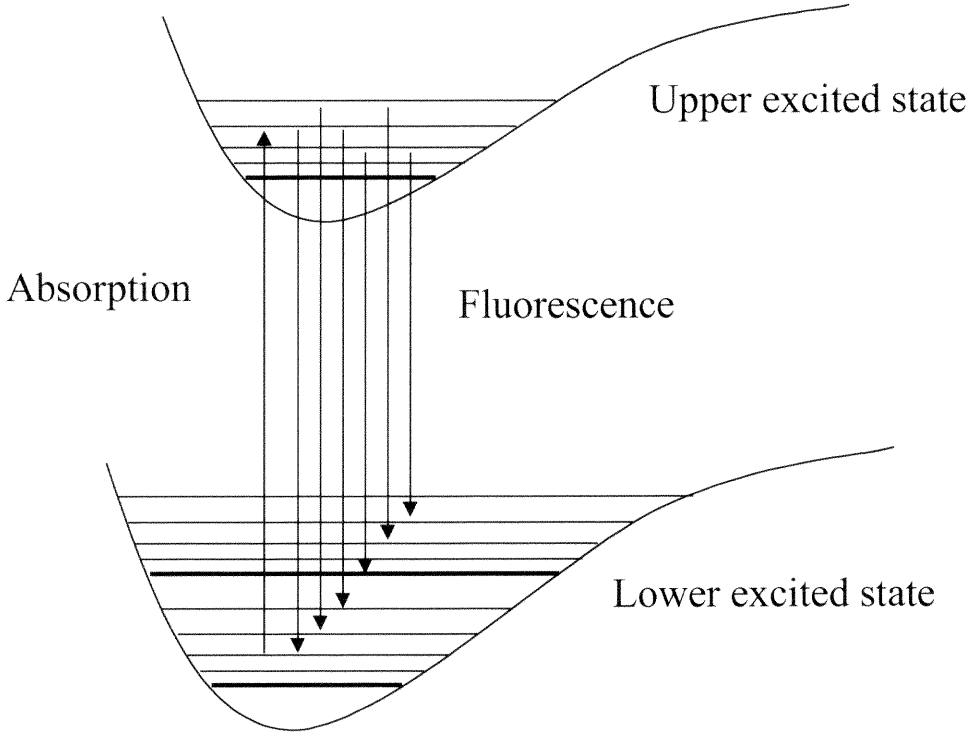

Figure 1.1 Diagram of fluorescence. Shown are schematic potential energy curves for lower and upper electronic states with vibrational (heavy) and rotational (light) energy levels. Fluorescence is a two-step process, an absorption (heavy upward arrows) followed by spontaneous emission (light downward arrows) [11].

1.2.2 Principles of Photofragment Fluorescence (PFF) Spectroscopy

The photofragment fluorescence (PFF) approach is most often utilized when the analyte molecule does not lend itself to direct spectroscopic detection [15]. In general, atoms and small molecules (e.g. diatomic and even some triatomic species) can be detected directly by absorption, fluorescence or photoionization techniques. This is due to a favorable combination of usually strong optical transitions and sharp, well-resolved spectral features that provide effective optical selectivity. However, it is often the case for larger molecules that the transitions are weaker and the spectral features are broad and poorly defined. In these cases, direct detection of the molecule by any of the above techniques is not analytically practical.

Where direct molecular detection may not be feasible, the photofragmentation products of polyatomic molecules are often monatomic and diatomic species which can be detected with relatively high levels of sensitivity. Furthermore, the photofragments are characteristic of the chemical composition of the precursor molecule (analyte) and contribute to the selectivity of the analytical methods.

In PFF spectroscopy, a photolyzing ultraviolet (UV) light beam is used to dissociate the target molecule into fragments, some of which are imparted with excess energy (step1). The energy might then be lost by fluorescence (step 2):

$$ML_n + h\nu \rightarrow (ML_{n-1})^* + L \quad (1.1)$$

$$(ML_{n-1})^* \rightarrow ML_{n-1} + h\nu' \quad (1.2)$$

In this representation, ML_n stands for a metal compound, M is the metal, L is a ligand, $h\nu$ is the incident photon energy and $h\nu'$ is the energy of the fragment fluorescence photon.

Photo-fragment fluorescence is a general phenomenon, applying to non-metallic inorganic and organic compounds as well.

Energetically, the following condition holds:

$$h\nu = E_{diss} + h\nu' \tag{1.3}$$

where E_{diss} is the dissociation energy per molecule.

In the case of metal compounds, fragmentation all the way down to the metal atom has been observed:

$$ML_n + h\nu \rightarrow M^* + nL \tag{1.4}$$

$$M^* \rightarrow M + h\nu' \tag{1.5}$$

This can occur by either of two methods: 1) The energy of a single photon (in the deep UV, i.e. below 200nm) may exceed the sum of all bond energies. Or, 2) Under high intensity conditions (a Q-switched pulsed laser or focused pulsed flash lamp), additional fragmentation is possible through absorption of UV photons by the initial fragments while they remain in the light field.

1.2.3 Quenching Theory

However, as in any fluorescence (resonance, PFF, etc.) method, a quenching effect may exist. Quenching refers to a nonradiative de-excitation. This takes place when excited atoms or molecules collide with other atoms or molecules, then decay to lower energy states, without emission of a photon. Collisional quenching leads to a loss of fluorescence signal.

The fluorescence quantum yield ϕ_f is introduced to describe the efficiency of fluorescence emission. It is usually unity in the absence of collisonal quenching. The rate constant k for decay of the excited species is defined [12]

$$k = \tau^{-1} = k_{rad} + k_{nonrad} \tag{1.6}$$

$$k_{rad} = \tau_r^{-1} \tag{1.7}$$

where k_{nonrad} stands for the rate constant associated with the nonradiative decay (collisional quenching here), k_{rad} is the fluorescence rate constant in the absence of a quencher, τ is the measured lifetime of the excited state, τ_r is the natural fluorescence lifetime of the excited state in the absence of a quencher. The rate constant is applied to the rate of population change of the expected level:

$$\frac{dN^*}{dt} = -kN^* \tag{1.8}$$

where N* is the population of the species in the upper state.

The fluorescence quantum yield ϕ_f is defined as following:

$$\phi_f = k_{rad}\tau = \frac{k_{rad}}{k_{rad} + k_{nonrad}} \tag{1.9}$$

Generally, collisional quenching of electronically excited species (i.e. fluorescence quenching) in the gas phase plays an important role in LIF. The kinetics of electronic quenching is described by the well-known Stern-Volmer relationship [12]. Including quenching, the rate constant for the decay of fluorescence can be expressed as

$$k = k_{rad} + \sum_i (k_q)_i [Q_i] \tag{1.10}$$

where k_q are the bimolecular quenching rate constants, i stands for the various collision partners, and $[Q_i]$ are their number concentrations.

For a simple case where only one quencher is present, fluorescence lifetime can be expressed easily by dividing Eq.1.10 by k_{rad} and using Eqs.1.6, 1.7 to get:

$$\frac{\tau_r}{\tau} = 1 + k_q \tau_r [Q] \tag{1.11}$$

The most commonly encountered form of Stern-Volmer relationship is [12]

$$I_q = I_0 \phi_f \tag{1.12a}$$

$$\frac{I_0}{I_q} = 1 + k_q \tau_r [Q] \tag{1.12b}$$

where I_0 is the fluorescence intensity of zero quencher, I_q is the fluorescence intensity in the presence of quenching gas.

Efficiencies of electronic quenching and energy transfer are commonly expressed by the collisional cross-section σ_q^2. The relationship between the collisional cross-section and the quenching rate constant k_q is [12]:

$$k_q = \sigma_q^2 \nu \tag{1.13}$$

$$\nu = (\frac{8kT}{\pi\mu})^{\frac{1}{2}} \tag{1.14}$$

where ν is the center-of-mass rms thermal velocity, k is Boltzmann constant, μ is the reduced mass of the collision pair and T is the absolute gas temperature. Open-shell species such as O_2, NO, NO_2 and other radicals quench fluorescence very efficiently. This is the main reason LIF techniques are not generally considered very promising under ambient atmospheric conditions.

1.2.4 Sensitivity of Fluorescence Detection

The detection of fluorescence against a background of zero or low levels of scattered light is intrinsically much more sensitive than the direct measurement of absorbed light. Using laser light as an intense excitation source can potentially increase the sensitivity of the fluorescence technique, which is of particular importance to the measurement of chemical vapor at low concentrations (ppb level).

The fluorescence process can be used for accurate quantitative determinations. The intensity of the fluorescence radiation is proportional to the intensity of the absorbed radiation. In simplicity (single-photon excitation, two-energy level system, low excitation irradiances), the fluorescence signal intensity F at certain wavelength may be expressed as:

$$F = I_{abs}\phi_f C \tag{1.15}$$

where I_{abs} is the intensity of the absorbed radiation and ϕ_f is the fluorescence quantum yield. Apparatus constant C comprised all factors for geometry, optical collection transmission, and detection efficiency.

Assuming Beer's law holds, the absorbed incident power I_{abs} is given by

$$I_{abs} = I_0 - I_0 e^{-\sigma_{abs} Nl} \tag{1.16}$$

where I_0 is incident light power, σ_{abs} is absorption cross-section, L is length of laser beam overlapping with sample gas, and N is sample vapor density (total).

Applying a Taylor series expansion,

$$e^{-\sigma Nl} = 1 + \frac{(-\sigma Nl)}{1} + \frac{(-\sigma Nl)^2}{2!} + \cdots \tag{1.17}$$

When the vapor concentration is very low, the assumption of $\sigma NL<<1$ may hold. Then the higher order terms in Eq.1.17 can be omitted. Therefore Eq.1.16 can be rewritten:

$$I_{abs} = I_0 \sigma NL \tag{1.18}$$

Combining Eq.1.15 and Eq.1.18, the fluorescence intensity F in the low sample concentration condition is

$$F = I_0 \sigma NL \phi_f C \tag{1.19}$$

Thus, fluorescence is linearly proportional to the concentration N of the analytes and excitation light power I_0.

1.3 Prior Work Done at the Laser Diagnostics Lab, NJIT

Barat and Poulos[13] have successfully used laser photofragment fluorescence spectroscopy to detect $Hg(CH_3)Cl$, $HgCl_2$ and HgI_2. In their experiments, a static cell (no flow) containing mercury compound vapor was probed with a deep ultraviolet laser to generate a characteristic spectra. The major results of their investigations are cited below.

1.3.1 Photofragment Fluorescence of Methylmercury Chloride.

Photofragment fluorescence (PFF) spectra of $Hg(CH_3)Cl$ were recorded for both focused and unfocused excimer laser excitation at 193 nm with a $Hg(CH_3)Cl$ concentration of 180 mg/m^3. Figure 1.2 shows a broad structured feature reaching a maximum near 550 nm in addition to the strong atomic Hg emission lines at 546 and 579 nm. This continuum was assigned to the B→X system of $HgCl^*$ excited states [14]. Excitation laser focusing increases the fraction of emission due to Hg atomic lines, versus emission from HgCl, by a

factor of 5. Atomic Hg emission lines are also observed at 254, 405, and 434 nm under unfocused and focused laser excitation. Figure 1.2b also shows a feature at 431nm assigned to CH*, a secondary product derived from the fragment CH_3. This emission is not present without focusing.

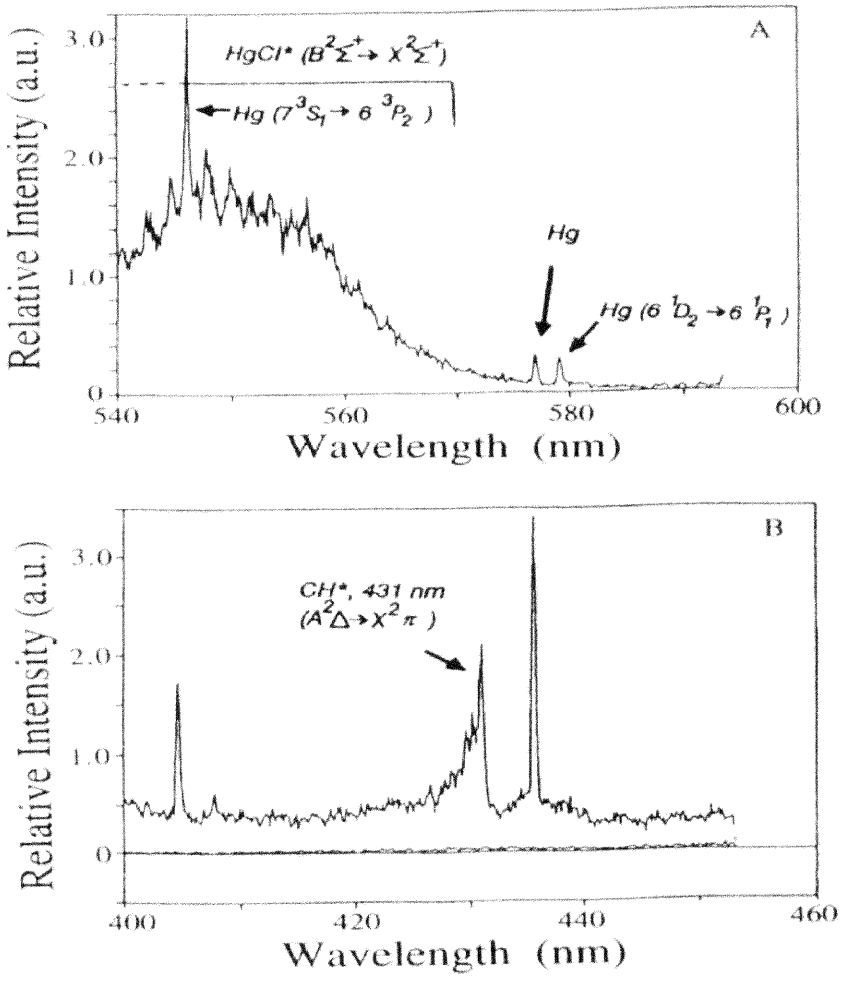

Figure 1.2 (a) PFF spectrum (540-600nm) from unfocused beam excitation (193nm) of $Hg(CH_3)Cl$. **(b)** PFF spectrum (400-450nm) for focused beam excitation (193nm) of $Hg(CH_3)Cl$ [13].

1.3.2 PFF of $HgCl_2$ Using 222nm Excitation

The $HgCl_2$ vapor was excited at 222 nm with laser energy of 2 mJ/pulse at a repetition rate of 10 Hz. The PFF signal was monitored at 253.7 nm. Signal linearity was observed from 1 to 250 mg/m^3. Similar results were observed for $Hg(CH_3)Cl$ excited at 222nm, with fluorescence measured at 546 nm. Signal linearity was observed from 0.09 to 400 mg/m^3.

1.3.3 PFF Signal Response to Quenching by Ambient Gas

The ratio of PFF intensity at "zero" quencher (ca. 1 milltorr background pressure) to PFF intensity at a given quencher pressure, I_0/I, was plotted vs. quencher (N_2) pressure. In the experiment, $Hg(CH_3)Cl$ was excited at 222 nm, with PFF monitored at 546 nm. A Stern-Volmer plot is shown in Figure 1.3. The quenching rate constant for Hg* with nitrogen is obtained from the regression of the data.

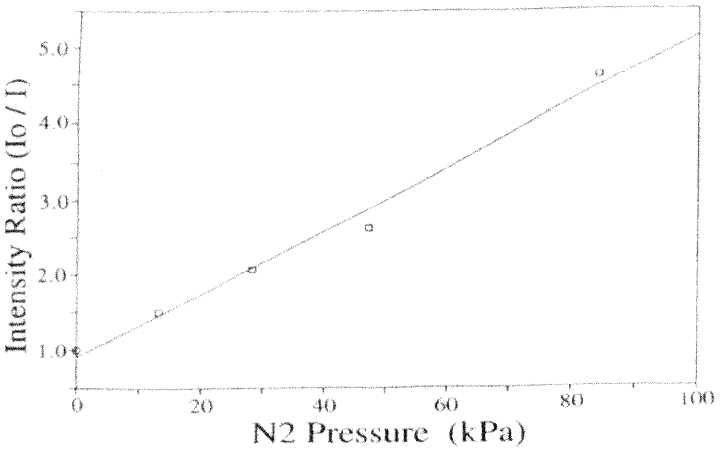

Figure 1.3. Stern-Volmer plot of PFF (detection at 546 nm, excitation at 222 nm) from $Hg(CH_3)Cl$ [13].

1.4 Scope of this Doctoral Research

The purpose of this doctoral research is to develop novel approaches for continuous emission monitoring of volatile mercury species found in stack or process off-gases. Such techniques should provide the high sensitivity, and specificity, while operating at relative low cost, needed for practical real-time analysis of both elemental and vapor compound mercury.

Figure 1.4 shows a vision of laser induced fluorescence as an on-line detection method to analyze continuously extracted samples. Both elemental mercury vapor and mercury compound vapor are tested in this work. For mercury compound, photofragment fluorescence spectroscopy is applied. Resonance fluorescence spectroscopy at 253.7 nm is used for detection of elemental mercury (Hg).

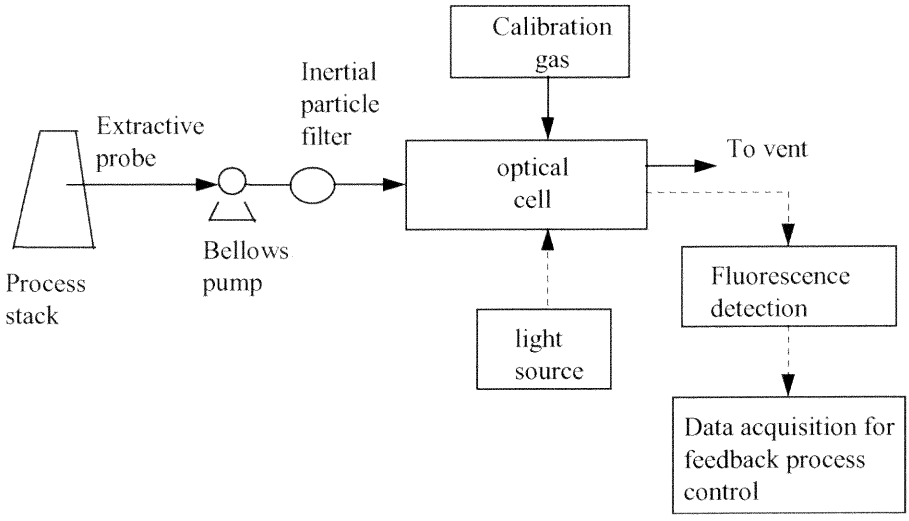

Figure 1.4. Continuous mercury species monitor system diagram.

Photofragment fluorescence of $HgBr_2$ in an atmospheric flow cell has been first investigated. Argon gas is used as the carrier and dilution gas. Laser excitation is chosen at 222 nm, while fluorescence is monitored at 253.7 nm. Important supporting data such as source and transfer line temperature control, time gating during signal detection, and signal/concentration linearity have been collected. In examining the PFF of mercury bromide ($HgBr_2$) vapor, the performance of two different detection schemes - charge coupled device (CCD) and photomultiplier tube (PMT) - are investigated in detail. Advantages/disadvantages, as well as limits of detection for both schemes has been obtained and compared.

As mentioned before, quenching limits the fluorescence detection sensitivity. In order to reduce quenching to improve detection sensitivity, a supersonic gas expansion combined with laser induced resonance fluorescence is used for detection of elemental mercury vapor in the second phase of this doctoral research. A supersonic beam is produced by flowing the sample gas from a higher pressure, and then expanding it through a small nozzle (200μm of diameter) into a vacuum. After expansion into vacuum, the gas density drops appreciably. Therefore, collisonal quenching is reduced which should improve the fluorescence efficiency. In this experiment, laser excitation and fluorescence monitoring are both at 253.7 nm. A time gating approach is used to separate fluorescence and laser beam- generated elastic background scattering.

In the work for atomic mercury measurement, the contribution of gas expansion to fluorescence intensity is investigated and discussed in detail. The time dependent fluorescence signal is obtained and analyzed with rate equations for a two electronic level system. The dependence of gas density upon axial distance of excitation to nozzle is

investigated experimentally and theoretically. The dependence of resonance fluorescence signal linearity on laser power and sample concentration, and the time resolution of the signal are all tested. A detection limit has been estimated as well.

In addition to the above work, the use of ultraviolet (UV) interferometery is investigated for extracting the narrow mercury emission line from the background. This UV interferometer as a spectral discriminator is examined as an alternative to time gating in separation of the resonance fluorescence from background scattering. The performance and limitations of this UV interferometer have been studied. Based on all these experimental results, conclusions and suggestions as to the best ways for detection of vapor mercury compounds and elemental mercury are drawn in the last chapter of the doctoral dissertation.

CHAPTER 2

DETECTION OF MERCURIC BROMIDE IN A FLOW CELL BY PHOTOFRAGMENT FLUORESCENCE

2.1 The Photofragment Fluorescence (PFF) Spectroscopy Technique

2.1.1 Principles of PFF Spectroscopy

For the case of a triatomic metal compound $HgBr_2$, Figure 2.1 illustrates PFF. If the excitation photon ($h\nu_{ex}$) has sufficient excess energy, the stable excited state HgBr* is populated. This hot fragment can then fluorescence at frequency ν_{f1}. The HgBr fragment can then absorb another excitation photon, resulting in the hot metal atom Hg*, which can then fluorescence at ν_{f2}. Target compound concentrations can be related to the fluorescence intensity from a hot fragment. Fragment identities and distributions as revealed in the fluorescence spectra, can in principle, provide information on the composition of the target, in a manner analogous to mass spectrometry and other fragmentation spectroscopies. For example, fluorescence photon $h\nu_{f2}$ is spectrally narrow, characteristic of atomic emission. The fluorescence photon $h\nu_{f1}$ would actually be present as a molecular band spectrum [13, 14].

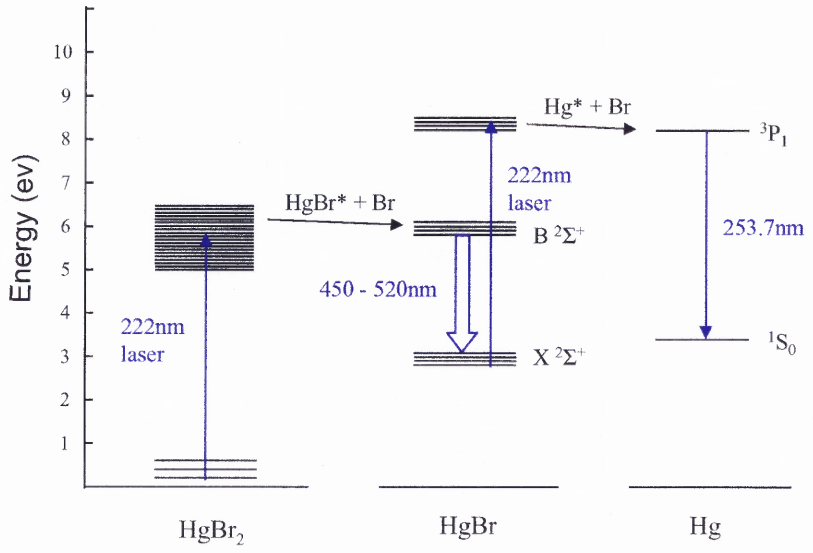

Figure 2.1 Energy diagram of photofragment fluorescence.

2.1.2 Applications of PFF Spectroscopy

PFF spectroscopy has been used for analysis of a variety of inherently non-fluorescent compounds. Compounds tested include Alkali Chlorides, NH_3, NaOH, NO_2, $GaCl_3$, Nitromethane [16-20], etc. PFF in the UV appears to be a particular promising analytical technique for mercury compounds. Mercury compounds are generally non-fluorescent. They absorb light strongly below 250 nm [22] as shown in Figure 2.2; and these absorption bands are dissociative. Furthermore, many mercury compounds (e.g. halides) are quite volatile, and consequently can be analyzed directly in the gas phase by a spectroscopic technique such as PFF. Use of photofragment fluorescence as an analytical tool for mercury compounds was demonstrated by Poulos [21]. Successful detection of $Hg(CH_3)Cl$ vapor down to sub-ppm levels was observed using an unfocused excimer laser

beam (193 nm) as the light source. The estimated limit detection, assuming reasonable improvements in light collection efficiency and detection gating, was under 0.1μg/m^3 (9 ppt) at a 2 minute averaging time.

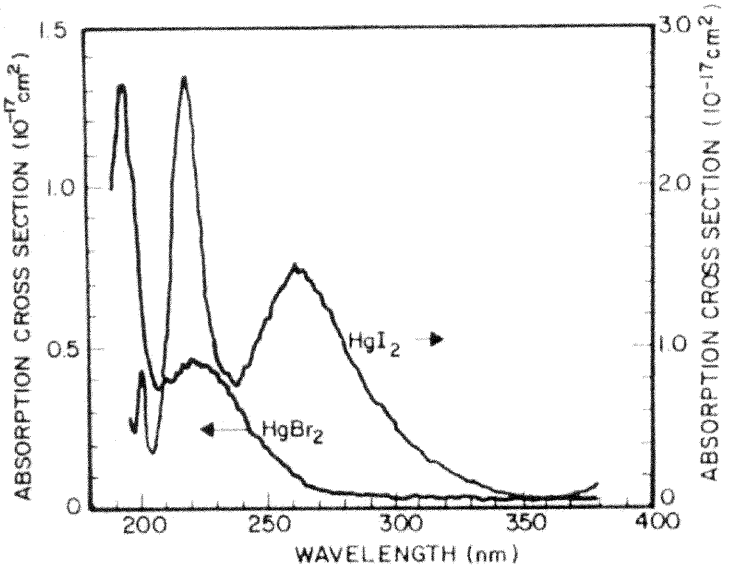

Figure 2.2 Absorption spectrum of mercury compounds [22]. Left y-axis corresponds to $HgBr_2$, and right y-axis corresponds to HgI_2.

In this doctoral research work, mercuric bromide ($HgBr_2$) vapor in a one atmosphere flow cell is detected by photofragment fluorescence spectroscopy. Mercuric bromide can be present in incinerator stack gases due to the nature of the original waste; for example, Hg-containing batteries and Br-based flame retardants. The long term goal of this work has been the development of a real-time mercury compound sensor.

2.2 Experimental Set-up

The apparatus consists of a pulsed dye laser system and optical guides, PFF spectroscopy flow cell, optical sampling system, detection system, and data acquisition system. Figure 2.3 illustrates an overview schematic of the apparatus. Each sub-system is described separately below.

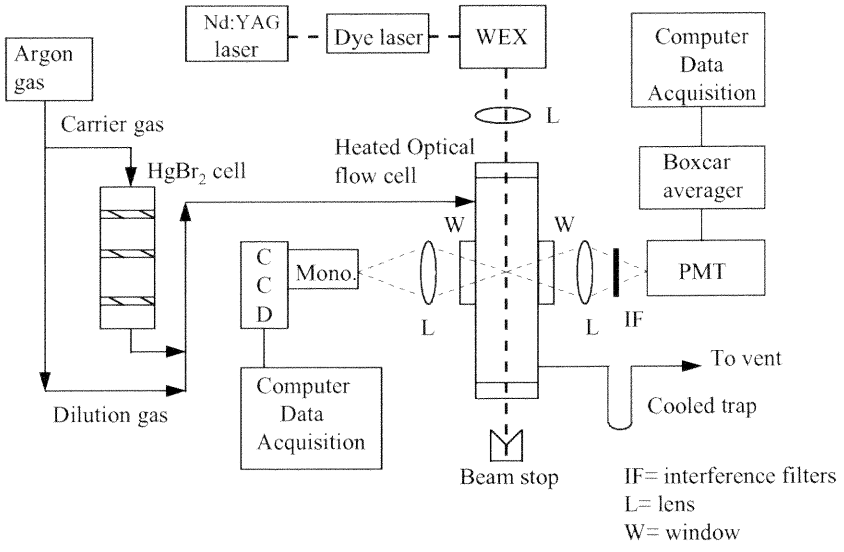

Figure 2.3 Research apparatus for PFF studies

2.2.1 Ultraviolet Laser System

The fundamental laser beam is from a Spectra-Physics Model GCR-3 pulsed Nd:YAG laser. It is Q-switched, outputs radiation at 1064nm with a maximum pulse energy of 850mJ and pulse width of 6 ns. In the experiment, the pulse rate of the Nd:YAG laser is always set at 10 pulse/sec (Hz). Passing through a second harmonic generation crystal, this fundamental laser beam is frequency doubled to 532nm radiation with a maximum

pulse energy of 400mJ. This radiation (532 nm) pumps a Spectra-Physics PDL-3 Dye laser.

The laser dye for the PFF spectroscopy investigation of $HgBr_2$ is Rhodamine 590. It is a very stable, high gain dye with peak output at 560nm and a tunable range from 553 to 577nm. The desired dye laser visible wavelength is converted into a UV line using nonlinear optics in the Spectra-Physics WEX-1 Wavelength Extender. For the PFF experiment, doubled Rhodamine 590 is mixed with residual fundamental YAG radiation (1064 nm) in the WEX to produce output in the range 219-227 nm with a peak output at 222nm. The excitation wavelength chosen for the PFF studies of $HgBr_2$ is 222nm, which falls in the mercury compound absorption region.

The UV laser power was monitored using a Scientech Model 372 power meter. Typical average laser power in this study at 222 nm is 30 mW, with pulse energy at 3 mJ (pulse rate 10 Hz). The laser beam passes through a focusing lens (2.5 cm diameter x 28 cm focal length) prior to entering the PFF cell. The laser beam is focused to an approximate spot size of 1 mm $\times$ 2 mm, which yields an average laser fluence of 150 mJ/ cm^2 per pulse.

2.2.2 PFF Spectroscopy Optical Flow Cell

Designed for flow conditions, the cross-shaped quartz photolysis cell contains four Suprasil windows and two ports at opposite ends for connection to the gas flow system. The laser beam is introduced through the windowed long axis (19 cm). Fluorescence is collected along the windowed short axis (5 cm), which is perpendicular to the long axis.

The entire flow cell is suspended within an insulated box, which is heated with an internal electrical strip heater. The heater is part of feedback temperature control loop which also includes a type K thermocouple located inside the box, and a proportional controller. The cell is maintained at 90 ^{o}C, which is 10 degree higher than the highest temperature of the vapor saturator. The cell is first evacuated, and then purged with argon gas while heating prior to introduction of $HgBr_2$ vapor.

2.2.3 Vapor System

Mercuric bromide vapor is generated in a heated, stainless steel tube containing $HgBr_2$ powder on three porous steel disks. A metered, downward flow of argon carrier gas entrains the vapor. The tube is suspended inside a heated cylinder. The temperature inside the tube is measured with a thin type K thermocouple and is kept constant with a controller. The flow rate of argon gas through the source tube is regulated at less than 70 cm^3/s (standard conditions) to ensure the saturation of $HgBr_2$ vapor. A separate, metered argon flow bypasses the heated source, and serves as a diluent to generate lower $HgBr_2$ concentrations.

Mercuric bromide vapor concentrations in the source outlet are determined based on published vapor pressure/temperature data in the form of the Claussius-Clapyeron equation [26]:

$$\log_{10} P^V = a - b/T \qquad (2.1)$$

where P^V = vapor pressure (Torr); T = absolute temperature (K); and a, b = species-specific constants (for $HgBr_2$, a = 10.181 and b = 4168).

Final $HgBr_2$ concentrations at the optical cell are based on both gas flows and one atmosphere (absolute) total operating pressure. Low $HgBr_2$ concentrations are achieved by increasing the fraction of diluent and/or operating the source at lower temperatures. In the experiment, the temperature of the $HgBr_2$ source was regulated at a specific temperature in the range of 20 °C to 80 °C, corresponding to vapor pressures of 6.8×10^{-5} mmHg to 2.3×10^{-2} mmHg. Temperature control was maintained to within ±2 °C, with a typical source temperature of 32 °C. This corresponds to a typical precision of ± 80 ppb in the corresponding a vapor concentration of 430 ppb. In order to prevent any condensation and subsequent loss of HgBr2 concentration, all transfer lines downstream of the source, like the optical cell, are kept at an elevated temperature (typically 90 °C) which is always higher than the source temperature.

2.2.4 Detection System

For this PFF study, photofragment fluorescence of $HgBr_2$ is monitored at 253.7 nm, which is the strongest emission line ($^3P_1 \rightarrow {}^1S_0$) of atomic mercury. The fluorescence light is collected by two optical systems: I) monochromator + charge coupled device (CCD), and II) interference filters + photomultiplier tube (PMT). In mode I, the fluorescence light emitted from the optical cell is collected and focused by a fused silica lens (50 mm diameter × 80 mm focal length) into a Scientific Measurement System MonoSpec 18 (0.156 meter, 1200 lines per mm grating, f# = 3.8) monochromator. In place of an exit slit, the monochromator is fitted with a Santa Barbara Instruments Group model ST-6 ultraviolet sensitive CCD camera. When the exit slit of the monochromator is removed in this way, the monochromator becomes, in effect, a spectrograph. The CCD camera is

thermoelectrically cooled to -20°C. The CCD dimensions are 750× 242 pixels, each of area 11.5 μ m × 27 μ m and dynamic range of 65535 counts. The camera is interfaced to a laboratory computer equipped with Kestrelspec software for CCD control, data collection and spectrum display. For convenience of alignment, the CCD and monochromator are mounted on an x-y-z translation stage. By optimizing the spectrum of background scattering (setting monochromator wavelength at 222nm), the fluorescence collection optics are aligned.

In mode II, the fluorescence is collected and focused by a duplicate lens through two stacked 253.7 nm interference filters (each ± 5 nm bandwidth). The transmitted light is detected by an end-on Thorn-EMI model 9558QB PMT. The output of the PMT is input to an SR250 gated integrator module of a Stanford Research Systems model 280 boxcar averager. The boxcar is interfaced to a separate laboratory computer for instrument control, data collection and display.

In detection mode II, even though the laser excitation is at 222nm, the PMT still detects a strong, short-lived (about 10ns) background signal which is superimposed on the weak long-lived fluorescence at 253.7 nm (about 120ns). Elastic scattering (at 222 nm) from the wall and windows of the optical flow cell transmitting through the outermost edge of the interference filters may contribute to this observed background signal. On the other hand, inelastic scattering and fluorescence generated by the coating/glass of the interference filters might contribute to the background as well. Due to the strong background, the PMT is easily saturated if only one filter is used. Thus, two interference filters are applied in mode II to reduce the background.

As photofragment fluorescence of $HgBr_2$ and the background are detected together by the PMT, a time-gating approach is used to separate the photofragment fluorescence from the background, which is illustrated in Figure 2.4, where, ΔT_c is boxcar gate delay, T_c is boxcar gate width and τ is fluorescence lifetime. In the case of laser excited photofragment fluorescence, background generally lasts as long as the laser pulse (10ns). Atomic fluorescence of Hg ($^3P_1 \rightarrow {}^1S_0$) can last about 120 ns. By properly setting the time delay and width of an electronic sampling gate in the boxcar, only the photofragment fluorescence is collected and integrated. The stray light signal component is largely rejected.

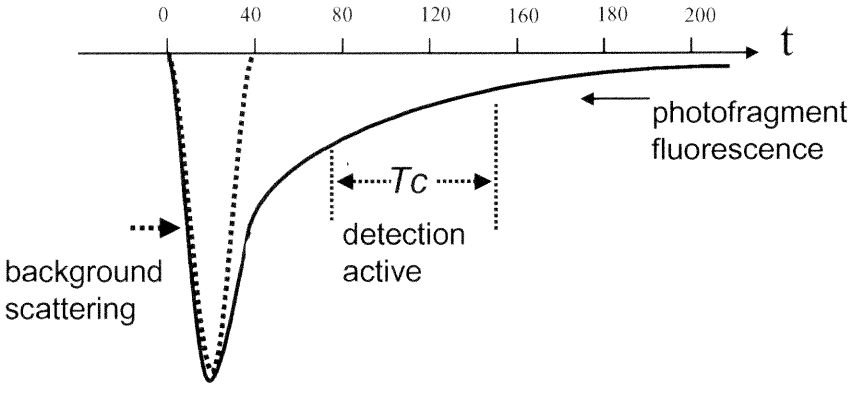

Figure 2.4 Typical display of fluorescence signal on the screen of oscilloscope. ΔT_c is boxcar gate delay, T_c is boxcar gate width and τ is fluorescence lifetime.

2.2.5 $HgBr_2$ Concentration Calibration

Flame atomic absorption spectrometry (FAAS) is used as an independent means to verify the $HgBr_2$ concentration flowing in Ar to the cell. A simplified drawing of a basic FAAS is given in Figure 2.5. Here, the sample solution is nebulized into the flame, the solvent evaporates and the metals in solution convert into their atoms. The radiation from the

source goes through the flame and is partially absorbed [23]. The emission linewidth of the hollow-cathode lamp is narrower than the atomic absorption linewidth; hence, linear Beer's law can be used.

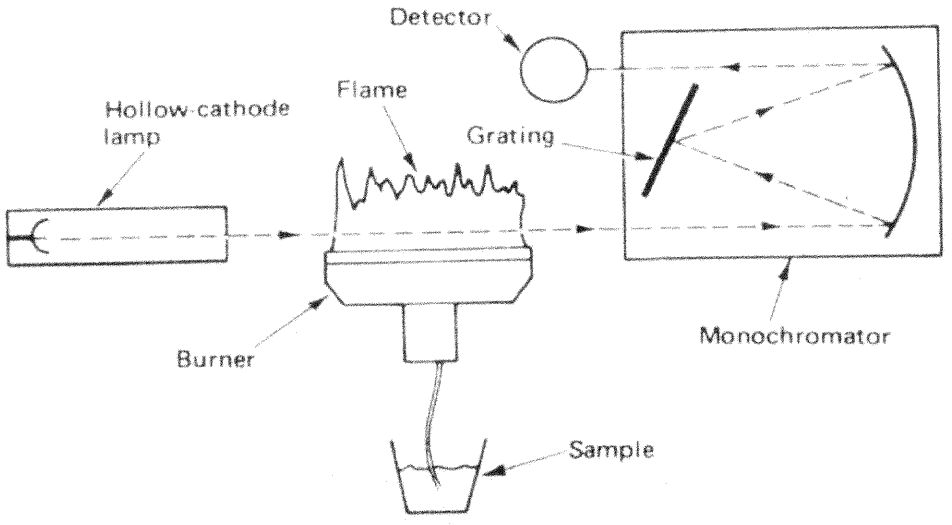

Figure 2.5 Simplified drawing of a basic flame atomic absorption system [23].

In the $HgBr_2$ concentration calibration experiment, $HgBr_2$ vapor with concentration of 5.4 ppm (based on vapor pressure-temperature relations) leaves the optical flow cell in a flow rate of 50 cm^3/s and then passes through a cold trap (0 °C). After collecting condensed $HgBr_2$ vapor in the trap over three hours, the trap is washed out with aqueous hydrochloric acid (HCl) solution quantitatively. The condensed $HgBr_2$ dissolves completely through multiple washes. In aqueous HCl, the $HgBr_2$ dissolves completely into Hg^{+2} and Br^- ions. Then, the solution containing Hg^{+2} is ready to be analyzed by FAAS.

A Perkin-Elmer model 403 Flame Atomic Absorption Spectrophotometer is used to analyze the sample solutions. Prior to any testing, the FAAS is calibrated to verify its linearity and sensitivity based on solutions with known concentrations. Figure 2.6 gives the linearity calibration of the on-site FAAS using a Hg Hollow-Cathode lamp.

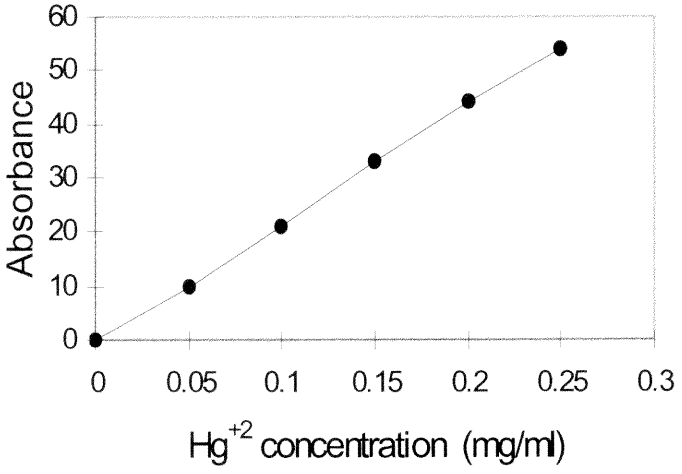

Figure 2.6 FAAS calibration showing linearity of absorbence with concentration of $HgBr_2$ sample.

The Hg^{+2} concentration in the experimental solution from the wash of the cold trap is expected to be 215 μg/ml. The measurement from FAAS gives the result of 200 μg/ml based on its absorbence. Therefore, the $HgBr_2$ vapor concentrations calculated from temperature data (Clausius- Clapyeron) in this work is correct to within a quite acceptable 8 % as compared to the independent FAAS analysis.

2.3 Photofragment Studies of $HgBr_2$ with PMT Detector (mode II)

2.3.1 Response of $HgBr_2$ Photofragment Emission to Laser Pulse Energy

The photofragment fluorescence emission of $HgBr_2$ can be described by the following photochemical mechanism.

$$HgBr_2 \xrightarrow{h\nu} HgBr + Br \quad (\lambda = 222\ nm) \tag{2.2}$$

$$HgBr \xrightarrow{h\nu} Hg^*(^3P_1) + Br \tag{2.3}$$

$$Hg^*(^3P_1) \rightarrow Hg(^1S_0) + h\nu' \quad (\lambda' = 253.7\ nm) \tag{2.4}$$

The bond dissociation energy of HgBr-Br is 72 ± 2 kal/mol [24] corresponding to light wavelength of 398 nm. Therefore, absorption of a single photon at 222 nm which corresponding to energy of 130 kcal/mol, is sufficiently energetic to dissociate $HgBr_2$ to HgBr and Br. The bond dissociation energy of Hg-Br is 17 kal/mol [24]. The threshold energy for the second step is:

$$112.7\ kcal/mol\ (\lambda = 253.7nm) + 17\ kcal/mol = 129.7\ kcal/mol \tag{2.5}$$

Thus, absorption of one or two additional photons by the HgBr has sufficient energy to dissociate it, and to deposit excess energy into the atomic Hg photo-product to yield the excited $Hg(^3P_1)$ state, which then emits at 253.7 nm.

Experimental PFF signal dependence upon laser fluence is shown in Figure 2.7, where the experimental parameters are: a $HgBr_2$ concentration of 124 ppb, a PMT voltage 1000v, a boxcar gate delay of 15 ns, gate width of 500ns, sensitivity of 20mv with 2-stage preamplifier. The curve can be separated into two parts by using data regression analysis. The quadratic portion for laser fluence less than 45 mJ/cm^2 per pulse suggests two-photon absorption with second-order regression coefficient R= 0.998. For laser fluence greater

than 45 mJ/cm^2 per pulse, the PFF signal is linear with first-order regression coefficient R= 0.999. A similar phenomenon was also observed by Schendel in his work of laser PFF spectrometric determination of Nitromethane [20].

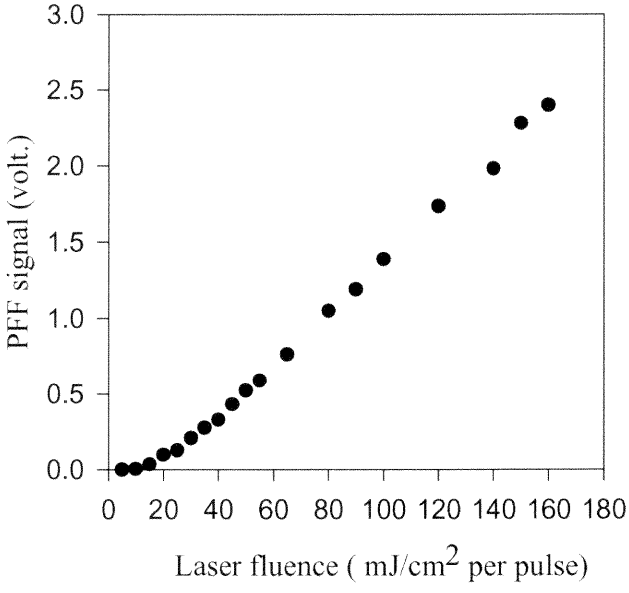

Figure 2.7 $HgBr_2$ PFF signal dependence upon laser fluence

The possible mechanism of photofragment fluorescence emission in this PFF study of $HgBr_2$ can be analyzed using population rate equation. Figure 2.8 shows the possible pathways of $HgBr_2$ photofragmentation. In the figure, I is the laser fluence, k_1 and k_2 are optical excitation rates, and k_3 is the decay rate of HgBr radical to the other possible pathways. D stands for all the pathways except the atomic fragment $Hg^*(^3P_1)$. The rate equation for $Hg^*(^3P_1)$ and HgBr radical can be written:

$$\frac{d[Hg^*]}{dt} = k_2 I[HgBr] \tag{2.6}$$

$$\frac{d[HgBr]}{dt} = k_1 I[HgBr_2] - k_3[HgBr] - k_2 I[HgBr] \tag{2.7}$$

where, $[HgBr_2]$, [HgBr] and [Hg*] stand for the densities of $HgBr_2$, HgBr radical and Hg*, respectively.

In steady state,

$$\frac{d[HgBr]}{dt} = 0 \tag{2.8}$$

Then, the density of HgBr radical in steady state is:

$$[HgBr] = \frac{k_1[HgBr_2]I}{k_3 + k_2 I} \tag{2.9}$$

By substituting Eq.2.9 into Eq.2.6, the density of [Hg*] is:

$$\frac{d[Hg^*]}{dt} = \frac{k_1 k_2 [HgBr_2] I^2}{k_3 + k_2 I} \tag{2.10}$$

Therefore, PFF of $HgBr_2$ is a two-photon process when laser fluence is low. At higher excitation fluence, PFF of $HgBr_2$ is linear.

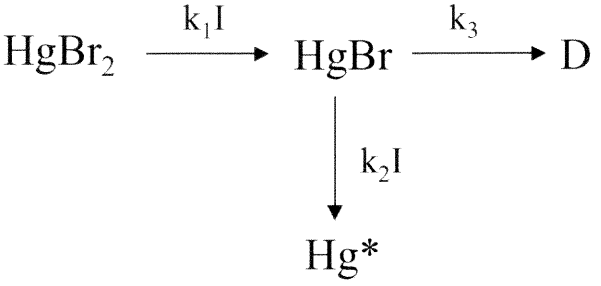

Figure2.8 Diagram of photofragmentation of $HgBr_2$ with rate constants.

2.3.2 Response Time

An important consideration for a future application of this method for real-time monitoring is the response time, which is defined as the time interval between the start of a step change in the concentration of the monitored gas stream and the time when the system output reaches 95 percent of its final value. The response time represents a time lag.

The response time was investigated by purging the fluorescence cell for a long enough time using bypass argon flow, then turning off this bypass flow. At t=0, the source flow is opened to 60 cm^3/sec to let only saturated $HgBr_2$ vapor go through fluorescence cell. Figure 2.9 shows the dependence of PFF signal on time during flow of 150 ppb $HgBr_2$ vapor to the initially clean fluorescence cell where laser energy was set at 1.3 mJ/pulse. It takes approximately 3 seconds for the signal to reach half value, and about 45 seconds for the signal to be maximum.

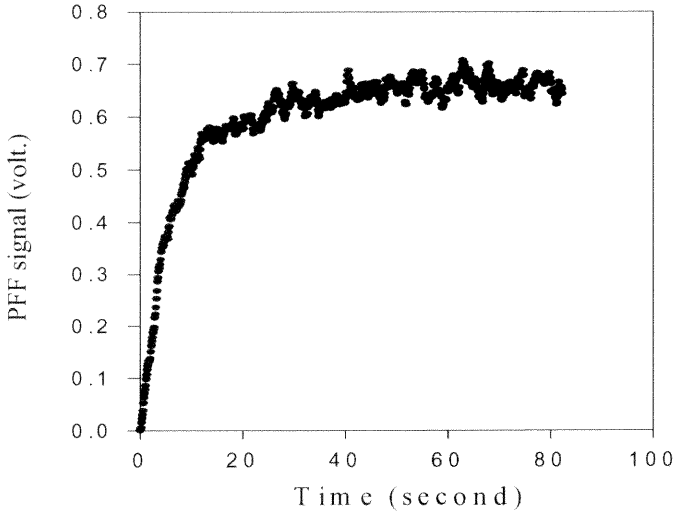

Figure 2.9 Time dependence of PFF signal during flow of 150ppb $HgBr_2$ vapor

The response time could be reduced by increasing the flow rate of carrier gas. The fluorescence cell is held at a higher temperature than the source to prevent surface condensation. However, cold points and persistent adsorption on surfaces apparently lead to the high response time. In the absence of such effects, the minimum response time could be as low as the gas residence time. For the optical flow cell, gas residence time τ_{gas} is:

$$\tau_{gas} = \frac{volume\ of\ cell}{actual\ flow\ rate\ at\ cell} = 1.5\ \text{sec} \qquad (2.11)$$

To reduce the response time, the temperature homogeneity of the flow cell could be improved. An alternative material, such as glass or Pyrex, for the transfer line could be evaluated.

2.3.3 Linear Dynamic Range

By heating the source to a high enough temperature (53 °C), and using the inert gas dilution method, the dynamic range of this detection method is investigated. Figure 2.10 shows the dependence of photofragment fluorescence upon $HgBr_2$ concentration up to 2 ppm (medium range). Experimental parameters are: average laser power 40mW, PMT 1000v, boxcar gate delay 15ns, gate width 500ns, signal sensitivity 0.1v, 2-stage preamplifier, 100 sample averaging. An approximately linear response with the PMT for $HgBr_2$ concentration is observed up to 0.7 ppm (11mg/ m^3). At higher concentrations, the PFF signal is sufficiently large to cause PMT saturation. This was experimentally verified with neutral density filters.

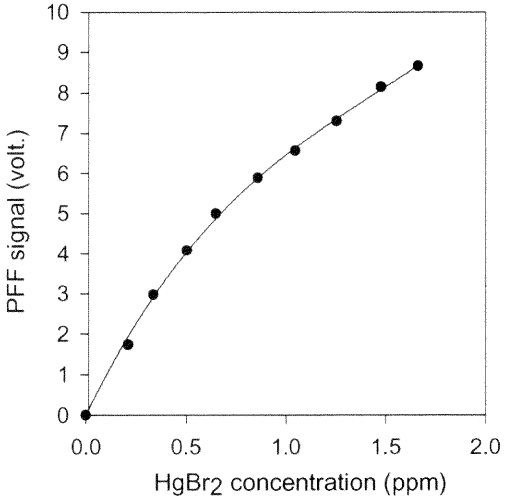

Figure 2.10 Photofragment fluorescence intensity vs. $HgBr_2$ concentration (in medium range).

2.3.4 Limit of Detection

To estimate the detection limit, inert gas dilution methods are used to simulate low-level concentrations. By keeping the total flow rate through the PFF cell constant, and changing the ratio of flow through the saturated vapor source to the bypass argon flow, the concentration of $HgBr_2$ can be made as low as 6 ppb (96 $\mu g/m^3$) at room temperature. Figure 2.11 gives the plot of sensitivity of $HgBr_2$ photofragment fluorescence signal using the PMT as the detector. Experimental parameters are: laser energy =3.5 mJ/ pulse , PMT 1000v, Boxcar gate delay of 15 ns, gate width of 500ns, and sensitivity of 20mv with 2-stage preamplifier. Averaging of 30 samples (pulses) at 10Hz corresponds to a duty cycle of 3 second. The noise is determined by the standard deviation of each measurement. By extrapolating the concentration back to a S/N = 2, the limit of detection is estimated to be 0.8ppb, corresponding to 13 $\mu g/m^3$. Further enhancement of the detection sensitivity might

be obtained by averaging the fluorescence signal over more laser pulses (i.e. increasing the duty cycle).

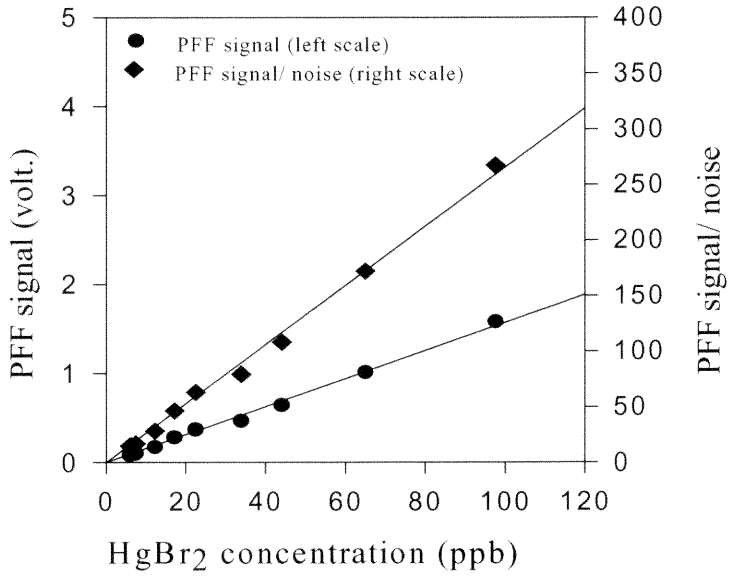

Figure 2.11 PFF signal sensitivity vs. $HgBr_2$ concentration (in low concentration range)

In a practical field environment such as municipal incinerator, extracted stack gas consists of combustion species such as CO_2, CO, H_2O, O_2 and N_2. Among them, O_2 has the largest quenching cross section for state $Hg^*(^3P_1)$ [27]. The PFF signal at 253.7 nm would be reduced by a factor of 0.05 at an O_2 concentration of 8 % [28]. In this case, the extrapolated detection limit would rise to approximately 16 ppb from 0.8 ppb. To improve the application of PFF for mercury compound detection in real industrial environments, a shorter wavelength excimer laser could be chosen. The absorption cross section of $HgBr_2$ at 193 nm is 3 times greater than that at 222 nm [22]. Also, the relatively high laser

energy, which can be 50 times greater than the present laser system, makes the excimer quite attractive for this application.

2.4 Photofragment Fluorescence Studies of $HgBr_2$ with CCD Detector (mode I)

2.4.1 Brief Introduction to Charge Coupled Device (CCD)

A Charge Coupled Device (CCD) is a two-dimensional (2-D) array detector. Its dimension are given in units of pixels. The basic function of the CCD detector is to convert an incoming photon of light into an electron which is stored in the detector until it is read out, thus producing data which the computer can display as a 2-D image (image mode). In some application, it does not have to be displayed as an image. It could just as well be displayed as a spreadsheet with groups of numbers in each cell presenting the number of electrons produced at each pixel [25]. Alternatively, for this $HgBr_2$ detection work, the CCD is used in a spectrum mode. In this case, the count in each pixel in a vertical column are summed (accumulated). The result is a histogram. The CCD has been used extensively in astronomical imaging, but has been used for spectroscopic applications only in the last several years [11]. Because of the many advantages of the CCD; i.e., sensitivity, dynamic range, low noise, speed, ruggedness; this device shows great potential in spectroscopic application.

For laser PFF work, the most common reported fluorescence detector has been the photomultiplier tube (PMT) due to its high quantum efficiency for most wavelengths, relatively low price, and ease of use. However, the fluorescence detection is most often limited to single transition wavelengths since the PMT is typically used with

monochromators (with exit slits) or interference filters. When PFF spectra with complicated structure are of interest, PMT use can be cumbersome.

A CCD detector has several advantages over a PMT in determination of trace gases by the PFF method. First, owing to its ability to detect several wavelengths simultaneously, it can be used for fast and convenient investigation of the fluorescence spectra from excited fragments so as to find the most sensitive excitation and detection wavelength combination. This is of great importance when the emission spectra of trace compounds are unknown. Second, the spectra information provided by the CCD allows parent molecule speciation by PFF. Generally , the spectrum of molecular fragments can indicate some structural information on the parent species.

2.4.2 Calibration of CCD Camera and its Monochromator

In detecting a fluorescence spectra with the CCD camera, the dispersion of the fluorescence spectra is along the horizontal axis of the CCD and the vertical dimension of CCD is used to accumulate the spectrum. In other words, the fluorescence intensity in units of counts at each x-axis pixel is the sum of the counts of all corresponding y-axis pixels; i.e., a histogram. The x-axis of the CCD histogram in this application corresponds to individual wavelength. The monochromator used with the CCD is fixed (no scan) while the CCD takes the fluorescence spectrum. The setting wavelength of monochromator is designed to roughly correspond to center of the x-axis of the CCD histogram. In order to find out the spectral coverage of the CCD, it needs to be calibrated by some light source with known spectrum. Since atomic emission of mercury is well-known, a mercury pencil lamp is used to calibrate the CCD camera.

Using the collection optics and geometry as shown in figure 2.3, the emission spectrum of the Hg pencil lamp as detected by the CCD camera is illustrated in Figure 2.12. The monochromator for this measurement is set at 385nm with a 25 μm entrance slit. The CCD is set at 0.1s exposure time. The two adjacent Hg emission peaks are assigned to 365.0nm and 404.6 nm, respectively [26]. Therefore, a spectral range of 43.8 nm is available with this given monochromator and CCD camera system. The FWHM (Full Width at Half Maximum) of the atomic Hg emissions observed by the CCD camera with a 25 μm entrance slit is about 1.7 nm.

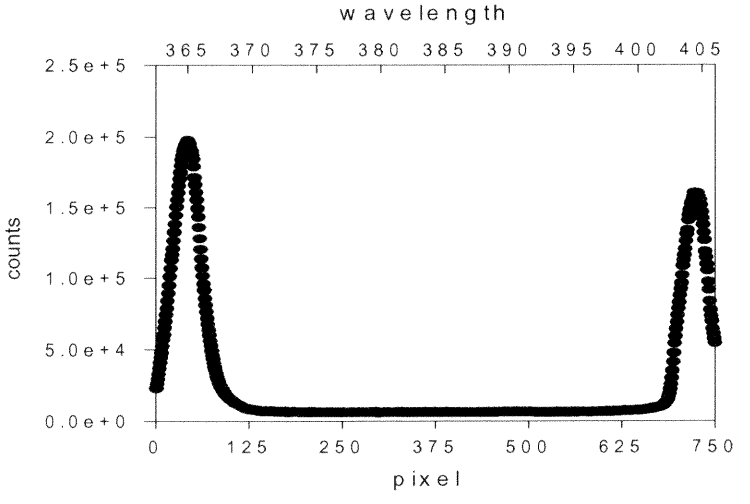

Figure 2.12 CCD calibration curve with Hg lamp when monochromator is set at 385nm.

2.4.3 PFF Studies of $HgBr_2$ with Detector of CCD

(a) Fluorescence Spectra

Figure 2.13 shows a calibrated PFF signal from 1.67 ppm $HgBr_2$ vapor at a laser pulse energy of 4 mJ. The CCD system was operated with 10 seconds exposure time, one accumulation per exposure, and a monochromator entrance slit of 250 μm.

From Figure 2.13, the estimated effective resolution of the PFF signal at 253.7 nm is 2.5 nm with the present ultraviolet sensitive ST-6 CCD camera and a 250 μm entrance slit.

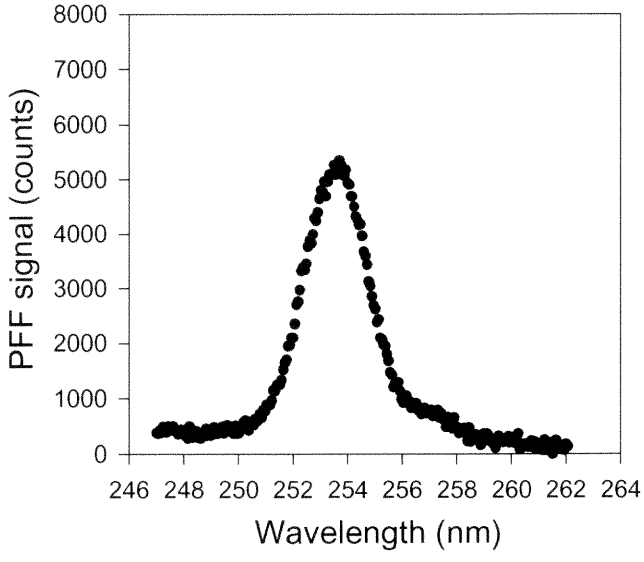

Figure 2.13 PFF signal of $HgBr_2$ with CCD detector.

(b) Dynamic Range

By varying the source temperature over the range of 43 °C to 88 °C, corresponding to a $HgBr_2$ concentration of 1 ppm to 53 ppm, the dynamic range of PFF detection with the CCD was investigated. Figure 2.14 shows the variation of PFF signal over a wide $HgBr_2$ concentration range, where the average laser power is 20 mW, the repetition rate is 10 Hz, and the CCD operates at 2 exposures of 10 second each. The signal recorded in Figure 2.14 is the peak value of each spectrum taken at different $HgBr_2$ source temperatures. The approximate linear range of CCD detection extends up to 20 ppm, corresponding to 320 mg/m^3. The saturation of the PFF signal at higher concentration in the experiment does

not result from the saturation of the CCD camera, since the read-out of all pixels were within their dynamic range (maximum count value is 65535).

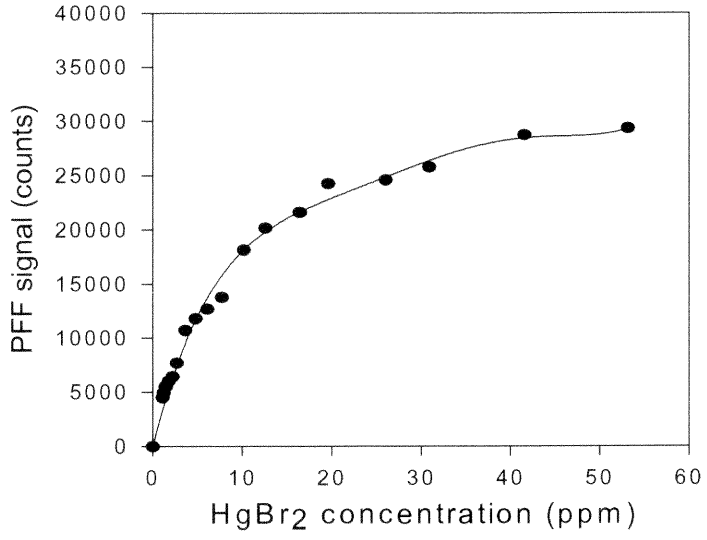

Figure 2.14 PFF signal dependence upon $HgBr_2$ concentration for CCD (in high concentration range)

Several possibilities — fluorescence quenching, fluorescence trapping, mercury self absorption, or beam absorption — might explain the departure from linearity of the PFF signal for $HgBr_2$ concentrations greater than 20 ppm in Figure 2.14. The beam absorption effect occurs when laser power at the detection area is decreased due to significant absorption of the 222 nm laser beam by high concentrations of $HgBr_2$ in the cell. Absorption of the 253.7 nm emission by the high level of $HgBr_2$, termed fluorescence trapping, might also cause the PFF signal to drop. In the experiment, a linear photodiode was placed at the exit window of the optical cell along the long axis to monitor the power of the exiting laser beam with and without $HgBr_2$ vapor present. No significant beam

absorption was observed. The theoretical concentration of $HgBr_2$ to cause significant beam absorption effect or fluorescence trapping can be calculated based on Beer Lambert's Law. Assume 20% attenuation of beam intensity, the concentration of $HgBr_2$ (N_1) required for beam absorption or the concentration of $HgBr_2$ (N_2) required for fluorescence trapping is given by:

$$\sigma_1 N_1 l_1 = \sigma_2 N_2 l_2 = \ln 0.8 \tag{2.12}$$

where : σ_1 is the absorption cross-section of $HgBr_2$ at 222 nm (0.47×10^{-17} cm^2) [22], σ_2 is the absorption cross-section of $HgBr_2$ at 253.7 nm (0.15×10^{-17} cm^2) [22], l_1 is the half length of the long axis of optical cell, and l_2 is the half length of the short axis of optical cell. Thus, N_1=200ppm and N_2=2312ppm. These are at least 10 times greater than the $HgBr_2$ concentration used in the experiment. Therefore, the beam absorption and fluorescence trapping can not effect the fluorescence intensity significantly under the experimental conditions.

Fluorescence quenching means $HgBr_2$ species collide with excited mercury atoms (Hg*), returning them to their ground states without emitting photons. The collisional cross-section σ_q^2 of $HgBr_2$ with Hg* ($^3P_1$) is estimated to be about 17 A^2 [27]. Using Eq. (1.13) and Eq. (1.14), the quenching rate constant k_q for $HgBr_2$ with Hg* is calculated to be 3.8×10^{-17} m^3/s. Applying the Stern-Volmer relationship [12], the fluorescence quantum yield ϕ_f in the presence of collisional quenching is:

$$\phi_f = \frac{1}{1 + k_q \tau_r [Q]} \tag{2.13}$$

where, τ_r is natural radiative lifetime at 253.7 nm [27] and [Q] is the number density of quencher. The calculated quantum yield of PFF from Hg* in the presence of 20 ppm

$HgBr_2$ is approximately 1, which means quenching of $Hg^*(^3P_1)$ by $HgBr_2$ does not effect the fluorescence intensity.

Finally, self-absorption of the 253.7 nm fluorescence by ground state mercury $Hg(^1S_0)$ might cause the nonlinearity of PFF signal. The significance of mercury self absorption is roughly calculated under two assumptions. First, since the photodissociation of $HgBr_2$ is a two-photon process, it is valid to assume that two absorbed photons produce one excited atomic photofragment $Hg^*(^3P_1)$. The second assumption is that all $Hg^*(^3P_1)$ atoms relax to ground state $Hg(^1S_0)$, thus ensuring the maximum amount of Hg ($^1S_0$) in the focal volume.

When laser power P is 20mW with a pulse rate of 10Hz, the number of available excitation photons I_0 per pulse is :

$$I_0 = \frac{P}{10h\nu} = 2.2\times10^{15}\ photons \quad (at\ 222nm) \tag{2.14}$$

The focal volume is 2 cm long as determined by the 2 cm monochromator slit length (assuming 1-to-1 magnification). The number of photons observed by $HgBr_2$ which contributes to the fluorescence is ΔI given by:

$$\Delta I = I_0(e^{-\sigma_1 NL_1} - e^{-\sigma_1 NL_2}) = 10.71\times10^{12}\ photons \tag{2.15}$$

where σ_1 is the absorption cross-section of $HgBr_2$ at 222nm, N is $HgBr_2$ concentration (20ppm), and L_1=8.5cm, L_2=10.5 cm (monochromator slit length 2cm).

Therefore, the maximum number of Hg atoms produced in ground state is $(10.71\times10^{12})0.5 \approx 5\times10^{12}$ per pulse over the focal volume v (0.016 cm^3, focused laser beam diameter about 1 mm). The absorption cross-section of $Hg(^1S_0)$ at 253.7 nm is 3.3×10^{-18} m^2 [9].

Applying Beer Lambert's Law again (considering absorption of photons toward detector direction), the absorbence is:

$$\sigma Nl = 3.3\times10^{-14}\times\frac{5\times10^{12}}{0.016}\times0.05 = 0.5 \qquad (2.16)$$

Thus, the calculated mercury self absorption is able to cause detected fluorescence intensity to drop 40% when parent species $HgBr_2$ concentration is 20 ppm in the optical cell. Hence, compared to the 20% sub-linearity of fluorescence signal at $HgBr_2$ of 20 ppm in Figure 2.14, the Hg self absorption is the likely explanation for the observed non-linearity in the experiment.

(c) Detection Limit

In order to estimate the detection limit of the CCD system, low concentrations of $HgBr_2$ vapor were generated by using argon dilution while keeping the $HgBr_2$ source temperature constant. This approach reduced temperature induced fluctuations in the $HgBr_2$ concentration. The PFF signals and corresponding S/N values at 253.7 nm detected with the CCD are presented in Figure 2.15. Here, the results are based on experimental parameters of: source temperature 53 °C, average laser power 40 mW , repetition rate 10 Hz, 10 second CCD exposure, and one accumulation of exposure. The signal shown in Figure 2.15 is the average number of detector counts collected for five consecutive scans at each concentration. The noise is the standard deviation observed for those five signals.

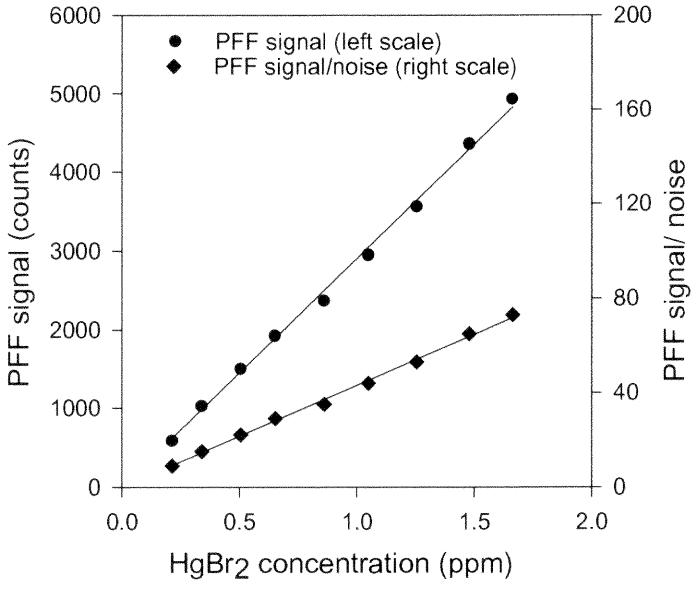

Figure 2.15 PFF signal sensitivity vs. $HgBr_2$ concentration for CCD (in medium concentration range)

By extrapolating the concentration back to S/N= 2, the estimated CCD detection limit is 30 ppb for the current setup. The observed magnitude of the noise is independent of the magnitude of the measured signal. Improvements in S/N for the source can, therefore, be achieved by maximizing optical throughput, such as increasing the collected PFF fluence into the entrance slit of the monochromator.

Some literature works in fluorescence detection by CCD have included a gated image intensifier [29,30]. Though an intensified CCD can detect smaller signals due to its enhanced gain, it can also amplify noise. Therefore, it may offer no significant advantage over the unintensified CCD camera in signal to noise ratio (S/N) performance, which is important to the present work. Time gating of the CCD also would not significantly enhance S/N in this application since there is no bright continuous background. The

detection at 253.7 nm is sufficiently removed from excitation at 222 nm by the attached monochromator. Moreover, the expensive image intensifier will tremendously increase the cost of a detection system for a practical airborne metals monitor. Thus, The CCD used in this study was not equipped with a gated image intensifier.

2.4.4 Comparison of the Detection Results from CCD and PMT

With the same laser settings, $HgBr_2$ source temperature, collection optics and dilution method as used for determination of the CCD detection limit, the sensitivity of the alternative PMT detection scheme (mode II) was investigated by setting the boxcar to average 100 laser pulses. This yielded an estimated detection limit of 1 ppb, but a linear response only up to 0.7 ppm (11 mg/ m^3) as shown in Figure 2.16. At higher concentrations, the PMT was observed to be saturated. In the set-up, the PMT saturates at lower concentrations than the CCD system. The saturation of the PMT could be avoided by lowering its voltage. However, PMT voltage was kept high to achieve a low detection limit in the experiment.

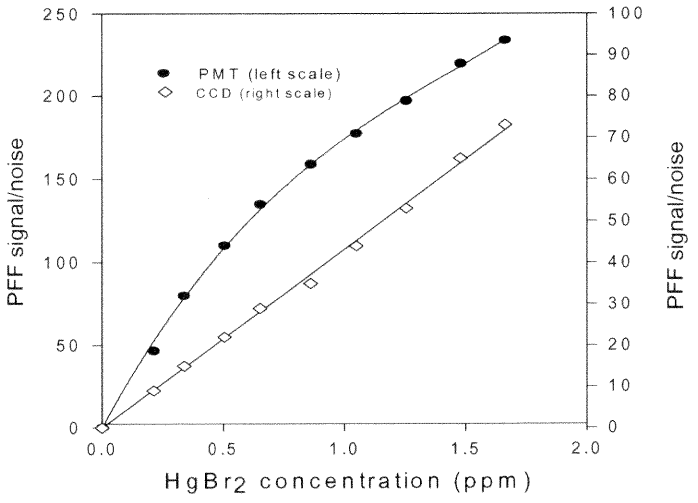

Figure 2.16 Comparison of S/N from CCD and PMT.

For a more fair comparison of observed detection limits of the CCD and PMT in the system, the S/N values for the PMT should be reduced to remove the boxcar averaging (100 laser pulses) effect, since the CCD system only averages over 5 consecutive scans. A modified PMT estimated detection limit is 5 ppb while the CCD detection limit is 30 ppb for S/N=2 at the same experimental conditions. Thus, mode II (interference filters + PMT) has a better detection limit than mode I (monochromator + CCD) in the PFF signal detection experiment. Now consider a more fundamental approach.

The actual optical throughput P for each detection system can be estimated as follows:

$$P = P_0 T \psi \eta \qquad (2.17)$$

where P_0 is incident fluorescent power on the slit plane (mode I, CCD) or filter plane (mode II, PMT). P_0 is same in both detection modes since they have identical collection

lens set-ups. ψ is quantum efficiency of either detector. η is a factor accounting for detector area. For the CCD+monochromator system, T represents the transmission of the Monospec 18 monochromator. It can be further expressed as [31]:

$$T_I = VFE_mR^2 \tag{2.18}$$

where, V: vignetting factor due to the slit aperture being smaller than the source image; F: $f^{\#}$ mismatch factor; E_m: grating efficiency; R: mirror reflection efficiency. For the PMT+ interference filters system,

$$T_{II} = \delta^2 \tag{2.19}$$

where δ is the transmission of the 253.7 nm interference filters.

Table 2.1 Parameters for calculation of throughput (mode I and mode II)

Mode I	Mode II
ψ: 0.22 η: 0.4315 V: 0.25 F: 0.7 E_m: 0.55 R: 0.8	ψ: 0.21 η: 1 δ: 0.17

The estimated actual throughputs for the CCD+monochromator system (mode I) and the PMT+interference filters system (mode II) are $0.0058P_0$ and $0.0061P_0$, respectively. This shows mode II has nearly the same optical throughput as mode I. On the other hand, the PMT system gives a six times better detection limit than the CCD system. Therefore, in the present experimental set-up, the PMT+ interference filters system has an inherently higher sensitivity.

During the PMT work, the optimized PMT voltage, the number of stages of signal preamplification, and gate setting of the boxcar averager can improve the S/N performance. Such optimizations are not available with the CCD system. The large area of the PMT photocathode makes for easier alignment and less loss of fluorescence light than the CCD system where fluorescence is focused onto the 250 μm slit. These factors could result in the lower sensitivity for the CCD system. However, the detection limit of CCD system could be improved with certain system optimizations. As in the CCD system, noise is independent of the fluorescence intensity, so higher sensitivities are possible with more optical throughputs. This can be accomplished by very careful system alignment, better f# matching of the collection lens to the monochromator, and better collection geometry, such as using a two-lens collection train.

CHAPTER 3

LASER-INDUCED FLUORESCENCE DETECTION OF MERCURY VAPOR IN A SUPERSONIC JET

3.1 Introduction of Cooling in Supersonic Jet

3.1.1 What is a Supersonic Jet ?

A supersonic jet is a gas beam at a velocity greater than that of sound. By flowing the gas from a high-pressure reservoir, and then expanding through a small nozzle into a vacuum, a supersonic beam can be produced over a short axial distance. With negligible viscous and heat conduction effects, this type of flow can be considered reversible, and therefore, isentropic. Various collimating apertures may be installed to shape the downstream flow pattern in some desired manner, and adequate pumping capacity is needed to maintain low downstream pressure. If the collimating apertures are absent, and if there is no attempt to control the downstream flow pattern, a supersonic source is called a free jet.

The state of gas at the reservoir is generally termed as the stagnation state where gas velocity can be assumed to be zero. From the First Law of Thermodynamics for an ideal gas, the energy equation can be written as: [32]

$$V^2 = 2\int_T^{T_0} C_p dT \tag{3.1}$$

where V is the velocity of the beam, T_o is the gas temperature in the reservoir, T is the temperature in the beam, C_p is the heat capacity at constant pressure. Based on the energy Eq.3.1, the gas temperature in the beam can be derived as: [32]

$$\frac{T_0}{T} = 1 + \frac{\gamma - 1}{2} M^2 \tag{3.2a}$$

$$\gamma = \frac{C_p}{C_v} \tag{3.2b}$$

where γ is the heat capacity ratio, M is the Mach number - defined as the ratio of the speed of the fluid (v) to the speed of sound (u) in the fluid under the conditions of flow.

$$M \equiv \frac{v}{u} \tag{3.3}$$

$$u = \sqrt{\frac{\gamma TR}{m}} \tag{3.4}$$

In the above equation, R is the gas constant and m is the molecular weight.

The flow is called subsonic, sonic, or supersonic, according to whether the Mach number is less than unity, at or near unity, or greater than unity, respectively.

Based on the ideal gas law,

$$\frac{P}{\rho T} = \frac{P_0}{\rho_0 T_0} = R \tag{3.5}$$

where T_0, P_0 and ρ_0 are temperature, pressure, and molar density in the reservoir, T, P, and ρ are the same quantities in the supersonic jet beam, and R is the gas constant as shown in Figure 3.1.

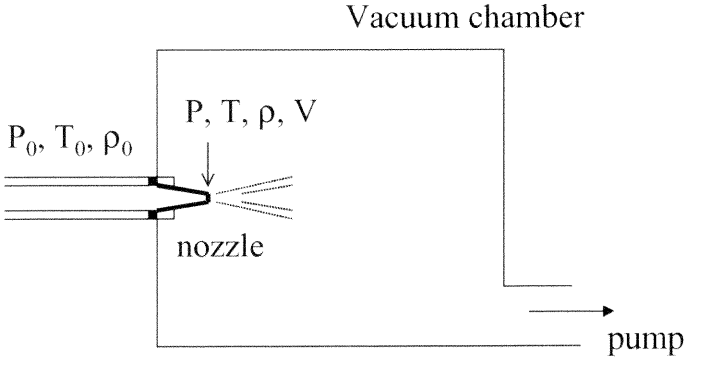

Figure 3.1 Diagram of gas expansion.

The relations between pressure, temperature, and density for an isentropic process are [32]:

$$\frac{P}{P_0} = (\frac{\rho}{\rho_0})^{\gamma} \tag{3.6a}$$

$$\frac{T}{T_0} = (\frac{P}{P_0})^{\frac{\gamma-1}{\gamma}} \tag{3.6b}$$

Substitution of Eqs. 3.6 into Eq. 3.2 yields the following important relations:

$$\frac{T_0}{T} = 1 + \frac{\gamma-1}{2} M^2 \tag{3.7a}$$

$$\frac{P_0}{P} = (1 + \frac{\gamma-1}{2} M^2)^{\frac{\gamma}{\gamma-1}} \tag{3.7b}$$

$$\frac{\rho_0}{\rho} = (1 + \frac{\gamma-1}{2} M^2)^{\frac{1}{\gamma-1}} \tag{3.7c}$$

Equation 3.7 indicates that in supersonic jet expansion where M>1, gas temperature, pressure and density in the supersonic beam will decrease. Cooling in the jet can be understood [33] as the expansion process converting the random kinetic energy of the gas to a directed mass motion that results in a narrowing of the molecular velocity distribution whose width determines the translational temperature. Rather than molecular gases, monatomic gases are preferable in obtaining the lowest temperatures because they do not store energy in rotational and vibrational degrees of freedom. Hence, for a given expansion ratio they will achieve a lower temperature.

Since the cooling process is much less efficient with polyatomic molecules, one typically "seeds" a small percentage of the polyatomic in a high pressure of monatomic carrier. At sufficiently low concentrations, the velocity of the larger molecule is

accelerated to that of the carrier and experiences a similar degree of cooling. This cold translational bath acts as a refrigerant for the other degrees of freedom. The internal degrees of freedom of the molecule begin to come to equilibrate with the translational degrees of freedom through collision in the early part of the expansion. Temperatures associated with the rotational and vibrational motions cooling using helium as carrier gas can be as low as 0.5K and 20-50K, respectively [44].

3.1.2 Jet Characteristics

Supersonic beam sources typically use a converging conical nozzle. For a nozzle with varying cross sectional area, the Mach number increases with a decrease in area when the flow is subsonic. However, when the flow is supersonic, the Mach number increases as the area increases. In other words, once the flow at the exit of the converging nozzle (the most constricted point) reaches sonic speed (M=1), the flow in the post nozzle region will be supersonic and M increases as the flow area increases [32]. Unity Mach number at the converging nozzle exit can be achieved by choking the flow [34]. Choking means that any change of vacuum ambient pressure P_b will not affect the flowing conditions within the nozzle [32].

Letting M=1 in Eq.3.7, the pressure at the nozzle exit P_E satisfies

$$G = \frac{P_0}{P_E} = \left(\frac{\gamma+1}{2}\right)^{\frac{\gamma}{\gamma-1}} \tag{3.8}$$

Choking the flow is provided by letting the pressure ratio P_0/P_b exceed the critical value $G \equiv (\frac{\gamma+1}{2})^{\frac{\gamma}{\gamma-1}}$. Then the exit pressure of nozzle becomes independent of P_b and equals to P_0/G [34].

The method of characteristics [35],which treats the expanding gas as a continuous medium, is generally used to determine the Mach number as a function of distance downstream of the nozzle (greater than a few nozzle diameters from the orifice). This result is

$$M = A(\frac{x}{D})^{\gamma-1} \tag{3.9}$$

where x is the distance from the nozzle, D is the nozzle diameter, and A is a constant which depends on γ, and is equal to 3.26 for a monatomic gas and 3.65 for a diatomic gas [36]. Thus, as one examines the conditions downstream of the nozzle, the Mach number increases and the temperature, pressure and density all decrease. However, there are a number of fundamental and practical limitations to the accuracy of Eq. 3.9 and which limit the amount of translational cooling obtained. The most important of these limitations are described below.

(a) Rarefication.

As the expansion proceeds, it eventually will reach the point where density is so low that there are no further inter-molecular collisions. From this point on, Mach number and temperature are " frozen" [45]. The "freezing" model predicts that the terminal Mach number M_T for argon gas (γ=1.67) is given by

$$M_T = 133(P_0 D)^{0.4} \tag{3.10}$$

where P_0 is the nozzle reservoir pressure in atmospheres and D is the nozzle diameter in centimeters. Combining Eq.3.10 and Eq.3.7 for argon, the terminal translational temperature T_T is given by

$$\frac{T_T}{T_0} = \frac{1}{1 + 5896(P_0 D)^{0.8}} \tag{3.11}$$

Equation 3.11 indicates that, for any given expansion gas, lower terminal temperatures may be obtained by increasing the pressure P_0 and/or the diameter of nozzle D. This trend will continue to be true until the available pumping speed (capacity) is exhausted.

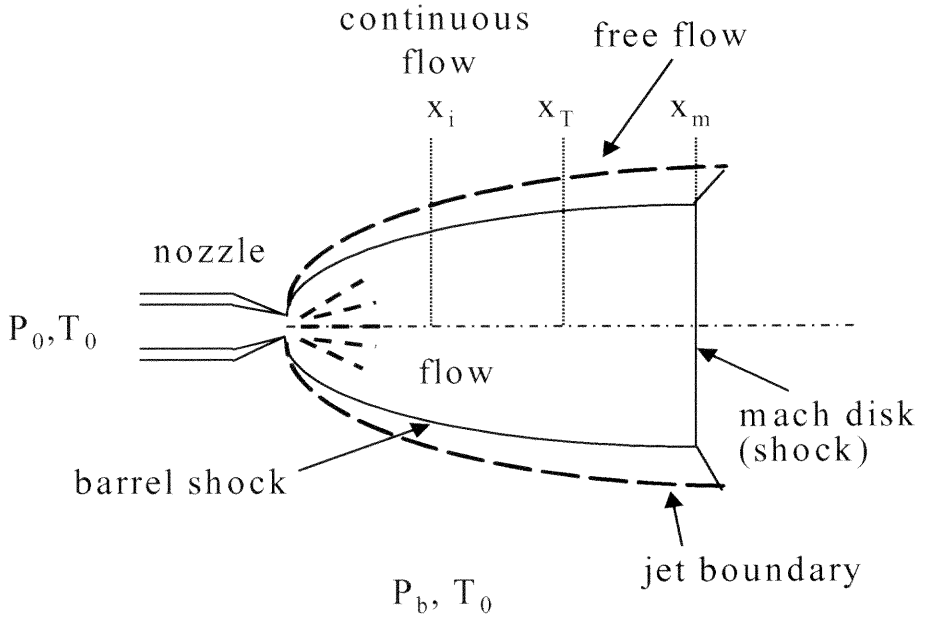

Figure 3.2. Supersonic jet formation by expansion of a gas at pressure P_0 and temperature T_0 into a vacuum chamber with pressure P_b ($P_b << P_0$).

(b) Pumping

Inadequate pumping speed in the flow pattern can create standing shock waves which decelerate jet molecules. A supersonic flow can not "sense" downstream boundary conditions. This is a crucial feature caused by that fact that information propagates at the speed of sound whereas the fluid moves faster (M>1)[34]. Thus, the flow does not "know" about the boundary conditions, yet it must adjust. The resulting dilemma is resulted by the occurrence of shock waves, very thin nonisentropic regions of large density, pressure, temperature, and velocity gradients. They are the outcomes of interaction of jets with background gases. Shock waves provide a mechanism to change the direction of a supersonic flow and to reduce the Mach number to subsonic values [34]. Once M<1, the flow can adjust to downstream boundary conditions. Referring to Figure 3.2, the gas first expands isentropically. However, since it does not "know" about P_b and M continues to increase, the gas over-expands and must be recompressed by a system of shocks, the barrel shock at the sides and the Mach disk shock normal to the centerline [34]. The Mach disk location X_m, where the jet terminates, is given by [35]:

$$\frac{X_m}{D} = 0.67\left(\frac{P_0}{P_b}\right)^{0.5} \tag{3.12}$$

This location is very close to that at which a shock is able to raise the local pressure to the background pressure P_b. If the vacuum chamber pressure P_b is too high, the Mach disk is so close to the nozzle that any useful spectroscopic studies will be prohibited.

(c) Condensation

Condensation of the expansion gas to form dimers, polymers, and eventually crystals or droplets can also limit the translational temperature by the release of the heat of condensation [47]. The frequency of three body collisions which are necessary to initiate condensation depends upon the mass and interatomic potentials of the atoms in question. However, since condensation is a much slower process than rotational or even vibrational relaxation for molecules, extensive internal cooling may be achieved before condensation takes place.

3.1.3 Advantages of Supersonic Jet Fluorescence Spectroscopy

As mentioned in chapter 1, fluorescence detection sensitivity is limited by the quenching effect. For many molecules excited at atmospheric pressure, the nonradiative process dominates, so that the fluorescence efficiency is low. However, with the test gas expanded in a supersonic jet, the quenching effect can be dramatically reduced. As previously discussed, gas density and temperature drop significantly in a supersonic jet downstream of the nozzle.

By substitution of Eq. 3.9 into Eq. 3.7, gas density and temperature drop at different position of supersonic jet (isentropic region) can be obtained. Figure 3.3a and 3.3b give the plot for carrier gases air and argon, respectively. Due to the decrease of gas density, the collision rate of excited atoms with quencher will be reduced. This method has the potential to enhance the use of resonance fluorescence for detection of atomic mercury.

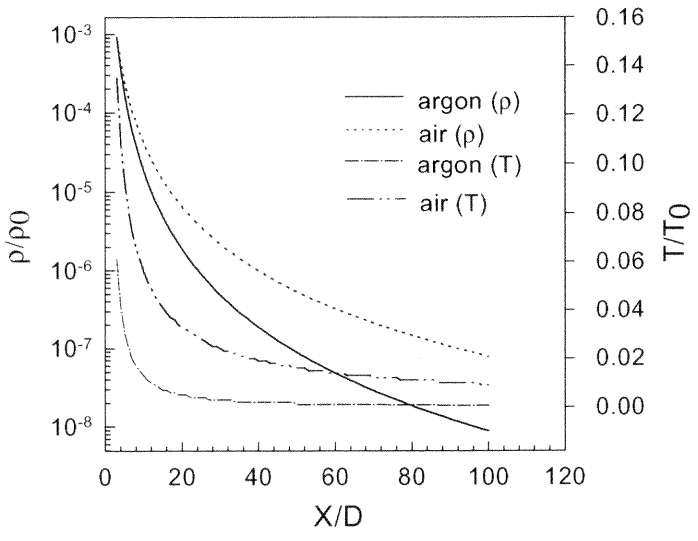

Figure 3.3a. Carrier gas (air and argon) density and temperature drop in a supersonic expansion (x is downstream distance and D is nozzle diameter).

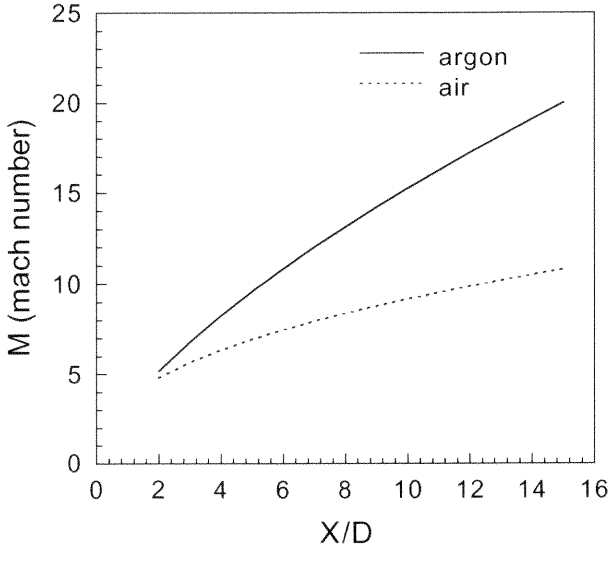

Figure 3.3b. Mach number for a supersonic expansion of argon/air gas as a function of downstream distance.

Based on Eq.1.15, the Hg resonance fluorescence intensity I can be modified to

$$I = I_0 \sigma N L \phi_f C \tag{3.13}$$

C can further be defined as:

$$C = \psi \frac{d\Omega}{4\pi} \eta \tag{3.14}$$

where ψ is the detector quantum efficiency, $d\Omega$ is the collection solid angle, and η is the dimensionless collection efficiency. After the gas expansion, the fluorescence quantum efficiency ϕ_f and atomic mercury concentration N in detection area will have opposite effects on the fluorescence intensity. Here, these effects are discussed in detail.

Applying the Stern-Volmer equation Eq.1.10, the quantum efficiency ϕ_f can be written as

$$\phi_f = \frac{1}{1 + \sum_i k_{qi} \tau_r [Q]_i} \tag{3.15}$$

$$k_{qi} = \sigma_{q_i}^2 \sqrt{\frac{8RT}{\pi \mu_i}} \tag{3.16}$$

$$\mu_i = \frac{M_{Hg} \cdot M_i}{M_{Hg} + M_i} \tag{3.17}$$

where, k_{qi} is the rate constant for species i quenching excited Hg atoms, μ is the reduced mass, σ_{qi}^2 is the effective collisional cross-section, R is the gas constant, τ_r is the natural radiative lifetime of the excited mercury atom $^3P_1 \rightarrow {}^1S_0$ (optical transition monitored in resonance fluorescence experiment), and $[Q]_i$ is the number density of quencher i.

Thus, using Eq.3.15, fluorescence quantum efficiencies as a function of density in the expanding jet can be calculated. Table 3.1 and Table 3.2 list the Hg fluorescence quantum

efficiencies with carrier gases of air and argon in vacuum/1atm condition (based on results as shown in Figure 3.3).

Table 3.1 Comparison of Hg fluorescence quantum yield in 1atm and vacuum conditions with air as carrier gas assuming Hg density in 1 atm condition is ρ_0.

For O_2, $\sigma_M^2 = 13.9A^2$ [27] $\tau_r = 1\times 10^{-7}$ sec. ($^3P_1 \rightarrow {}^1S_0$) [41]			
	ϕ_f	N	ϕ_f·N
1atm condition	0.003	ρ_0	$0.003\rho_0$
gas expansion (M= 4)	0.274	$0.028\rho_0$	$0.008\rho_0$

Table 3.2 Comparison of Hg fluorescence quantum yield in 1atm and vacuum conditions with argon as carrier gas assuming Hg density in 1 atm condition is ρ_0.

For Ar, $\sigma_M^2 = 0.7A^2$ [43] $\tau_r = 1\times 10^{-7}$ sec. ($^3P_1 \rightarrow {}^1S_0$) [41]			
	ϕ_f	N	ϕ_f·N
1atm condition	0.05	ρ_0	$0.05\rho_0$
gas expansion (M= 2)	0.355	$0.28\rho_0$	$0.1\rho_0$

Table 3.1 and 3.2 indicate that due to the jet expansion, the reduced collisional quenching (i.e. greater fluorescence quantum yield) will more than compensate for the drop in gas density, and should improve the detection sensitivity. The following gives the analysis of the contribution of jet cooling to the increase of fluorescence intensity. For Hg fluorescence in a supersonic jet, when the carrier gas density is sufficiently high that

$$k_q \tau_r [Q] >> 1 \tag{3.18}$$

then ϕ_f can be simplified (Eqs. 3.15 and 3.16) as

$$\phi_f \approx \frac{1}{\sigma_q^2 \sqrt{\frac{8RT}{\pi\mu}} \cdot \tau_r \cdot [Q]} \tag{3.19}$$

Multiplying by sample concentration N,

$$\phi_f \cdot N = \frac{1}{\sigma_q^2 \sqrt{\frac{8RT}{\pi\mu}} \cdot \tau_r \cdot [Q]} \cdot N \tag{3.20}$$

Since $\frac{N}{[Q]}$ is the mole fraction of Hg and is constant in any point of supersonic jet, an important conclusion is drawn from Eq.3.20 that

$$\phi_f \cdot N \propto \frac{1}{\sqrt{T}} \tag{3.21}$$

This means more jet cooling yields a stronger fluorescence intensity.

The above discussion of the jet cooling effect on fluorescence intensity based on Eq.3.13 does not consider the linewidths of the light source and the Hg absorption. In a real experiment situation, the linewidth of the excitation light source may be broader than that of the mercury absorption, which is termed a non-linear Beer's absorption phenomena. A detailed discussion of this non-linear effect will be covered in section 3 of this chapter. Here, the improvement of fluorescence sensitivity while considering the finite linewidths of the light source and the mercury absorption is discussed first.

In this case, Eq.3.13 is rewritten to include frequency ν dependence. The fluorescence intensity I_f can be defined by

$$I_f = \int_{-\infty}^{\infty} I(\nu)\sigma(\nu)\phi_f NLC d\nu \tag{3.22}$$

where, the incident light intensity is I(ν) and the mercury absorption cross-section σ(ν). For the jet work, the excitation light source is a laser beam. Assume the frequency dependence of this laser light source is a Gaussian function. Thus,

$$I(\nu) = I_0 e^{-4(\nu-\nu_0)^2 \ln 2/\Delta\nu_1^2} \tag{3.23}$$

where I_0 is the amplitude of light source power at the center frequency ν_0 and $\Delta\nu_1$ is the linewidth of the excitation light source.

The lineshape of the atomic mercury absorption may be Lorentzian or Gaussian depending on whether pressure broadening or Doppler/temperature broadening respectively, dominates [38]. In the current jet cooling case, the gas density is very low. Therefore, it is valid to assume mercury absorption is in Gaussian shape which is a result of temperature broadening. The absorption cross-section σ(ν) is frequently written in form [38]:

$$\sigma(\nu) = \frac{h\nu}{c} BS(\nu) \tag{3.24}$$

where B is Einstein coefficient, c is the speed of light, and S(ν) is the atomic lineshape function. Assume S(ν) has a linewidth of $\Delta\nu_2$ with a Gaussian shape:

$$S(\nu) = S(\nu_0) e^{-4(\nu-\nu_0)^2 \ln 2/\Delta\nu_2^2} \tag{3.25}$$

$$S(\nu_0) = \frac{1}{\Delta\nu_2}\left(\frac{4\ln 2}{\pi}\right)^{\frac{1}{2}} \tag{3.26}$$

Then, Eq. 3.22 becomes

$$I_f = \frac{1}{\Delta\nu_2} \cdot I_0 \left(\frac{4\ln 2}{\pi}\right)^{\frac{1}{2}} \cdot B \cdot \frac{h}{c} \int_{-\infty}^{\infty} \nu \cdot C \cdot \phi_f \cdot N \cdot L \cdot e^{-4(\nu-\nu_0)^2 \ln 2/\Delta\nu_1^2} \cdot e^{-4(\nu-\nu_0)^2 \ln 2/\Delta\nu_2^2} d\nu \tag{3.27}$$

Since the quantities C, ϕ_f, N, L are independent of frequency, Eq. 3.27 can be written as

$$I_f = \frac{1}{\Delta\nu_2} \cdot g \cdot \phi_f \cdot N \cdot \int_{-\infty}^{\infty} \nu \cdot e^{-(\nu-\nu_0)^2[4\ln 2(\frac{1}{\Delta\nu_1^2}+\frac{1}{\Delta\nu_2^2})]} d\nu \tag{3.28}$$

$$g = I_0(\frac{4\ln 2}{\pi})^{\frac{1}{2}} \frac{Bh}{c} \cdot L \cdot C \tag{3.29}$$

Since $\Delta\nu_1 << \nu_0$ and $\Delta\nu_2 << \nu_0$, then ν in the integration may be substituted by ν_0. Eq. 3.28 is approximately equivalent to

$$I_f = \frac{1}{\Delta\nu_2} \cdot g \cdot \phi_f \cdot N \cdot \int_{-\infty}^{\infty} \nu_0 \cdot e^{-(\nu-\nu_0)^2[4\ln 2(\frac{1}{\Delta\nu_1^2}+\frac{1}{\Delta\nu_2^2})]} d\nu \tag{3.30}$$

Using the identity

$$\int_{-\infty}^{\infty} e^{-aX^2} dx = \sqrt{\frac{\pi}{a}} \tag{3.31}$$

The integral in Eq. 3.30 is $\sqrt{\frac{\pi}{4\ln 2}} \cdot \sqrt{\frac{\Delta\nu_2^2 \cdot \Delta\nu_1^2}{\Delta\nu_2^2 + \Delta\nu_1^2}}$. Finally the expression of fluorescence intensity when the light source linewidth is $\Delta\nu_1$ and the absorption linewidth is $\Delta\nu_2$:

$$I_f = \frac{\nu_0}{\Delta\nu_2} g \cdot \phi_f \cdot N \cdot \sqrt{\frac{\pi}{4\ln 2}} \cdot \sqrt{\frac{\Delta\nu_2^2 \cdot \Delta\nu_1^2}{\Delta\nu_2^2 + \Delta\nu_1^2}} \tag{3.32}$$

Eq. 3.32 can be further discussed as following. If $\Delta\nu_1 >> \Delta\nu_2$ (that is, the light source linewidth is much broader than the absorption), then it can be written:

$$I_f = \frac{\nu_0}{\Delta\nu_2} g \cdot \phi_f \cdot N \cdot \sqrt{\frac{\pi}{4\ln 2}} \cdot \sqrt{\frac{\Delta\nu_2^2 \cdot \Delta\nu_1^2}{\Delta\nu_1^2}} \tag{3.33}$$

$$I_f = \nu_0 \cdot g \cdot \phi_f \cdot N \cdot \sqrt{\frac{\pi}{4\ln 2}} \tag{3.34a}$$

Combined with Eq. 3.21,

$$I_f \propto \frac{1}{\sqrt{T}} \tag{3.34b}$$

Eq. 3.34 tells that when the laser (the current light source) linewidth is broader than mercury absorption linewidth, the fluorescence intensity is linear with inverse of square root of temperature in the jet. If $\Delta\nu_1 << \Delta\nu_2$ (that is, the absorption linewidth is broader than the light source) then Eq. 3.32 approximately is

$$I_f = \frac{1}{\Delta\nu_2} g \cdot \phi_f \cdot N \cdot \sqrt{\frac{\pi}{4\ln 2}} \cdot \Delta\nu_1 \tag{3.35}$$

The dependence of $\Delta\nu_2$ on temperature T (Doppler broadening) is of the form [38]

$$\Delta\nu_2 = \frac{2}{\lambda_0}\left(\frac{2RT}{m}\ln 2\right)^{\frac{1}{2}} \tag{3.36}$$

where, λ_0 is the center absorption wavelength, m is molecular weight of mercury and R is gas constant.

Substituting Eq. 3.36 into Eq. 3.35:

$$I_f \propto \frac{1}{\sqrt{T}} \cdot \phi_f \cdot N \tag{3.37}$$

and therefore, combining with Eq.3.20,

$$I_f \propto \frac{1}{T} \tag{3.38}$$

This expression gives another important conclusion. When the laser lineshape is narrower than mercury absorption, not only reduced quenching improves the fluorescence intensity, but also the increased absorption, due to the drop of temperature and correspondingly a more narrow absorption linewidth, also contributes. With these two factors, fluorescence intensity is increased as a function of inverse of gas temperature. In summary, for the case

of $k_q\tau_r[Q] >> 1$, decreased collisional quenching in the expanding jet, which results in an increased quantum yield for fluorescence and increased absorption by mercury atoms ($\Delta\nu_1 << \Delta\nu_2$), will overwhelm the reduction of sample concentration upon expansion, and eventually improve the fluorescence intensity.

When gas density drops low enough, the approximation $k_q\tau_r[Q] >> 1$ is not satisfied. Upon further decrease of gas density, the fluorescence quantum efficiency will approach 1 and collisional quenching becomes insignificant. Then the fluorescence intensity may decrease due to the continuing drop of sample density, or it will not change if the expansion reaches the "frozen point" at which point gas density becomes constant. However, the lower gas pressure associated with gas expansion will decrease the background scattering intensity such as Rayleigh, Roman and Mie scattering which are linearly with pressure. Experimentally reducing background is an another important factor to indirectly improve fluorescence detection. This is particularly helpful for detection of resonance fluorescence where excitation and detection are at the same wavelength. Fluorescence is generally much weaker than the background scattering. The photodetector senses the background and fluorescence at the same time. If the background is too strong, the photodetector will easily be saturated without sensing any weak fluorescence. Once the background is reduced to about the same level as the fluorescence, the output of the photodetector can include enough fluorescence information for investigation.

One more advantage of fluorescence detection combined with jet cooling is the increased fluorescence lifetime. The decreased collision quenching rate at low pressure can result in an extended lifetime of the atomic mercury excited state. This will allow fluorescence signal to be well distinguished from background scattering signal. For

photofragment fluorescence, the lower temperature associated with this gas expansion will further reduce the Doppler linewidth. This effect will sharpen the fluorescence spectra which leads to a better discrimination of fragment structure.

3.2 Calibration of Excitation Light Source for Detection of Resonance Fluorescence in Supersonic Jet

Resonance fluorescence at 253.65 nm ($^3P_1 \rightarrow {}^1S_0$) is used as the detection scheme for measurement of elemental mercury in a supersonic jet. The excitation source which generates 253.65 nm radiation uses the same laser system as described in Chapter 2 for the photofragment fluorescence (PFF) experiment. For the PFF experiment on mercuric compound, the absorption bandwidth is quite wide compared to the laser line. Therefore, precise calibration of the laser system may be skipped. However, due to the narrow line structure of atomic mercury ($^1S_0 \rightarrow {}^3P_1$), the laser excitation must perfectly match the transition of two atomic energy levels to induce fluorescence emission. Thus, prior to resonance fluorescence experiments in the supersonic jet, the laser itself must first be calibrated.

Our calibration starts with the tunable dye laser. A grating installed in its oscillator disperses the light, allowing only a narrow wavelength to be reflected back into the oscillator cavity, which provides the required feedback to achieve lasing. Different laser counter setting (corresponding to the grating output) will give a different dye laser wavelength output. For the Hg resonance fluorescence experiment, the laser dye used is DCM in methanol solvent with output in the range of 610nm to 660 nm and a peak at 630nm. In order to have better ultraviolet (UV) excitation efficiency, a second dye LDS

698 (mass ratio relative to DCM is 1:3.4) is mixed with DCM to red-shift the excitation curve. The mixing dye gives output in the range of 610 nm to 700 nm with a peak at 660 nm. After going through the WEX system (frequency doubled plus residual 1.06 μm), the laser beam has a tunable wavelength in the range of 237 nm to 263 nm. In order to get atomic resonance fluorescence, the dye laser counter must be set precisely to output radiation at 253.65 nm.

The experimental setup for the laser counter setting calibration is shown in Figure 3.4. This calibration is based on detection of atomic Hg resonance fluorescence in a static cell while changing the laser counter setting. The static, all-quartz photolysis cell contains a sample well and a single valve connection to the gas/vacuum manifold. The sample well contains liquid Hg. Prior to the experiment, the cell is evacuated to near-vacuum (ca.10 milltorr background pressure). The static cell is then filled with 1 atm Ar. The 253.65nm beam is then applied. The resonance fluorescence measurement under 1 atm Ar serves three purposes. First, the pressure inside static cell is balanced with atmospheric pressure reducing the potential for leaks. Thus O_2 in atmosphere will not enter the static cell to quench out the fluorescence signal. Second, the linewidth of the mercury absorption is increased with the introduction of 1 atm Ar (pressure broadening). This will increase the likelihood of overlapping the mercury absorption line profile with that of the laser source. Third, Ar gas serves as collision partner to assist the heavy Hg atoms which are at low concentration to uniformly distribute in the static cell.

The laser beam is introduced through the long windowed axis of the static cell. Resonance fluorescence is collected along the short axis, normal to the long axis of static cell. Fluorescence is focused into a calibrated McPherson Model 218 (0.3 meter, 1200

lines per mm grating, f#=5.3, dispersion = 2.6 nm/mm, resolution = 0.06 nm at 313.1 nm) monochromator.

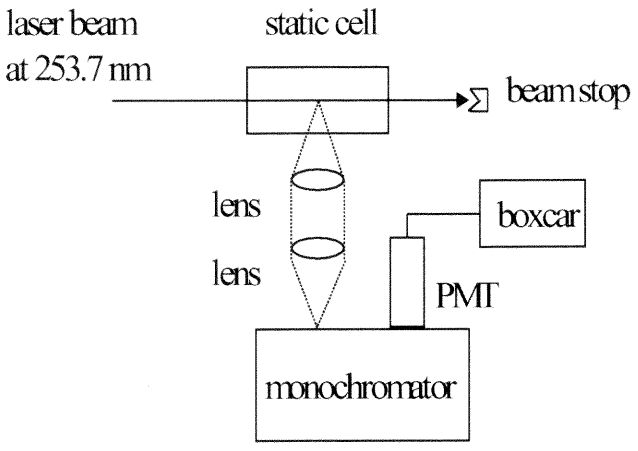

Figure 3.4 Experimental set-up of laser calibration for detection of Hg resonance fluorescence.

By manually changing the laser counter while fixing the McPherson monochromator at 253.7 nm, the variation of the intensity of the resonance fluorescence is observed. Figure 3.5 shows the dependence of resonance fluorescence on laser counter setting. It is straight forward that laser counter setting which yield the peak of the resonance fluorescence spectrum gives the radiation with wavelength of 253.65 nm. Therefore, in the following experiments for Hg resonance fluorescence detection in a supersonic jet, Dye laser counter is always set at 26650.5 to ensure output wavelength at 253.7 nm.

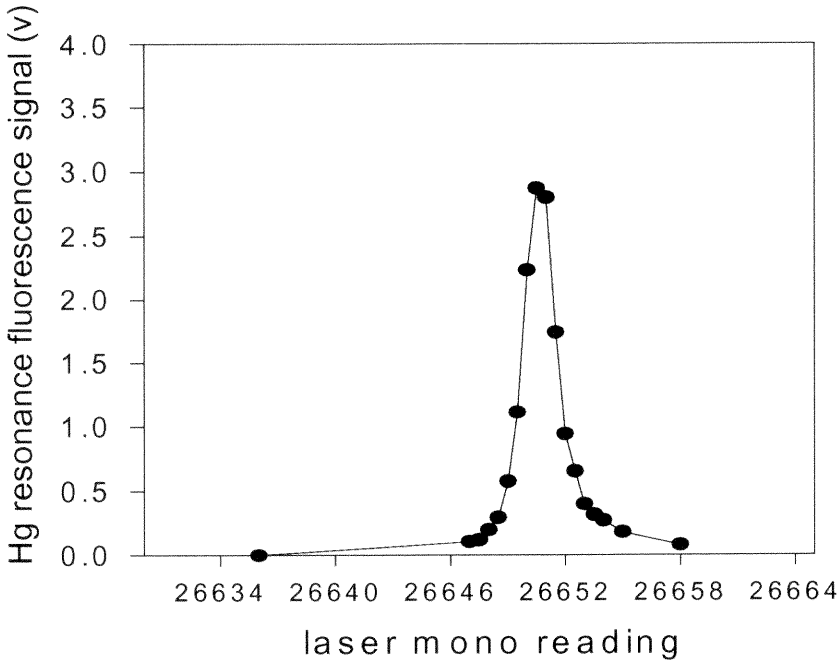

Figure 3.5 Hg resonance fluorescence signal vs. laser counter setting. Grating in Dye laser operates in 4^{th} order.

In addition to the Dye laser counter calibration, the linewidth of this laser radiation at 253.65 nm is investigated as well. This linewidth investigation gives the important background information for the future Hg concentration calibration experiment and Hg resonance fluorescence experiments for the supersonic jet. Figure 3.6 illustrates the set-up for this laser linewidth investigation. It is based on evaluating scattered laser light. For this investigation, laser is set at a fixed wavelength of 253.65 nm while scanning the McPherson monochromator.

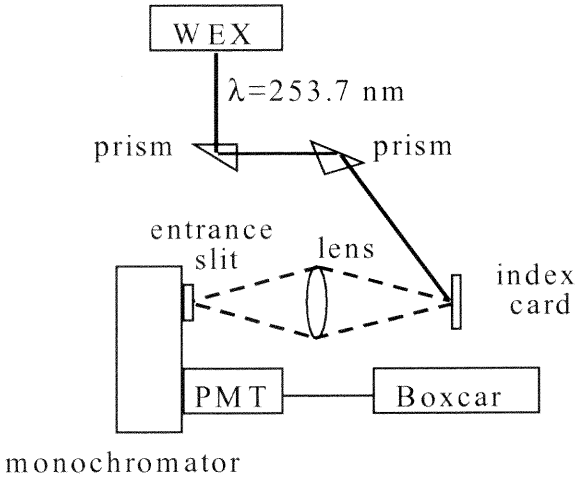

Figure 3.6 Schematic of apparatus used for study of laser linewidth.

The variation of scattered laser light intensity upon the monochromator setting is shown in Figure 3.7. With entrance slit width and exit slit width both at 50 μm, detected laser linewidth is about 0.166 nm. By narrowing slit width down to 10 μm, a measured laser linewidth about 0.07 nm at 253.7 nm is obtained. When slit width is set at 50 μm, the resolution of this monochromator is determined by its linear dispersion which is

$$2.6 \text{ nm/mm} \times 50 \text{ μm} = 0.13\text{nm} \tag{3.39}$$

When the exit slit width is narrow enough, the measurement resolution is determined by monochromator itself. For this McPherson monochromator, its resolution is 0.06 nm [50], very close to the result when the slit width is 10 μm. However, based on the manufacturer specification of this laser system, the laser linewidth is about 1 cm^{-1} at 253.65 nm corresponding to 0.007 nm. This is 10 times more narrow than what has been observed. Therefore, the measurement of laser linewidth here is believed to be limited by the resolution of monochromator itself, and that the detected laser line shape is convoluted with a Gaussian instrumental function.

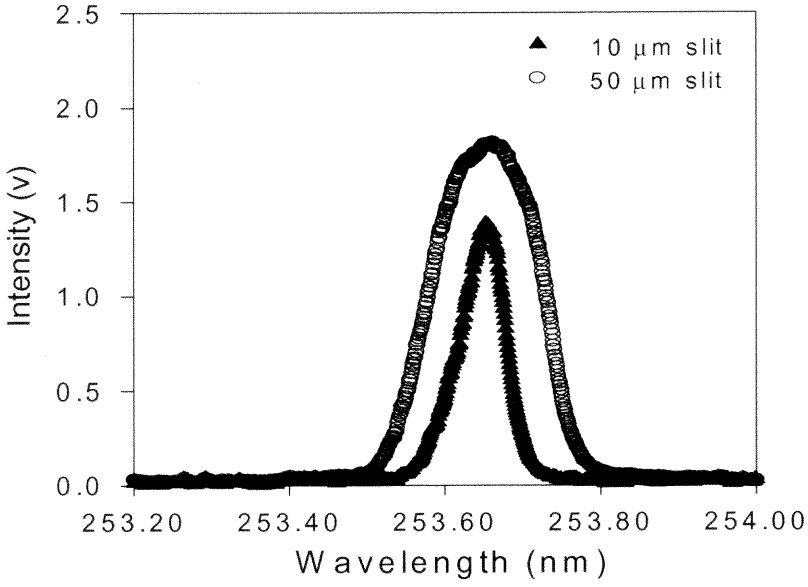

Figure 3.7 Monochromator scan of scattering light generated by laser radiation at 253.7 nm.

3.3 Calibration of Sample Concentration from the Mercury Vapor Saturator

3.3.1 Purpose of Calibration

In the work of resonance fluorescence detection under jet expansion, Hg sample vapor is provided by purging argon carrier gas through a special glass vessel containing liquid mercury. Later, this vessel is referred as the mercury saturator. The structure of mercury saturator is shown in Figure 3.8. Liquid Hg can be filled to all three stages. Ar gas from the tank enters the bottom of the saturator, and then flow through three stages of frits while mixing with Hg vapor from the liquid. The Hg/Ar saturator is immersed in a constant temperature bath equipped with water circulator and heating coil. Due to its large heat capacity, the bath maintains the setting temperature for quite a long time with

stability of ±2 °C. It is assumed that the bath temperature is also the liquid mercury and Hg vapor/Ar gas temperature.

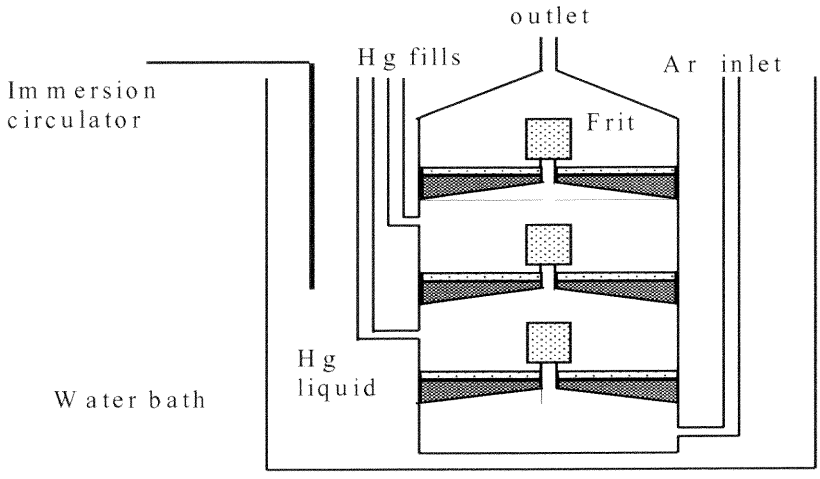

Figure 3.8 Plane view (not to scale) of mercury vapor saturator.

The concentration of Hg vapor theoretically is determined by the temperature of the mercury fluid (i.e. Hg vapor pressure), assuming Hg vapor and Ar carrier gas are well equilibrated while mixing. However, this is not guaranteed for every flow rate setting. In fact, only certain range of flow rate of Ar gas is observed good for phase equilibrium. In order to make sure that the Ar gas is well saturated with Hg vapor, a sample concentration calibration has to be done first. The purpose of concentration calibration is to investigate whether the actual concentration of Hg vapor in the Ar obtained from the saturator corresponds to the vapor pressure of Hg at the saturator temperature.

3.3.2 Experiments on Hg Concentration Calibration

The sample concentration calibration is based on optical absorption spectroscopy. In absorption spectroscopy, the amount of light being absorbed is directly related to concentration of absorption medium based on the Beer-Lambert Law. Figure 3.9 shows the schematic of the absorption experiment for Hg vapor from Hg/Ar saturator.

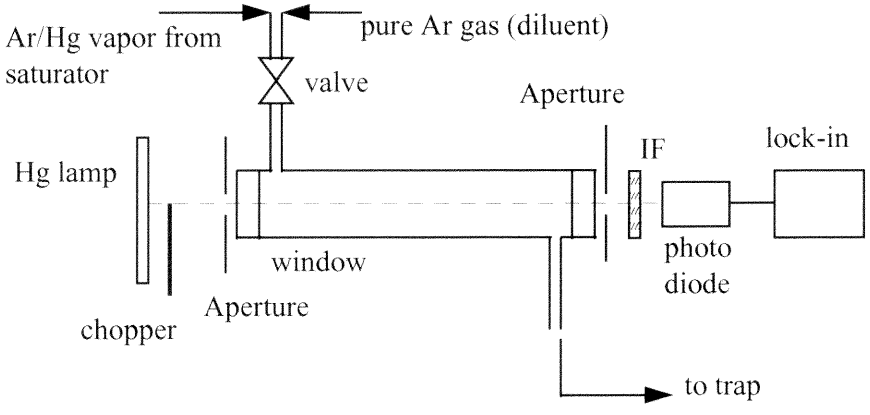

Figure 3.9 Experimental set-up for absorption of Hg vapor from mercury/Ar saturator investigated in a one atmosphere flow cell. (IF: interference filter at 253.65nm with bandwidth of 10nm)

The light source for these absorption experiments is a Double Bore low pressure mercury pencil lamp manufactured by the Jelight, Inc. The lamp consists of a small U-shaped quartz tube filled with natural Hg and Ar at a low pressure, and is operated in AC mode at a low current. Hg pencil lamps are commonly used for alignment and calibration of spectrometer systems in the visible and UV regions. The measured output power drift of this Double-Bore lamp is within 1.6%. Constant output power of the light source is vital for an absorption experiment, particularly when the concentration of absorption medium is very low. This is one reason that Hg pen lamp rather than the on-site laser system is chosen as light source for absorption experiment. Secondly, as will be discussed

later, the Hg lamp is a spectral narrower light source than the laser, and narrow linewidth increases the absorption efficiency.

The dependence of mercury vapor concentration N (mmHg) upon temperature T (Kelvin) follows[26]:

$$N = 10^{-\frac{3813}{T}+10.383} \tag{3.40}$$

By differentiate Eq.3.40, the value of ΔN when T=273K,

$$\Delta N = 4.77\times10^{-6}\Delta T \tag{3.41}$$

If $\Delta T=1^{\circ}C$, then $\Delta N=4.77\times10^{-6}$ mmHg corresponding to $1.65\times10^{17}\ \frac{1}{m^3}$.

Using the Beer-Lambert absorption Law,

$$I = I_0 e^{-\sigma NL} \tag{3.42}$$

where I_0 is the light intensity before absorption, I is the light intensity after absorption, σ is absorption cross-section, and is equal to 3.3×10^{-18} m^2 at 253.7 nm [9]. L is the absorption length. For the static cell, the absorption length is 15 cm. Differentiate Eq.3.42, then

$$\frac{dI}{I} = -\sigma L dN \tag{3.43}$$

when $dN = 1.65\times10^{17}$ m^3,

$$\frac{dI}{I} = 8\% \tag{3.44}$$

Calculation of Eq.3.44 shows that when mercury vapor temperature increases $1^{\circ}C$, light intensity after absorption will drop about 8%. In the other words, if the drift of light source intensity is beyond 8%, any difference in intensity when mercury vapor

temperature only changes 1°C can not be distinguished. With its strong stability (1.6%), the mercury pen lamp is good for performing absorption experiments.

The optical cell for this absorption experiment is the same one used for the photofragment fluorescence experiments with $HgBr_2$ in chapter 2. It is heated and always kept at a temperature at least 10 °C higher than the saturator. All gas transfer lines are heated as well. Hg vapor mixed with Argon gas goes through the optical cell which is open to atmosphere and causes the light absorption being observed. The absorption is monitored at 253.7 nm. The lock-in amplifier is used to detect the variation of light intensity due to the absorption.

The first experiment done for Hg concentration calibration is the investigation of the effect of gas flow rate through the saturator on Hg concentration. Figure 3.10 shows the variation of transmitted light intensity at 253.7 nm with Ar flow rate and saturator temperature. Since this is an absorption experiment, minimum transmitted light corresponds to maximum Hg concentration. When transmitted intensity is independent of flow rate, it is likely the Ar is saturated with Hg vapor (i.e. phase equilibrium). From Figure 3.10, in the case of low Hg fluid temperature, only a narrow flow rate range of Ar gas likely achieves phase equilibrium with Hg vapor. The increased Hg vapor available at high temperature accommodates a wider flow rate range. When the Ar gas flow rate is too low (less than about 1.5 cm^3), poor gas mixing between the Ar exiting a frit and the Hg vapor coming off the liquid results in a low Hg concentration. Thus, the transmitted intensity is high (low absorption). On the other hand, if Ar gas flow rate is too high, although gas mixing inside saturator is good, there is not enough time to achieve phase equilibrium, which results in a low Hg concentration and high transmission. However,

once Hg fluid becomes hotter, the saturation of Hg vapor with carrier gas is easier. This gives a broader range of flow rate for phase equilibrium as seen in Figure 3.10. Comparing the curves in Figure 3.10, Ar flow rate of 3 cm^3/second is observed good for Hg saturation at all available temperatures.

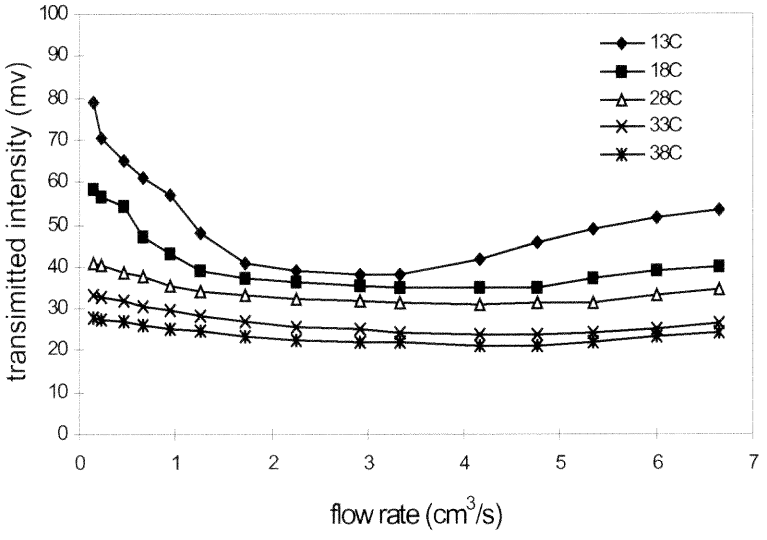

Figure 3.10 Light intensity vs. Ar flow rate through the Hg saturator of absorption experiment in atmospheric flow cell.

With the knowledge of a proper flow rate setting for Hg saturation in this particular saturator, investigation of light absorption using different Hg saturator temperatures (vapor concentrations) in the flow cell is the next step toward calibration of the Hg vapor. Prior to the absorption experiment, linearity of the photodetector has been verified with a neutral density filter. Figure 3.11 shows the result of this investigation, where I_0 is the light intensity with no Hg vapor in flow cell and I is the transmitted light intensity in the presence of Hg vapor. The intensity signal I_0 is easy to get by simply flowing pure Ar gas through the 1 atm optical cell. In Figure 3.11, the Hg saturator

temperature is selectively controlled by the circulator in the range of 10°C to 35°C corresponding to Hg vapor pressure of 0.00045 mmHg to 0.0038 mmHg respectively.

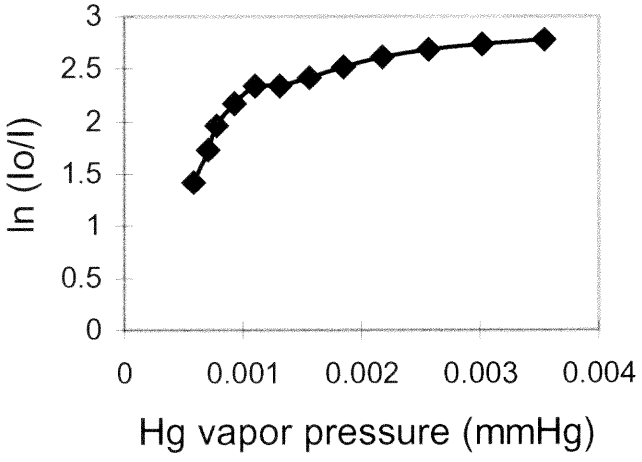

Figure 3.11 The dependence of absorbence $\ln(I_0/I)$ upon Hg vapor concentration in the atmospheric flow cell.

However, Figure 3.10 and Figure 3.11 together did not indicate whether or not the vapor stream is well saturated and is solely determined by temperature. It only indicates that the absorption under the best equilibrium that the experimental set-up can provide. In order to make sure the experimental set-up and preferred operating condition (flow rate) do meet the requirement for Hg vapor saturation, a similar absorption experiment is set up, but is in a static cell (no flow) as shown is Figure 3.12. A static cell eliminates any mixing or mass transfer considerations.

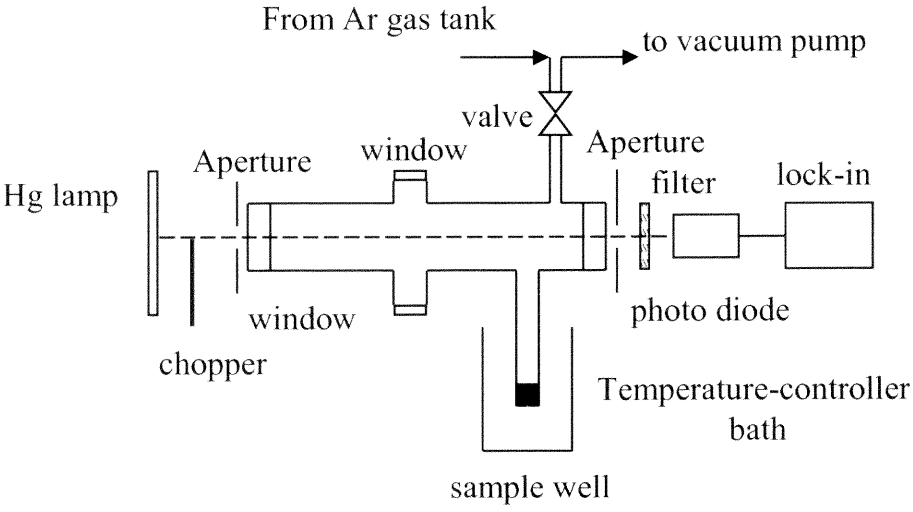

Figure 3.12 Experimental set-up for absorption in a static cell (no flow)

In order for a fair comparison with the result from flow cell experiments, the static cell is first evacuated and then filled with 1 atm Ar to generate the same experiment parameters except for the flow. The light source and detection system are same for both static cell and flow cell cases. The static cell is heated and kept at least 10°C higher than the sample well. The sample well is dipped into a water bath with heating coil controlled by a circuit with a thermocouple. In the static cell, I_0, which is the light intensity with no Hg vapor in presence, is obtained by vacuum pumping the cell while keeping the well (source) in ice water but the walls of static cell at 80°C. Prior to this experiment, linearity of the photodiode has been confirmed as well. Figure 3.13 shows the results of the absorption experiment in a static cell where sample well temperature is varied from 0°C to 42°C corresponding to Hg vapor pressure of 0.00019 mmHg to 0.0061 mmHg. In order to fairly compare this curve with the result from flow cell absorption experiment, the x-axis of Figure 3.13 is Hg atom density (N) multiplied by absorption pass length (L). In this

way, the effect of different lengths in flow cell (19cm) and static cell (15cm) on the absorption intensities can be corrected.

Comparing the two absorption experiment results in Figure 3.13, it is found that they match each other very well. Therefore, the current Hg vapor generating system (the saturator) does provide saturated sample vapor and its concentration can be determined by setting the saturator bath temperature and the Ar flow rate at or near 3 cm^3/second.

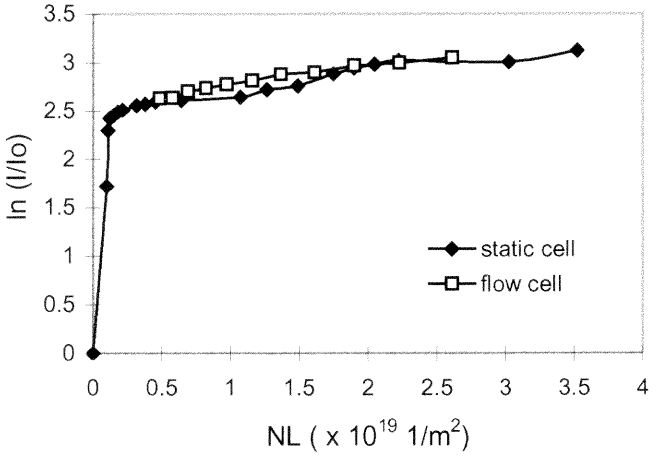

Figure 3.13 Comparison of absorption in static cell and flow cell.

3.3.3 Theoretical Simulation of Absorption Experiment

An interesting phenomena worth of mention in the above flow cell and static cell absorption experiment is that the absorbence ($\ln\frac{I_0}{I}$) plot is very non-linear while the detector response is still in the linear region. As expected from the typical Beer Lambert Law formula:

$$\ln\frac{I_0}{I} = \sigma N l \tag{3.45}$$

Thus, $\ln\frac{I_0}{I}$ should be a linear function of NL. However, what has really been seen in the experiment is termed a non-linear absorption phenomena.

(a) What is a Non-linear Absorption?

When the center of the source line and the absorption line are at the same wavelength, but the Full Width at Half Maximum (FWHM) of the source line ($\Delta\lambda_s$) is narrower than that of the absorption line ($\Delta\lambda_{absorp}$), the entire light intensity under the source line is absorbed in accordance with Beer Lambert Law. Figure 3.14(a) illustrates this linear absorption. The FWHM is also called the linewidth. However, if the source linewidth is much broader than that of the absorption linewidth as shown in Figure 3.14(b), only a small fraction of the band of radiation overlapped with the absorption line is absorbed, and a large portion of unabsorbed light falls within the detector. This results in a nonlinear plot of $\ln(I/I_0)$ vs. concentration. This type of absorption is the non-linear absorption.

The non-linear absorption can be roughly explained in the following way when source line is broader than the absorption line. Incident light intensity I_0 can be written as

$$I_0 = I_n + I_b \tag{3.46}$$

where I_n is the intensity falling into the absorption line, I_b is the intensity outside the absorption.

The detected light intensity I_{det} can be written as

$$I_{det} = I_a + I_b \tag{3.47}$$

where I_a is the residual intensity within the absorption but transmitted (not absorbed)

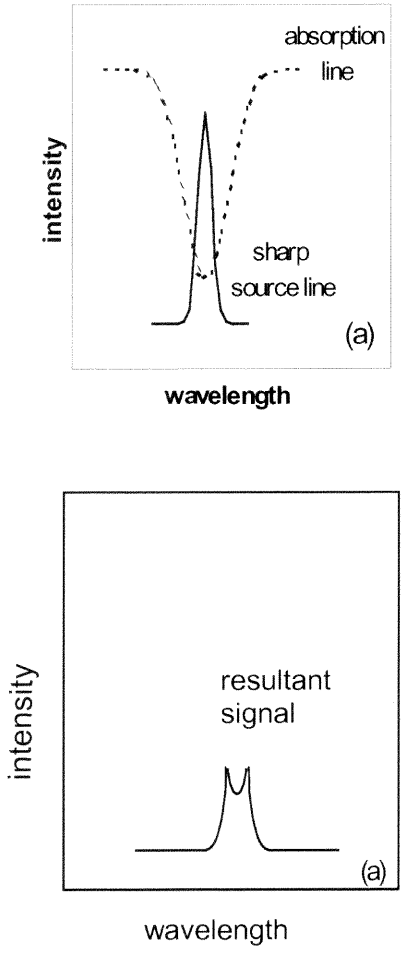

Figure 3.14a Atomic absorption when $\Delta\lambda_s < \Delta\lambda_a$ ($\Delta\lambda_s$ is the linewidth of light source and $\Delta\lambda_a$ is the linewidth of absorption line)[48].

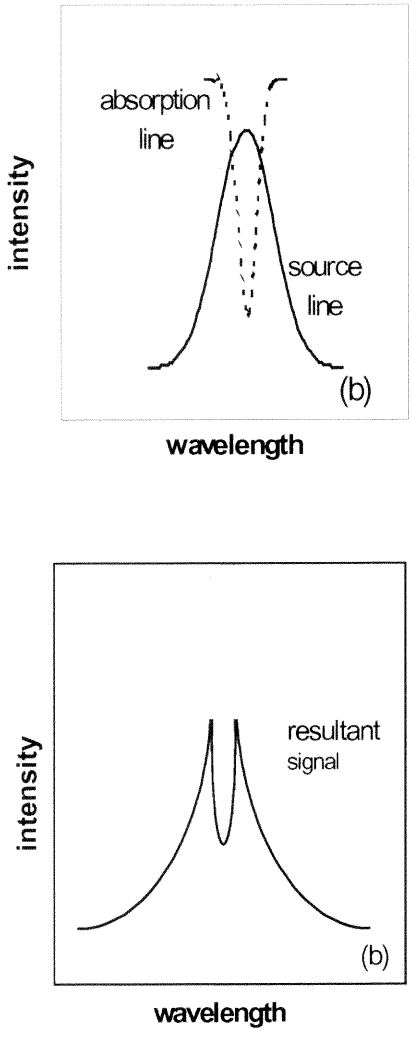

Figure 3.14b Atomic absorption when $\Delta\lambda_s > \Delta\lambda_a$ [48] ($\Delta\lambda_s$ is the linewidth of light source and $\Delta\lambda_a$ is the linewidth of absorption line)[48].

.

Then,

$$\ln \frac{I_0}{I_{\text{det}}} = \ln(\frac{I_n + I_b}{I_a + I_b}) \tag{3.48}$$

where

$$\ln \frac{I_n}{I_a} = \sigma N l \tag{3.49}$$

Therefore, when concentration (N) of absorption medium is high, I_a is low and I_a+I_b will approach I_b and becomes effectively constant. As a result, plot of $\ln \frac{I_0}{I_{\text{det}}}$ vs. concentration will become flat in the higher concentration range. Figure 3.15 illustrates the difference between the absorption of a narrow source and a broad source.

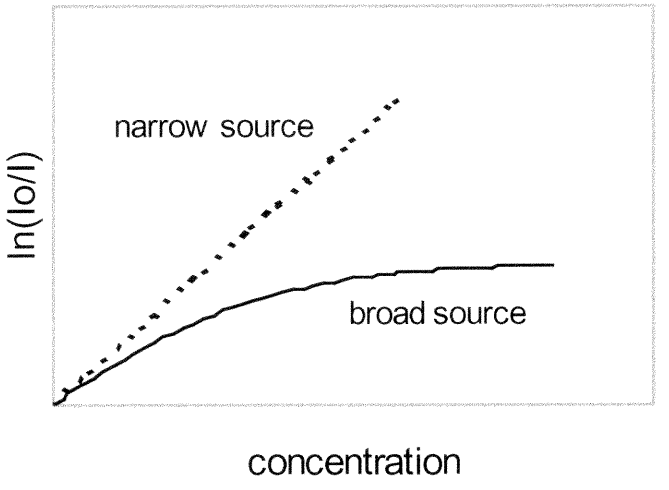

Figure 3.15 Comparison of linear absorption (source is spectrally narrow) and non-linear absorption (source is broad)[48].

(b) Simulation of Light Absorption in Static cell/flow cell

Since a non-linear Beer's law behavior is observed, this suggests that Hg pen lamp is spectrally broader than the Hg vapor absorption in the flow cell. For the calculation of non-linear absorption, the Beer- Lambert Law is still valid, but the linewidths of the light source and the absorption must be considered. Then, the non-linear absorption shall obey:

$$I = \int_{-\infty}^{\infty} I_0(\lambda) e^{-\sigma(\lambda) NL} d\lambda \tag{3.50}$$

where I is the light intensity detected by photodiode, I_0 is the incident light intensity with dependence on wavelength, σ is the absorption cross-section which depends on wavelength as well.

For the absorption experiment in static cell/flow cell, the light source is a mercury pen lamp. Its emission at 253.7 nm follows a Gaussian profile with linewidth of 0.0018 nm from reference [39]. Therefore, $I_0(\lambda)$ can be written:

$$I_0(\lambda) = I_0 e^{\frac{-4(\lambda-\lambda_0)^2 \cdot \ln 2}{(\Delta\lambda_1)^2}} \tag{3.51}$$

where I_0 is the amplitude of light intensity at 253.7 nm, λ_0 is the center wavelength of the absorption (253.7 nm), $\Delta\lambda_1$ is the linewidth of the lamp.

Assume the absorption of Hg vapor in the static cell is Doppler broadened (Gaussian profile) with a linewidth $\Delta\lambda_2$. Then the Hg absorption cross section $\sigma(\lambda)$ is:

$$\sigma(\lambda) = \sigma_0 e^{\frac{-4(\lambda-\lambda_0)^2 \cdot \ln 2}{(\Delta\lambda_2)^2}} \tag{3.52}$$

where σ_0 is the amplitude of the absorption cross-section at 253.7 nm, and is equal to 3.3×10^{-18} m^2 [9].

The infinite integral (Eq. 3.50) can be reduced to $\lambda_0 \pm \frac{\Delta\lambda_1}{2}$. The detected light intensity I can be simplified:

$$I = I_0 \int_{\lambda_0 - \frac{\Delta\lambda_1}{2}}^{\lambda_0 + \frac{\Delta\lambda_1}{2}} e^{\frac{-4(\lambda-\lambda_0)^2 \cdot \ln 2}{(\Delta\lambda_2)^2}} \cdot e^{-\sigma(\lambda)\cdot N \cdot L} d\lambda \qquad (3.53)$$

Eq.3.53 is numerically solved using MathCAD software. The solid line curve in Figure 3.16 gives the calculated function of $\ln(\frac{I_0}{I})$ vs. Hg density N when lamp linewidth $\Delta\lambda_1$ is 0.0018 nm and mercury absorption linewidth $\Delta\lambda_2$ assumed is 0.0007 nm. The diamond curve gives the experimental result. In the high concentration range (N >10× 10^{19} m^{-3}), simulated absorption curve fits experimental result better than in the low concentration range (source temperature is below 16°C).

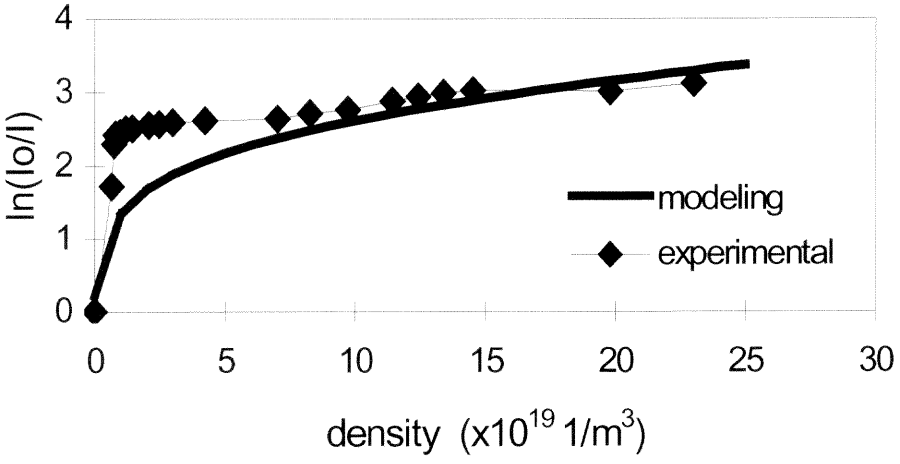

Figure 3.16 Comparison of experimental static cell and simulated results on absorbence ln (I_0/I) as a function of Hg density.

The deviation as seen in figure 3.15 may origins from the Hg lineshape assumption. The Doppler linewidth of Hg at room temperature is 0.00021nm [27]. The Lorentzian width of Hg with 1 atm Ar can be calculated at about 0.00005nm based on hard sphere model [38]. The actual collision broadened linewidth can be larger, by as much as an order of magnitude, than those calculated in the hard sphere model [38]. In simulation of the absorption in static cell/flow cell using MathCAD, the modeling under the assumption of a Lorentzian (collision broadened) absorption line has been tried. But it gives even more deviation from the experimental results. Thus, the real lineshape function of Hg in the experiment may be in a Vogit profile, a more complicated mathematical function which is not calculated here.

3.4 Detection of Resonance Fluorescence of Elemental Mercury in a Supersonic Jet

3.4.1 Experimental Apparatus

With the completion of laser source calibration and sample concentration calibration, detection of resonance fluorescence of atomic mercury at 253.7 nm in a supersonic jet is next. The research apparatus for the study of atomic resonance fluorescence in a supersonic jet is shown in Figure 3.17.

(a) Sample Vapor

Argon gas saturated with Hg vapor leaves the saturator. The vapor pressure of Hg is established by the temperature of the bath surrounding the saturator and is based on published vapor pressure/temperature data (Claussius-Clapyeron relations) [26]. The lines leaving the saturator are held at 10°C higher than the bath to prevent condensation. An

additional Ar bypass stream provides dilution of the vapor stream, and is used to get a background (blank) signal. The combined streams flow to a supersonic nozzle leading to an evacuated chamber.

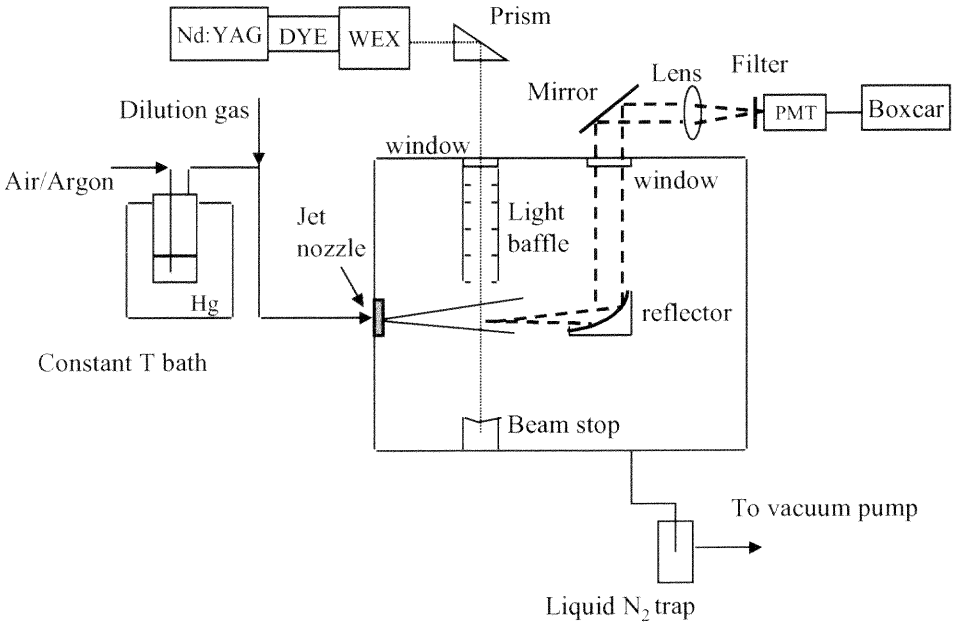

Figure 3.17 Schematic of the experiment set-up for the study of atomic resonance fluorescence in an expanding jet.

(b) Nozzle

The supersonic converging nozzle is manufactured by Beam Dynamics, Inc. originally as a skimmer for production of molecular beams. By grinding the pointy end of the skimmer cone flat to expose an orifice of the desired I.D., a skimmer then becomes a converging nozzle as shown in Figure 3.18. In the experiment, the diameter of nozzle orifice is 200 um with an interior conical angle of 25°. This nozzle is made of nickel, and is operated at room temperature in the resonance fluorescence experiment. In order to have the ability to

adjust the nozzle position, a x-y translation stage is attached onto the front surface of vacuum chamber. The movable distance of this supersonic nozzle is 2 cm in both x (horizontal) and y (vertical) direction.

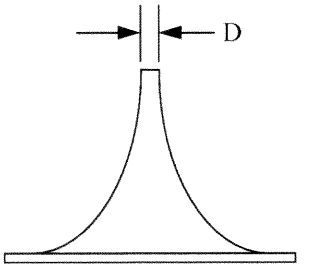

Figure 3.18. Schematic drawing of nozzle.

As discussed in section 3.1.2, the dependence of Mach number on axial distance for a monatomic gas in the isentropic expansion region follows:

$$M = 3.26(\frac{x}{D})^{\gamma-1} \tag{3.54}$$

Combining Eq.3.10 with Eq.3.54 where P_0= 1atm and D=0.02cm, a theoretical jet terminal position (free molecular flow) for the 200 μm nozzle is:

$$x_T = 25D = 0.5cm \tag{3.55}$$

Using the ambient pressure P_b is 60 milltorr of the vacuum chamber with flow in the nozzle in Eq.3.12, the theoretical Mach disk comes at:

$$x_m = 0.67D(\frac{P_0}{P_b})^{0.5} = 1.6cm \tag{3.56}$$

Eq.3.55 and Eq.3.56 together describe the theoretical predicted jet properties of the 200 μm nozzle. When nozzle-to-excitation distance is less than 5 mm, the gas flow is expected to undergo an isentropic expansion. After downstream distance of 0.5 cm, the gas flow is in the "frozen zone" with expected no collision till the Mach disk comes at jet downstream distance of 1.6 cm as shown in Figure 3.2.

(c) Pumping

An Edwards rotary pump is used to generate a vacuum environment in the testing chamber. Its pumping speed is 1.13×10^4 cm^3/s. In the experiment, the nozzle entrance pressure is always kept at 1 atm. This condition is set to meet the requirement of a practical atmospheric application of this detection method; for example, extracting sample gas from a stack at one atmosphere and then injection. Venting to one atmosphere pressure, this pump will reduce the testing chamber pressure to 10 milltorr without gas flow in the nozzle and 60 milltorr with a typical gas flow through the nozzle (about 3 cm^3/second). With the capacity of this pump, the gas flow through the converging nozzle is choked. It is supersonic, following an isentropic expansion out of the nozzle.

(d) Laser Radiation

In this resonance fluorescence detection of atomic mercury vapor in a supersonic jet, the laser system generates UV radiation at 253.7 nm with typical power of 1.0 mW and a beam size of approximately 3 mm × 5 mm (unfocused). The beam is pulsed (10Hz), with pulse duration of 10 nanoseconds. This UV beam crosses the supersonic beam at a right angle. In the experiment, the laser beam crosses the gas flow at different nozzle-to-

excitation distances. The change of laser excitation position is achieved by moving the nozzle in or out relative to the vacuum chamber while the laser beam is fixed.

The resonance fluorescence is monitored at the same wavelength as that of the excitation (253.7nm). The strong elastic (same wavelength) scattering from the chamber wall, entrance window, nozzle and light collection optics due to the laser radiation is a major problem to fluorescence detection, and needs to be reduced as much as possible. Therefore, much effort has been put into reducing the background scattering to increase the fluorescence detection sensitivity. A light baffle is installed below the laser beam entrance window to reduce the forward scattering entering the excitation area of the jet. After the exit window of the chamber, all fluorescence collection optics are installed inside a black tube to reduce the scattering light entering the PMT. The supersonic nozzle is also wrapped with black tape to reduce scattering.

(e) Fluorescence Collection and Detection

The fluorescence is detected in the direction of supersonic gas flow, but at a right angle to the laser beam. An off-axis parabolic reflector, which is installed on an optical rail, is used to collect the fluorescence emission and reflect it into a collimated beam. This parallel beam exits the chamber through a window. It is then reflected again by a mirror mounted over the exit window, and focused into the PMT. The alignment of the fluorescence collection and detection optics is accomplished by using scattering light at 253.7 nm. In this procedure, a glass rod replaces nozzle. The laser beam hits the glass rod generating strong elastic scattering. By adjusting the position of glass rod through the plane translation stage and adjusting the position of reflector, mirror and focusing lens,

scattering light collection can be optimized. Meanwhile, fluorescence collection is optimized.

For resonance fluorescence detection in this experiment, time-gating is used to separate resonance fluorescence from the background scattering. Each laser pulse generates a short-lived background scattering, but the fluorescence from the atomic mercury lasts much longer although it is much weaker. In the experiment, a Boxcar gated integrator is used to delay photon counting and pick up the fluorescence signal.

3.4.2. Investigation of Time-resolved Resonance Fluorescence

(a) Experimental Time Evolution of Resonance Fluorescence and Background Scattering

In order to get details about the experimental density drop in a supersonic gas flow and its contribution to the increase of fluorescence intensity, the time-resolved resonance fluorescence at different nozzle-to-excitation distances is investigated first. As mentioned before, control of the properties of supersonic flow from a converging nozzle is done by choking the flow. Once the flow is choked, its characteristics are fixed and independent of the ambient pressure of the vacuum chamber in its isentropic expansion region. On the other hand, this means the density of the expansion gas downstream of the nozzle can be theoretically predicted. A reference work in the jet-cooling technique uses a pitot tube and fast thermistor to measure gas velocity and temperature, respectively [40]. In this doctoral research work, the time decay of resonance fluorescence signal at different nozzle-to-excitation distances is expected to yield density information of interest. As gas density is associated with the rate constant (k) for the fluorescence decay based on quenching theory

and the Stern-Volmer equation (Eq.1.10), therefore the experimental density information on the supersonic gas flow from the 200 μm diameter nozzle can be obtained.

A Stanford Research System Boxcar Gated Integrator is used to detect the resonance fluorescence signal. Its gate is synchronized with the laser pulse. By scanning (moving) this gate along the time evolution of the pulse, each point of fluorescence signal can be recovered. Without an available gate scan module, the Boxcar gate scanning in the experiment is performed manually. This means manually increasing the gate delay to record the fluorescence signal point by point, not continuously. The gate width here can not be set too large. Since the signal is averaged over the gate width; hence, the fast evolution of the pulse signal might lost. In the experiment, the gate width for this application is set at 3ns. In the resonance fluorescence experiment, the PMT detects both background scattering and fluorescence signal. The increment of gate delay is set at 10 ns for scanning the fast background scattering signal, and is set at 30 ns for scanning the long-lasting fluorescence.

Figure 3.19 shows the time decay (waveform) of the combined Hg resonance fluorescence and background scattering signal at 253.7 nm. The laser beam is focused down to a diameter of 0.7 mm. The nozzle-to-excitation distance is 1.2 cm. The PMT is set at 900v; laser power is about 0.02mW; Boxcar gate sensitivity is 50 mv; Hg vapor concentration in Ar is 1.22ppm corresponding to 12 mg/m^3. The background signal (i.e. no fluorescence) is obtained by flowing only Ar gas through the nozzle with its inlet pressure at 1 atm. By subtracting Ar only signal, the time evolution of the fluorescence signal, which is the information of interest, is obtained. As illustrated in Figure 3.19, the observed full width at half maximum (FWHM) of time-dependent background scattering

is about 40 ns. It is much broader than the specified laser pulse duration (10 ns). The time response of the PMT is considered as the factor to cause this broadening. As in any photomultiplier tube, different electron trajectories within the PMT tube can cause the spread of response time [49]. For the Thorn EMI Q 9558B PMT, its specified transit time spread is between 15 and 40 ns. Therefore, the detected background scattering is convoluted with the PMT time response function.

The fluorescence signal as shown in Figure 3.19 lasts much longer than the background scattering. With the installation of light baffle, the ratio of the peak intensity of the background scattering to the fluorescence is about 2:1 under the experimental conditions for Figure 3.19.

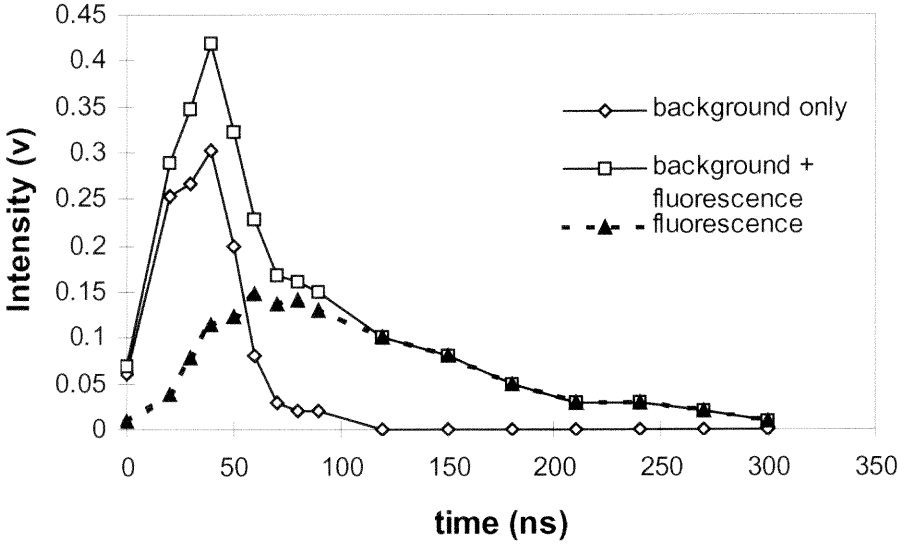

Figure 3.19. Time decay of Hg resonance fluorescence and background scattering when laser crosses the beam at 1.2 cm down the nozzle.

(b) Population Rate Equation Analyzing Time Dependence of Resonance Fluorescence

The fluorescence waveform consists two parts: a short rise, and a long decay. The time dependent fluorescence can be modeled by a population rate equation. In the resonance fluorescence experiment, a two energy level system is considered in Figure 3.20.

The values b_{12} and b_{21} are, respectively, the rate constants for stimulated absorption and stimulated emission, and are related to the atomic absorption cross section σ through the relation [38].

$$b = \sigma\phi \tag{3.57a}$$

$$b_{12} = b_{21} \tag{3.57b}$$

where ϕ is the excitation photon flux (photons/cm^2·sec). A_{21} is the spontaneous emission rate constant, and Q represents the collisional quenching rate constant. Γ_1 and Γ_2 are associated with the inelastic collisions taking all of the atoms out of level 1 and level 2.

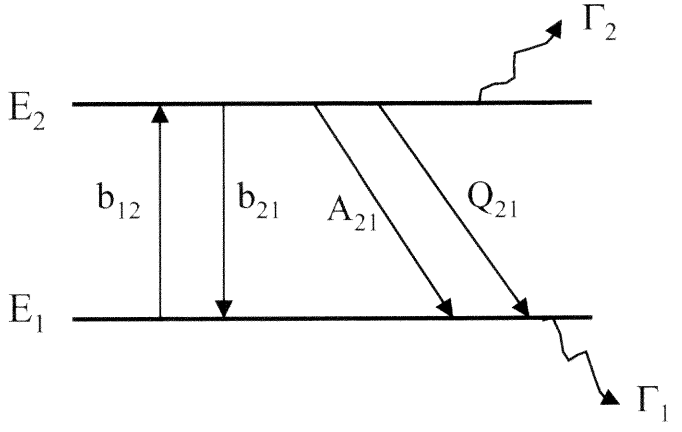

Figure 3.20 Two-energy level diagram for Laser induced fluorescence (LIF) modeling

Writing rate equations for the temporal derivatives of the state population densities, denoted by N_1 and N_2,

$$\dot{N}_1 = -\Gamma_1 N_1 + (A_{21} + Q_{21})N_2 + b_{12}(N_2 - N_1) \tag{3.58}$$

$$\dot{N}_2 = -\Gamma_2 N_2 - (A_{21} + Q_{21})N_2 - b_{21}(N_2 - N_1) \tag{3.59}$$

Γ_1 and Γ_2 are frequently small relative to A_{21} and $\sigma\phi$, and the intermediate-time behavior is of the most interest here. Therefore, the slow influence of Γ_1 and Γ_2 to N_1 and N_2 can be ignored in this case. Eqs.3.58 and 3.59 simplify to:

$$N_1 + N_2 = N = \text{constant} \tag{3.60}$$

$$\dot{N}_1 = (A_{21} + Q_{21})N_2 + \sigma\phi(N_2 - N_1) \tag{3.61}$$

$$\dot{N}_2 = -(A_{21} + Q_{21})N_2 - \sigma\phi(N_2 - N_1) \tag{3.62}$$

where N is the total density in two energy levels and is a constant.

Solving for $N_2(t)$ gives:

$$N_2(t) = [N_2(0) - \frac{N\sigma\phi}{(Q_{21} + A_{21} + 2\sigma\phi)}]e^{-(A_{21}+Q_{21}+2\sigma\phi)t} + \frac{N\sigma\phi}{A_{21} + Q_{21} + 2\sigma\phi} \tag{3.63}$$

Where $N_2(0)$ is the initial (t=0) density of level 2. In the experiment, with average laser power at 1.2 mw at 253.7 nm and a pulse rate of 10Hz , and the beam focused down to a diameter of 0.7 mm, the photon flux is:

$$\phi = 3.9\times10^{17}\ photons/cm^2 \cdot s \tag{3.64}$$

Using the cross section σ at 253.7nm [9]:

$$\sigma\phi = 1.2\times10^4\ \frac{1}{s} \tag{3.65}$$

$$A_{21} = \frac{1}{\tau} = 8.5\times10^6\ \frac{1}{s} \tag{3.66}$$

where τ is the natural fluorescence lifetime and is equal to 1.17×10^{-7} ns [41].

Comparing Eq.3.65 and Eq.3.66 gives:

$$\sigma\phi << A_{21} \tag{3.67}$$

In this case, $N_2(t) << N$. There is a very small excited population and most of the atoms stay in their ground levels. Eq.3.67 indicates that the laser radiation in the experiment is a weak excitation and not enough to saturate the atomic transition.

Based on Eq.3.63, and assuming $N_2(0)=0$, Eq. 3.63 can be simplified

$$N_2(t) = \frac{N_1(0)\sigma\phi}{k_{21}}(1-e^{-k_{21}t}) \tag{3.68}$$

$$k_{21} = A_{21} + Q_{21} \tag{3.69}$$

Eq.3.68 for the cases of with and without a laser pulse is discussed as following:

Case (a): $t << \tau_{pulse}$ (laser pulse width) and for values of $k_{21}t << 1$

The function $e^{-k_{21}t}$ can be approximated in a Taylor series around t = 0 for short time $t>0$ to $1-k_{21}t$. Substitution into Eq.3.68 results in:

$$N_2(t) \approx N_1(0)\sigma\phi t \tag{3.70}$$

This means the upper level population initially builds up linearly with time during the laser pulse excitation and then reaches the value of $N_2(\tau_{pulse})$

Case (b): $t > \tau_{pulse}$

Once the laser pulse has ended, there is no more extend excitation ($\sigma\phi = 0$), Eq.3.68 reduces to:

$$N_2(t) = N_2(\tau_{pulse})e^{-k_{21}t} \tag{3.71a}$$

$$N_2(\tau_{pulse}) = N_1(0)\sigma\phi\tau \tag{3.71b}$$

Eq.3.71 tells that the upper level population will drop in an exponential function after the laser pulse is gone.

With the above analysis of the time dependent fluorescence, the experimental fluorescence curves as shown in Figure 3.19 can be further discussed as following. In the upper level population build-up region, it reaches the maximum when t=60ns, then undergoes an exponential drop. Since the fluorescence pulse as measured is convoluted with the PMT time response, the fluorescence signal rise part is enlonged (delayed).

Based on Eq.3.71, the rate of population exponential decay in Figure 3.17 shall be equal to k_{21}. This rate constant provides to analyze the gas density drop in the supersonic jet. Its relation to the fluorescence lifetime τ in the presence of quenching is [39]:

$$k_{21} = \frac{1}{\tau} \tag{3.72}$$

Combing with Eq.1.11,

$$\frac{1}{\tau} = \frac{1}{\tau_{natural}} + k_q[Q] \tag{3.73}$$

where $\tau_{natural}$ is the natural fluorescence lifetime, k_q is quenching rate constant, and [Q] is quencher density.

Therefore, based on the fluorescence observed decay rate constant k_{21} which can be get from the experimental fluorescence curve, the quencher density information can be retrieved. In the resonance fluorescence work, the quencher is Ar gas. Figure 3.21(a) gives the experimental fluorescence plots at different axial positions relative to the nozzle, where the experimental parameters are: PMT 800v, laser power 0.04mW, laser beam focused with a diameter of 0.7 mm, boxcar sensitivity 50 mv, gate width 3ns, Hg concentration of 1.2ppm. Each fluorescence curve is obtained through same procedures as

illustrated in Figure 3.19. Based on Eqs.3.70, the peak of each fluorescence curve (f_{max}) shall be linearly proportional to the Hg atom density at ground state and fluorescence arise time. When laser pulse width is τ_{pulse}, the ideal time dependent fluorescence curve is expected as Figure 3. 21(b). Due to the jitter of boxcar trigger and boxcar gate delay, fluorescence peaks as shown in Figure 3.21 come at different time. It is not feasible to retrieve the information of gas density at different nozzle-to-excitation distance directly from Figure 3.21(a).

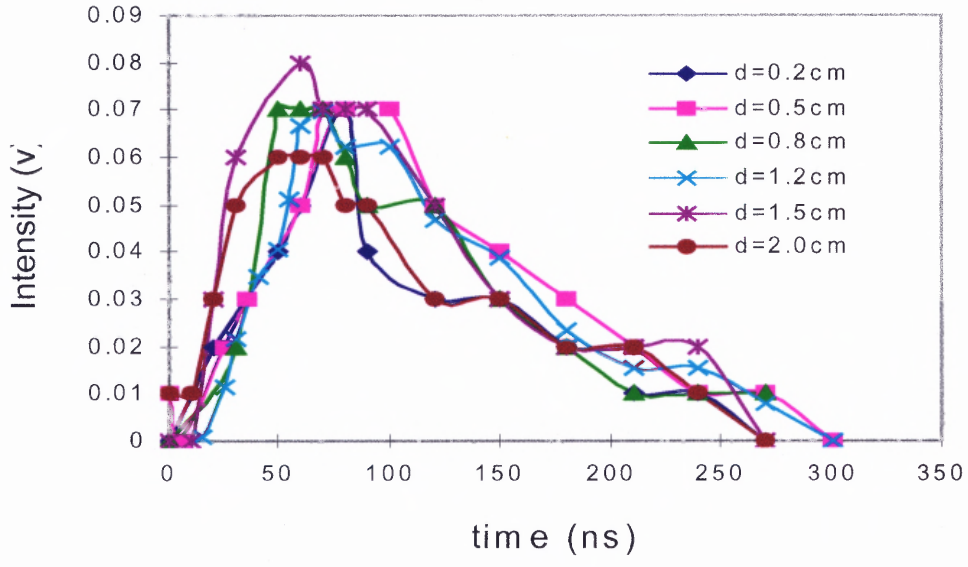

Figure 3.21(a) Experimental time dependence of fluorescence at different nozzle-to-excitation distance.

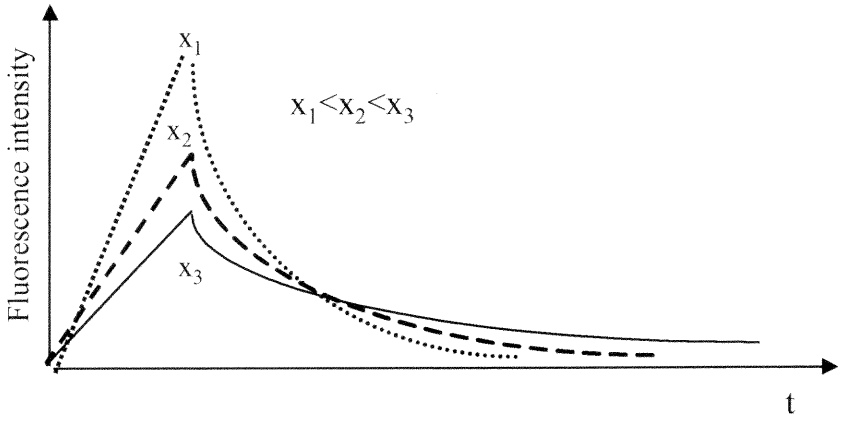

Figure 3.21(b) Theoretical plot of time dependent fluorescence curve (x is the nozzle-to-excitation distance).

An alternative analysis of the data in Figure 3.21 is to integrate the area under each curve. This area represents a spatial summation of all fluorescence falling within the solid collection angle of the off-axis parabolic reflector (see Figure 3.17). Figure 3.22 gives the integrated fluorescence (for each curve) as a function of axial distance (laser beam excitation to nozzle). This integration is calculated using Sigmaplot software(first curve fit of experimental result, then calculate area under the curve). Considering the experimental uncertainty (jitter), the integrated fluorescence at each investigated axial position is roughly the same. One explanation is that, since the laser beam crosses the gas flow at right angle, the total number of Hg atoms in each probe area is constant. This will yields same total fluorescence. In other words, the acceptance cone of the parabolic reflector is big enough to retain the solid angle of fluorescence collection and is not affected by the changing of nozzle-to-excitation distance.

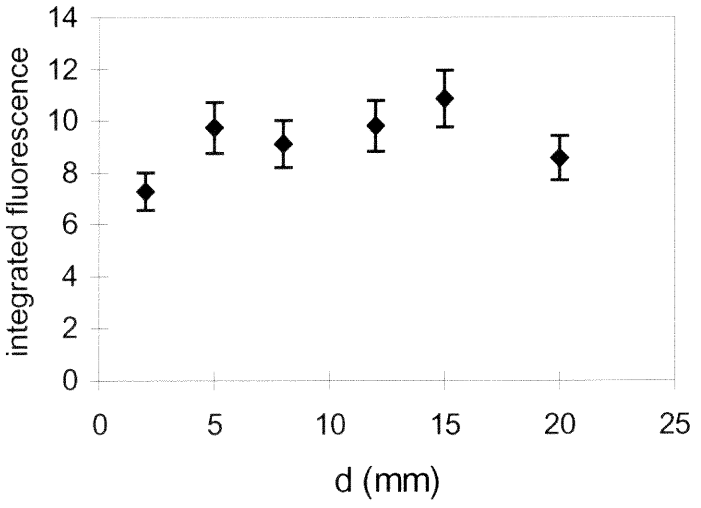

Figure 3.22 Integration of fluorescence vs. axial distance.

(c) Analysis Fluorescence Decay Rate k and its Relation to Density Drop in Supersonic Expansion.

In order to get fluorescence decay rate constant k from the experimental fluorescence curves, the fluorescence plots of Figure 3.21 can be modified by choosing only the data points in the exponential decay region (after the peaks) and plotting those data points on a logarithm scale. Figure 3.23 shows those modified data points in the plot of $\ln(f/f_{max})$ vs. axial distance. Using $\ln(f/f_{max})$ as the correlating function, where f_{max} is the peak of the fluorescence curve, removes the experimental drift in the f_{max} value, thus, giving clearer view of the "true" fluorescence decay rate k.

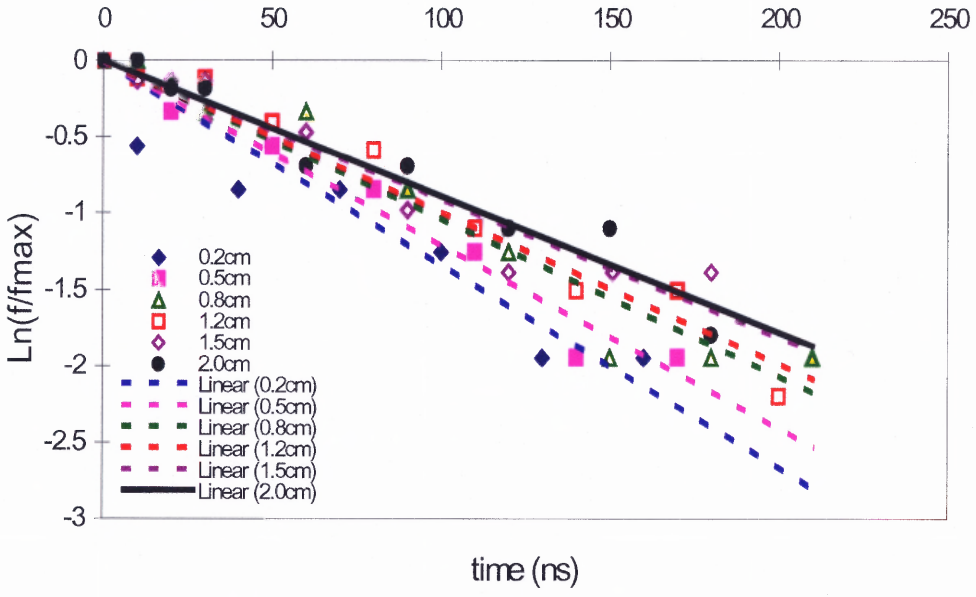

Figure 3.23 Time dependence of $\ln(f/f_{max})$ at different nozzle-to-excitation distance and their linear regressions.

Figure 3.23 clearly shows a definite relationship between the slopes of the lines and the axial distance. Rewriting equation 3.71a yields:

$$\ln(\frac{f}{f_{\max}}) \propto \ln\frac{N_2(t)}{N_2(\tau_{pulse})} = -k_{21}t \tag{3.74}$$

Therefore, the slope of each curve in Figure 3.23 corresponds to the fluorescence decay rate $k = k_{21}$.

As fluorescence lifetime is the inverse of fluorescence decay rate k, Figure 3.24 shows the plot of fluorescence lifetime ($\tau = 1/k_{21}$) as a function of nozzle-to-excitation distance based on results in Figure 3.23. A clear monotonic relation is evident.

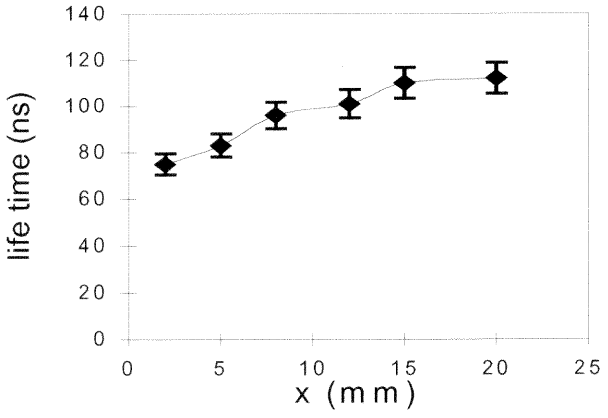

Figure 3.24 The dependence of calculated fluorescence lifetime upon nozzle-to-excitation distance from regression results in Figure 3.23.

The error bars around the points in Figure 3.22 is based on a simple propagation of uncertainty analysis. Since the most important factors affecting the determination of the fluorescence lifetime are the boxcar gate delay and the fluorescence intensity, the measurement error in this fluorescence lifetime can be estimated from [42],

$$(\frac{\sigma_\tau}{\tau})^2 = (\frac{\sigma_t}{t})^2 + (\frac{\sigma_f}{f})^2 \tag{3.75}$$

where σ_τ,σ_t and σ_f are standard deviations of fluorescence lifetime, boxcar gate delay and fluorescence intensity, respectively. In the experiment, the boxcar gate delays has a precision of about 5%. The PMT output drifts about 3% for a fixed input. Combined with an assumed laser power drift of 3%, all these factors together yield lifetime measurement uncertainty of about 7%. Therefore, the maximum fluorescence measured lifetime is 112 ns ± 8 ns. It is very consistent with the reference data for the natural fluorescence lifetime [41], which is 117 ns.

With γ=1.67 for Argon gas, a density drop in Eq.3.7c:

$$\frac{\rho_0}{\rho} = [1 + 3.56 \times (\frac{x}{D})^{1.34}]^{\frac{1}{0.67}} \tag{3.76}$$

where, ρ_0 is the Hg density at the nozzle inlet, ρ is the Hg density at downstream of jet and D is the nozzle diameter which is 0.2mm.

When $\frac{x}{D} >> 0.386$, Eq.3.76 simplifies to

$$\frac{\rho_0}{\rho} = 6.65(\frac{x}{D})^2 \tag{3.77}$$

Eq.3.77 indicates that in the isentropic region of jet expansion, gas density decreases on -axis as $1/x^2$ (x=distance from the nozzle).

Using Eq. 3.77 and substituting [Q] by ρ, Eq. 3.73 can be rewritten in terms of axial distance x:

$$\frac{1}{\tau} - \frac{1}{\tau_{natural}} = \frac{1}{6.65} k_q \rho_0 (\frac{D}{x})^2 \tag{3.78}$$

Reference [43] gives the quenching rate constant k_q of Hg (6^3P_1) with Ar gas as 5.8×10^9 liter/mol·sec.

Therefore, the dependence of fluorescence lifetime on the nozzle-to-excitation distance in the isentropic expansion region is:

$$\frac{1}{\tau} - \frac{1}{\tau_{natural}} = 0.039(\frac{D}{x})^2 \qquad (\frac{1}{ns}) \tag{3.79}$$

Figure 3.25 gives the plot of $\frac{1}{\tau}$ vs. $(\frac{D}{x})^2$ based on experimental results of Figure 3.24. After a linear regression of the plot, a slope of 0.2 ns^{-1} is obtained. Actually there are two different slopes in figure 3.23. The value of the fast slope is 4 for the first several data points, and 0.2 is the slope based on last three data points. Thus, even the slow slope is 10 times greater than the theoretical slope for the isentropic gas expansion. In other words, the gas expansion in the investigated region, where x varies from 2 mm to 20 mm, does not follow the isentropic expansion.

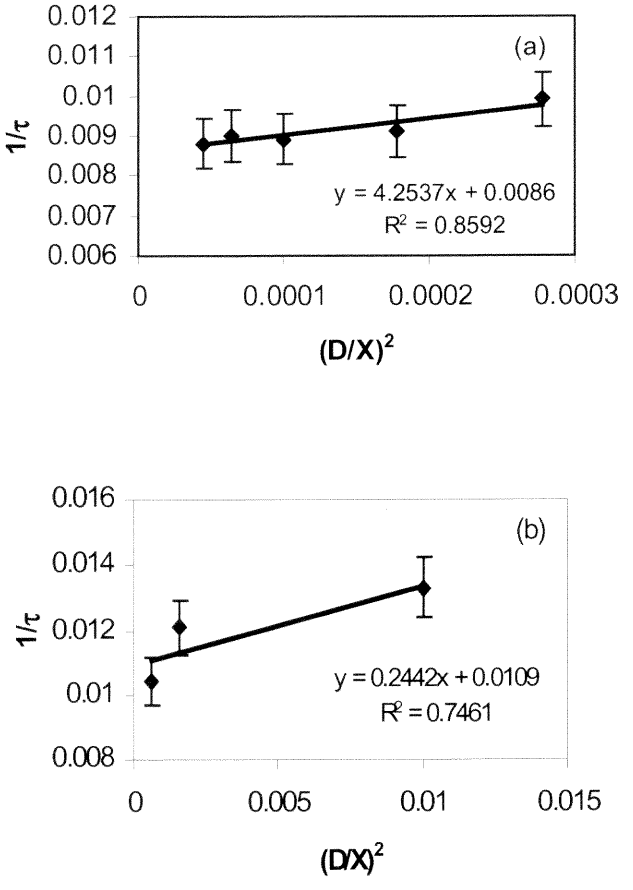

Figure 3.25 Plot of fluorescence decay rate constant k ($1/\tau$) as a function of $(D/x)^2$ (a) nozzle-to-excitation distance x in the range of 1.2cm to 3 cm. (b) x in the range of 0.2 cm to 0.8 cm.

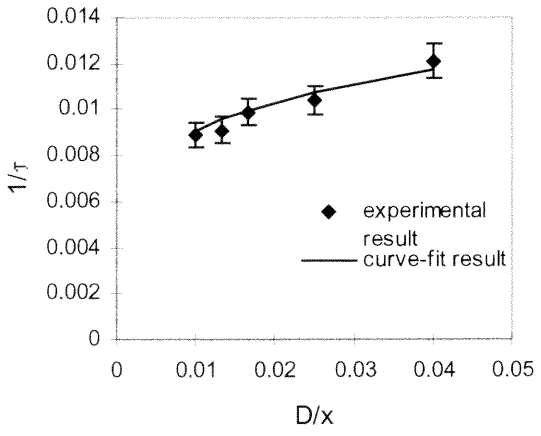

Figure 3.26 Experimental and Sigmaplot fitted dependence of fluorescence decay rate constant k ($1/\tau$) upon D/x where nozzle-to-excitation distance varies from 0.5cm to 2.0cm.

The dependence of the density drop on axial distance in the experiment is re-plotted in Figure 3.26, where x-axis is $\frac{D}{x}$. Using Sigmaplot curve fit the inverse of fluorescence lifetime over the x ranging from 0.5cm to 2.0cm yields

$$\frac{1}{\tau} \propto (\frac{D}{x})^{0.18} \tag{3.80}$$

This means that, in the region of the investigation, gas density undergoes a very slight drop along the jet axial direction. It is not very consistent with the theoretical predication as discussed in section 3.4.1(a).

Anderson and Fenn's "freezing" model for predicting the terminal Mach number M_T [37] says that a terminal Mach number is approached in the jet expansion when there are too few collisions to affect an appreciable change in the velocity distribution. In

addition, the transition to free molecular flow may be treated to be gradual [45]. Therefore, the slow density variation observed from modeling of experimental results may be associated with this gradual transition, which makes the spread of jet beam continue over some distance. On the other hand, the nozzle manufacture (particular the conical angle) has effects on jet cooling efficiency [46] and can cause deviations of real jet expansion from simple theory predictions.

3.4.3 Capabilities of the Supersonic Jet Fluorescence Spectrometer

As mentioned in Chapter 1, the purpose of this doctoral research is to develop real-time monitoring technologies for detection of vapor mercury species emissions. Therefore, the performance of this supersonic jet-based fluorescence spectrometer is investigated here to establish its capabilities and limitations.

(a) Optimization of Excitation in Supersonic Jet

Theoretically in order to take full advantage of the reduced quenching in the jet expansion, the jet should be excited at the position where the product of fluorescence quenching efficiency and gas density yields a maximum. This ideal optimum for argon (carrier gas) in the experiment is shown in Table 3.2, with excitation at the point where M=2 (x=0.7D). However, this theoretical optimal position is too close to the nozzle (D=200μm). Fluorescence detection at this point will not only suffer strong nozzle generated background scattering, but it will be experimentally difficult to control the excitation point. Thus, the optimal excitation is designated at the position where fluorescence quantum yield is approximately unity and gas density does not drop too much.

Since the time gating approach is used to separate background scattering and resonance fluorescence, fluorescence intensity detection with relative finite gate width is of most importance to its performance investigation. Figure 3.27 shows the Hg resonance fluorescence vs. nozzle-to-excitation distance with experimental parameters: PMT 700v, laser power 1.0 mw, laser beam focused down to a diameter of 0.7mm, gate delay 90 ns, gate width 90 ns, sensitivity 20 mv and Hg vapor concentration 1.2 ppm.

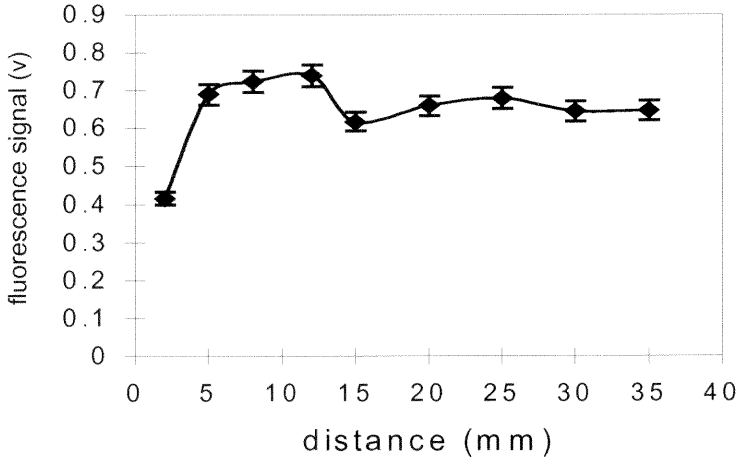

Figure 3.27 Hg resonance fluorescence vs. nozzle-to-excitation distance when boxcar gate delay is fixed at 90 ns, and gate width is set at 90 ns.

The detected resonance fluorescence intensity at a nozzle-to-excitation distance of 2 mm is much less than all others with greater nozzle-to-excitation distance, as shown in Figure 3.27 . In the region of axial distance of 5 mm to 12 mm, detected resonance fluorescence is roughly constant. With a slight amplitude drop at distance of 15 mm, detected resonance fluorescence becomes constant again. Eqs.3.55 and 3.56 tell that gas flow undergoes isentropic expansion and tremendous density drop within the downstream

distance of 5 mm from the 200 μm nozzle. In the region of downstream distance of 5 mm to 16 mm, gas flow is expected in a no collision zone, which means unity fluorescence quantum yield. Therefore, the low fluorescence intensity at nozzle-to-excitation distance of 2 mm may be due to low fluorescence quantum yield. Although the gas density at this point is high, it can not overwhelm the low fluorescence quantum efficiency. The sudden intensity drop at the nozzle-to-excitation distance of 15 mm may due to the occurrence of the Mach disk.

On the other hand, background scattering must be considered in deciding the optimal jet excitation point. As the PMT detects resonance fluorescence and background scattering at the same time, too much background scattering signal into PMT will cause detection saturation, thus limiting the detection dynamic range. Figure 3.28 gives the peak amplitude of the background scattering signal from oscilloscope readout in the experiment for investigation of time dependent resonance fluorescence. Parameters for that experiment are: PMT 700v, laser power 1.0 mW.

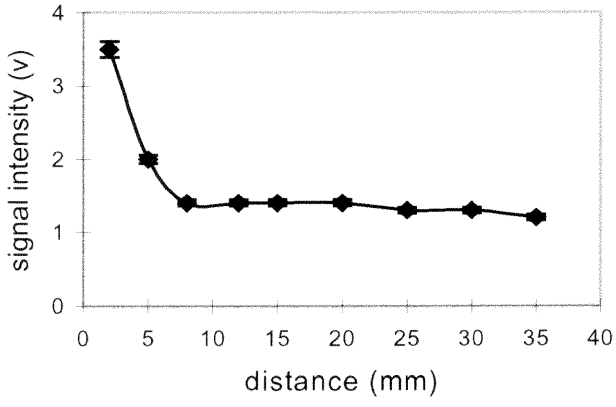

Figure 3.28 Background scattering signal vs. jet downstream distance (same experimental parameters as Figure 3.21).

The background scattering is very strong when the laser excitation point is very close to the nozzle whereas the fluorescence amplitude is not much different (refer to Figure 3.21). In the resonance experiment, it is found that there is no obvious difference in background scattering intensity in the cases of flowing Ar gas through the nozzle or no Ar gas flowing through the nozzle. This means that, in the experiment set-up, elastic scattering from walls, windows, etc rather than any Rayleigh scattering from the gas contributes to the background signal. When laser excitation is close to the nozzle, the nozzle itself generates strong scattering. Once the laser beam is about 10 mm away from the nozzle, the background scattering is effectively at its minimum. Therefore, based on the observations from the above figures, a jet downstream distance of 12 mm is selected as the optimal excitation position for the subsequent resonance fluorescence performance investigations. In addition to a minimum background scattering signal, collisional quenching is gone here.

(b) Fluorescence Signal as a Function of Sample Concentration.

By varying the Hg source temperature, the dynamic range of resonance fluorescence detection is investigated over a wide Hg concentration range. In these runs, the laser beam is unfocused with a power of 1.2mw. The laser crosses the jet at a downstream distance of 12mm, and the PMT is operated at 600v. The Boxcar gated integrator is set at 20 mv sensitivity, 30 samples averaging, 100 ns gate delay. The boxcar gate width is set at 300ns where system noise is observed relatively low.

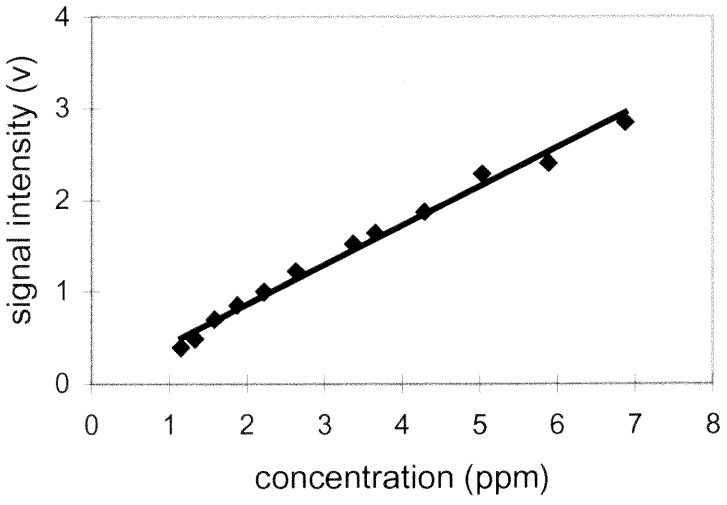

Figure 3.29 Hg resonance fluorescence in supersonic jet as a function of Hg vapor concentration.

In this investigation, the Hg saturator temperature is varied from 16 °C to 38 °C, corresponding to concentration of 1.1ppm (10 mg/m^3) to 6.87 ppm (61mg/m^3) respectively. The results are shown in Figure 3.29. No additional Ar dilution is introduced in order to get higher concentrations of Hg vapor. The observed Hg resonance fluorescence is in good linear response in this concentration range as shown in Eq.3.13. The linear dynamic range for this technique could be extended to higher concentrations using higher source temperatures. For the water circulator, which controls the temperature of Hg saturator, its working range is from 0°C to 100 °C. Due to the high vapor pressure of Hg, a maximum operating temperature of the Hg saturator is set at 40°C for safety reasons.

(c) Fluorescence Signal as a Function of Laser Power

Laser power at 253.7 nm is varied while maintaining constant Hg concentration at 355ppb (vapor pressure of 2.7×10^{-4} mmHg) to investigate the dependence of fluorescence signal with incident power. The variation of laser power experimentally is done by detuning the crystal in the WEX (which is for frequency doubling and mixing), then measured with an on-site power meter. Figure 3.30 gives the dependence of resonance fluorescence intensity with laser power based on experimental parameters of an unfocused laser beam (3mm× 5mm), nozzle-to-excitation distance of 12 mm, 700v PMT, and Boxcar settings of 10 mv sensitivity, 30 pulses averaging, 100 ns gate delay, 300 ns gate width and one-stage preamplifier. For incident power up to 1.2 mW, which is the maximum power the laser system can generate at 253.7 nm, the resonance fluorescence is linear with laser power. This is consistent with Eq.3.13.

The linearity of Figure 3.30 is typical for a one-photon absorption/emission process. The absorption of laser is just as expected since the resonance fluorescence is under monitoring now. In addition, the calculation (Eq.3.64- Eq.3.67) also shows that under the typical laser power condition in the experiment, the laser excitation is a relatively weak, and is not strong enough to saturate transition between $^1S_0$ and $^3P_1$ states, which corresponds to the 253.7 nm atomic emission. If the laser excitation is too strong (strong power/ tightly focused beam, $\sigma\phi\rightarrow$ large in Eq.3.65) and saturates the optical transition, then the population density in two levels are same and equal to $\frac{N}{2}$, where N is the total number of density of the two level system. Thus, with the increased power, no

more fluorescence is yielded. As a result of this, the curve becomes flat in the high power region/ saturation fluorescence). Clearly, by Figure 3.30, it does not happen.

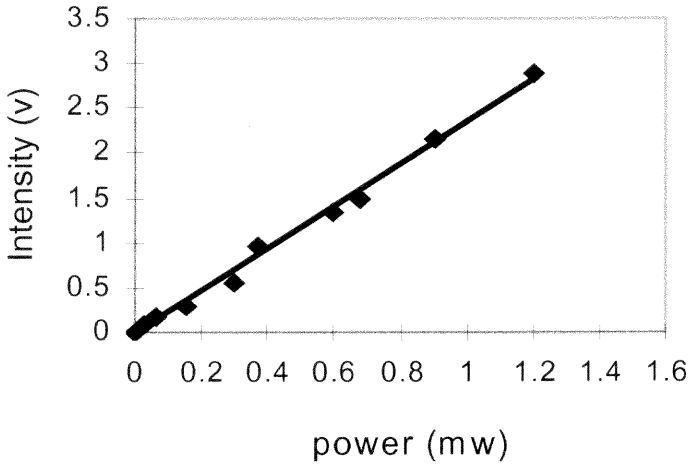

Figure 3.30. The dependence of Hg resonance fluorescence signal upon laser power.

(d) Response Time of the Fluorescence System

Response time is an important factor for a measurement system. Figure 3.31 shows the investigation of this matter with experimental parameters of 1.2 mW laser beam, 700v PMT, nozzle-to-excitation distance of 12mm, unfocused laser beam excitation, and Boxcar settings of 50 mv sensitivity, 100 ns gate delay, 300 ns gate width, one-stage preamplifier and 30 pulses average.

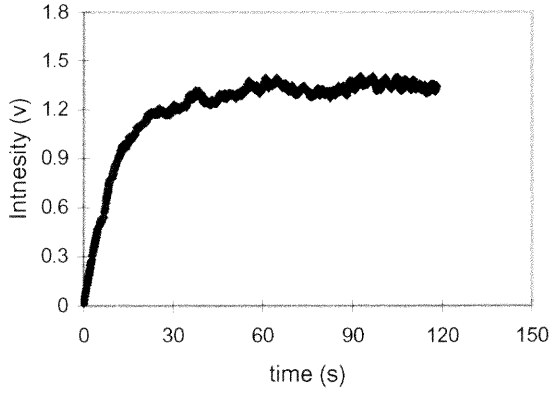

Figure 3.31(a) Time dependence of Hg resonance fluorescence during flow of 0.772ppm Hg vapor into vacuum chamber which initially only Ar vapor was present.

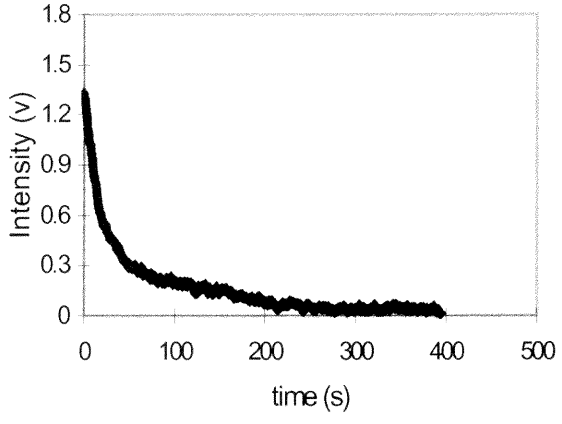

Figure 3.31(b) Time dependence of Hg resonance fluorescence during flow of Ar gas into vacuum chamber which initially was flowed with 0.772 ppm Hg vapor.

Initially, a steady flow of Ar only was flowing at time t=0. Hg vapor with concentration of 0.772 ppm is introduced into vacuum chamber with a flow rate of $3m^3/s$ as shown in Figure 3.31a. It takes about 10 seconds for the fluorescence signal to reach half value, and about 60 seconds for the signal to reach its final value. Figure 3.31b shows the instrument response in the case of introducing Ar only to the vacuum chamber in the same flow rate where the vacuum chamber initially has 0.772 ppm Hg flowing through the

supersonic nozzle; in other words, the Hg is " turned off" and only Ar flows. It also takes about 10 seconds for the signal to drop to half, but about 4 minutes for the vacuum chamber to be completely clean (without Hg vapor). The longer response in the latter case may due to a cold spot inside the nozzle. In the experiment set-up, the nozzle is installed in a tube which goes into the vacuum chamber where the heating tape is not accessible. Some residual condensed Hg in the nozzle might cause this long purge time.

Increasing the flow rate of sample gas could reduce the response time. However, this change in the vacuum chamber experiment will not be as good as in the experiment of $HgBr_2$ detection in the 1 atm flow cell, where the allowable flow rate range for saturation of $HgBr_2$ vapor is much broader. Due to the set-up of Hg vapor saturator itself, the permissible flow rate range is quite limited; otherwise Hg vapor is not well saturated (see Figure 3.10). In addition, if the flow rate is too high, the one atmosphere pressure condition in the nozzle inlet might not be satisfied. Then, the characteristics of the jet expansion will be different. It is important that experimental parameters be consistent.

(e) Detection Limit

The signal-to-noise ratio of fluorescence as a function of Hg concentration is investigated in order to get the detection limit of this monitoring technology. In the previous sections on optical transition and pumping in the two –energy level systems, discussions indicate that a stronger incident power density yields more excited atoms, which will generate more fluorescence photons (upto saturation). The improvement of power density can be obtained by increasing the laser power or/and focusing laser beam tightly. In the

experiment, the laser beam power is generally set at the maximum obtainable power. Therefore, improving optical pumping may be done by focusing the laser beam as much as possible. However, as the fluorescence calculation Eq.3.13 shows, fluorescence intensity is linearly proportional to the path length of laser beam overlapping the jet. With bigger beam size, the optical path length will be longer, and thus increase the fluorescence. Considering these two factors, signal-to-noise ratio of fluorescence is measured under two conditions, focused laser beam excitation or unfocused beam excitation.

The fluorescence collection and detection optics were initially aligned using the unfocused beam scattering off the tip of a glass rod with excitation of unfocused laser beam. With the introduction of a lens, the focused beam might not hit the center of the expanding jet. Thus, the lens for focusing the laser beam is mounted on an x-y-z translation stage with the capability to be optimized. Figure 3.33 illustrates the detected resonance fluorescence while scanning the focusing lens in a direction (y-axis) perpendicular to the gas flow (z-axis) but with the height of the lens fixed (see figure 3.32). Experimental parameters for this experiment are: PMT setting at 700v; laser power: 0.9mw; beam hitting the gas flow at a jet axial distance of 1.2cm; focal length of the lens: 300mm; lens height relative to the beam is 350 mm (the minimum height the system can go); and beam focused down to a diameter of 0.7mm; Hg concentration of 1.2 ppm; and boxcar set at 50mv sensitivity, gate delay of 60ns, gate width of 90ns and 30 samples averaging.

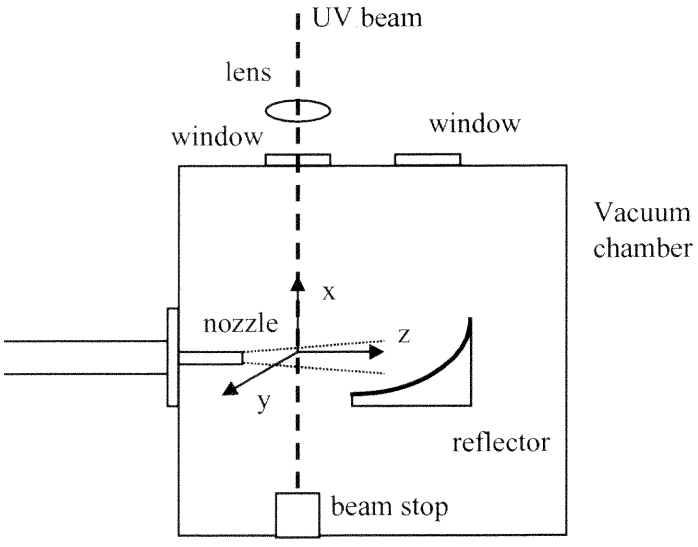

Figure 3.32 Drawing of movement of focusing lens for fluorescence optimization.

In the symmetric plot of Figure 3.33, fluorescence is maximized at the lateral position reading of 0.19 inch. The fluorescence intensity plotted in figure 3.33 had the background signal (the contribution from the scattering light) subtracted. In other words, if the spread of the jet at a downstream distance of 12 mm is roughly 0.3 inch, a zero fluorescence intensity shall be observed in the far wings of Figure 3.30. Thus, the non-zero minimum signal observed here might be associated with the misalignment of the laser beam to parabolic reflector and fluorescence collection optics.

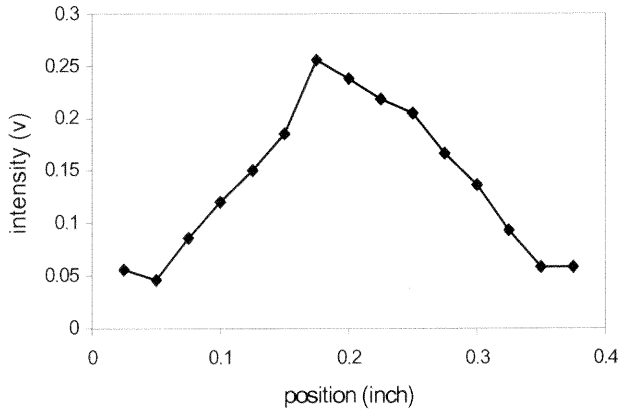

Figure 3.33 Scanning focusing lens in the radial direction of jet expansion for optimization.

Figure 3.34 gives the Hg resonance fluorescence under different degree of focusing of the incoming excitation beam (scan lens in x direction of Figure 3.32). Experimental parameters are: focal length of lens = 300 mm, laser power = 1.5 mW, nozzle-to-excitation distance of 12mm, PMT 700v, boxcar sensitivity 20mv, gate delay 100ns, gate width 300ns, Hg concentration 1.3 ppm. Figure 3.34 shows that a stronger fluorescence is detected when the laser focusing lens is further away from the gas flow (less focusing). Therefore, enlarging interaction volume contributes more to the fluorescence intensity than increasing the optical pumping density.

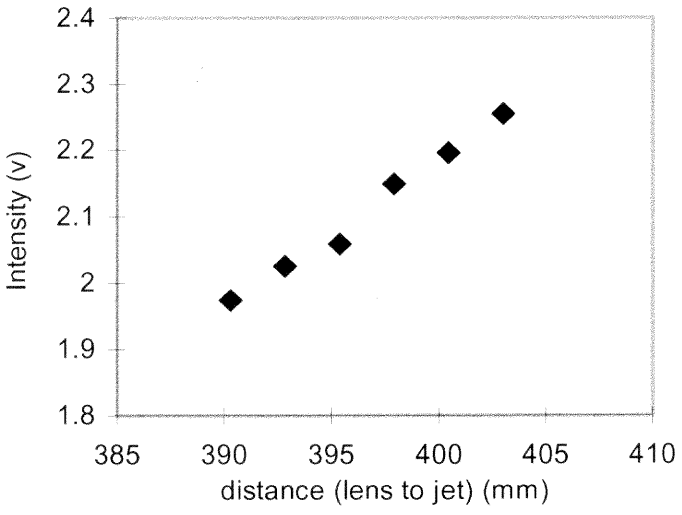

Figure 3.34 Hg resonance fluorescence vs. position of the focusing lens, which is mounted on a translation stage with maximum displacement of 1.5 cm..

In order to improve the performance of the fluorescence signal-to-noise ratio for this monitoring technology, the detection gating needs to be optimized for best experimental results. By varying the gate width, gate delay, boxcar sensitivity as well as the PMT voltage, detection gating is optimized to yield maximum fluorescence output while the noise is kept at low. The obtained "best" gate settings for resonance fluorescence detection are: gate delay of 100ns, gate width of 300ns, and sensitivity of 10mv for low concentrations of Hg detection (<1ppm).

Low concentrations of Hg are needed to estimate the detection limit of the experimental system. They are obtained by using argon dilution while keeping the Hg source temperature low. Since the Hg source has a narrow flow rate range for saturation at low temperatures (less than room temperature), and since nozzle inlet pressure must be one atmosphere, the degree of dilution in this experiment is limited. Thus, the minimum

Hg concentration obtained from the experimental system is 100ppb (parts per billion, by volume). The resonance fluorescence S/N values as a function of Hg vapor concentration are presented in Figure 3.35. Here, the results are based on experimental parameters of: source temperature varying from 0 °C to 18 °C corresponding to 0.25 ppm to 1.3 ppm respectively; bypass dilution ratio of 0.47; PMT 700v; laser power 1.2mW; nozzle-to-excitation distance of 12 mm; boxcar gate delay 100ns, gate width 300ns, sensitivity 10mv, and 30 samples averaging with one-stage preamplifier. The boxcar gate setting here is the optimal case. By extrapolating the concentration back to S/N=2, the estimated detection limit is 3ppb for unfocused laser excitation and is 6ppb for focused laser excitation where the height of lens (f=300mm) is 350mm relative to the gas flow. Since the unfocused beam gives stronger resonance fluorescence at the same concentration, therefore, a better detection limit is obtained in this case.

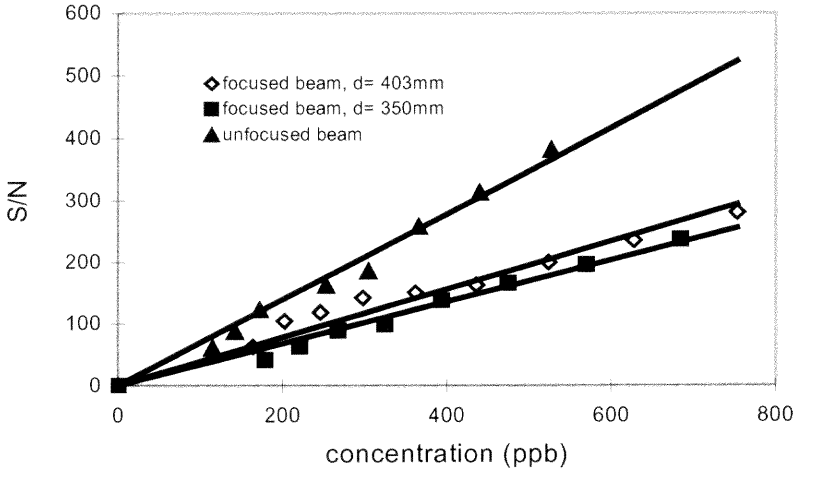

Figure 3.35 The dependence of S/N upon Hg vapor concentration (d: distance between focusing lens and jet).

Increasing the number of averaging samples of the Boxcar gated integrator can improve the detection limit of this system. However, increasing the averaging sample will enlong the duty cycle of this measurement system (3 seconds with 30 averaging samples), which is not helpful to real-time monitoring application. Therefore, other options such as reducing the instrument noise and increasing the excitation laser power need to be considered.

CHAPTER 4

ULTRAVIOLET INTERFEROMETRY FOR DETECTION MERCURY RESONANCE FLUORESCENCE

4.1 Problem Statement and Possible Methods

The second main task in this doctoral research work is to detect elemental mercury in a supersonic jet by resonance fluorescence spectroscopy. In resonance fluorescence, laser excitation and fluorescence are at the same wavelength. They may be separated by time-gating approach as explained in Chapter 3. Time-gating is a useful and simple approach to extracting resonance fluorescence signal from a strong background in the time-domain, but it has some limitations. The primary disadvantage of this method is that only part of the emitted fluorescence can be collected; that is, the portion after the laser scattering pulse has died off. Even with extensive optical baffling to reduce stray light, a portion of the atomic resonance fluorescence signal will be lost.

In order to get a mercury resonance fluorescence detection system with high sensitivity, UV interferometry is investigated here as a potential alternative to replace time-gating. Most of the applications of the interferometry have been in the infrared and visible spectral regions. Little work has been published in ultraviolet (UV) due to the difficulty of alignment at shorter wavelengths. With its prominent analytical lines found in the UV region, atomic mercury is a good candidate for exploring interferometry in the UV.

4.2 Theory of Interferometry to Detect Resonance Fluorescence

The UV interferometry investigated here is based on a Michelson interferometer as shown in Figure 4.1. The Michelson interferometer is a device that can divide a beam of radiation into two paths and then recombine the two beams after a path difference has been introduced. A condition is thereby created under which interference between the beams can occur. The intensity variations of the interfering beams emerging from the interferometer can be measured as a function of path difference (retardation) by a detector. This intensity variation with path difference ultimately yields spectral information using Fourier Transform.

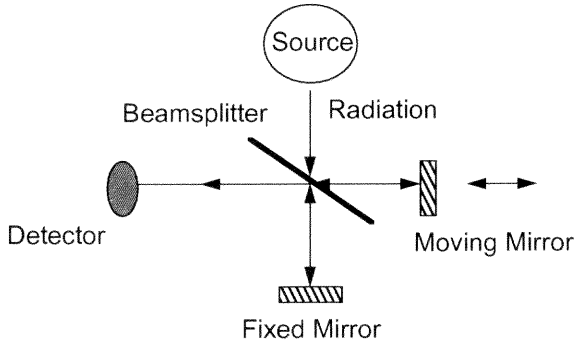

Figure 4.1 An optical diagram of Michelson interferometer

The variation in the intensity of the interfering beams passing to the detector as a function of the path difference is the interferogram. For an idealized light source of infinitely narrow monochromatic radiation, its wave number is $1/\lambda$ (reciprocal centimeters). The interferogram from this ideal source is given by [51]:

$$I(\delta) = (0.5)I(\frac{1}{\lambda})\cos(\frac{2\pi\delta}{\lambda}) \tag{4.1}$$

where I(δ) is the intensity of the beam at the detector, $I(\frac{1}{\lambda})$ is the intensity of the source and δ is the path difference between two beams. Mathematically, I(δ) is said to be the cosine Fourier Transform of $I(\frac{1}{\lambda})$. Figure 4.2 and Figure 4.3 show the simulated interferogram from a narrow light source and a broad light source using MathCAD software (calculation see Appendix A & B). These two assumed light sources are both centered at 253.65 nm with linewidth of $1cm^{-1}$ and $100cm^{-1}$, respectively.

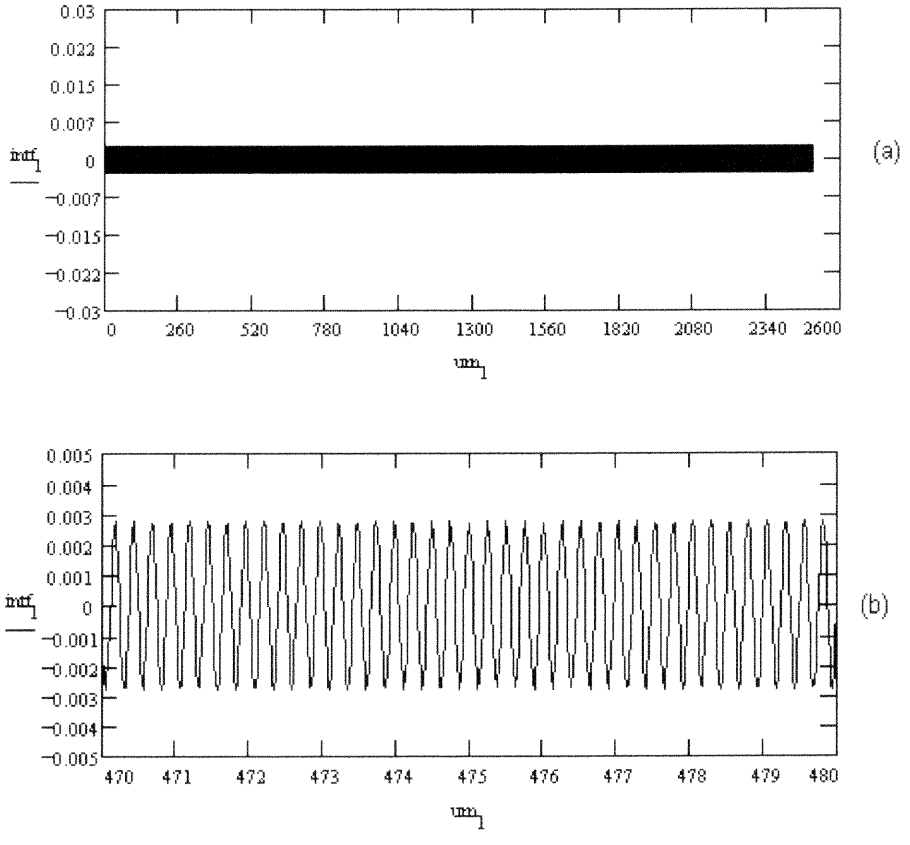

Figure 4.2 Simulated interferogram from narrow source ($1cm^{-1}$ bandwidth at 253.7nm corresponding to bandwidth of 0.01nm) where $intf_i$ is the interferogram intensity in an arbitrary unit and um_i is the mirror displacement in the unit of micron. (a) interferogram in the range of 2μm. (b) expanded interferogram.

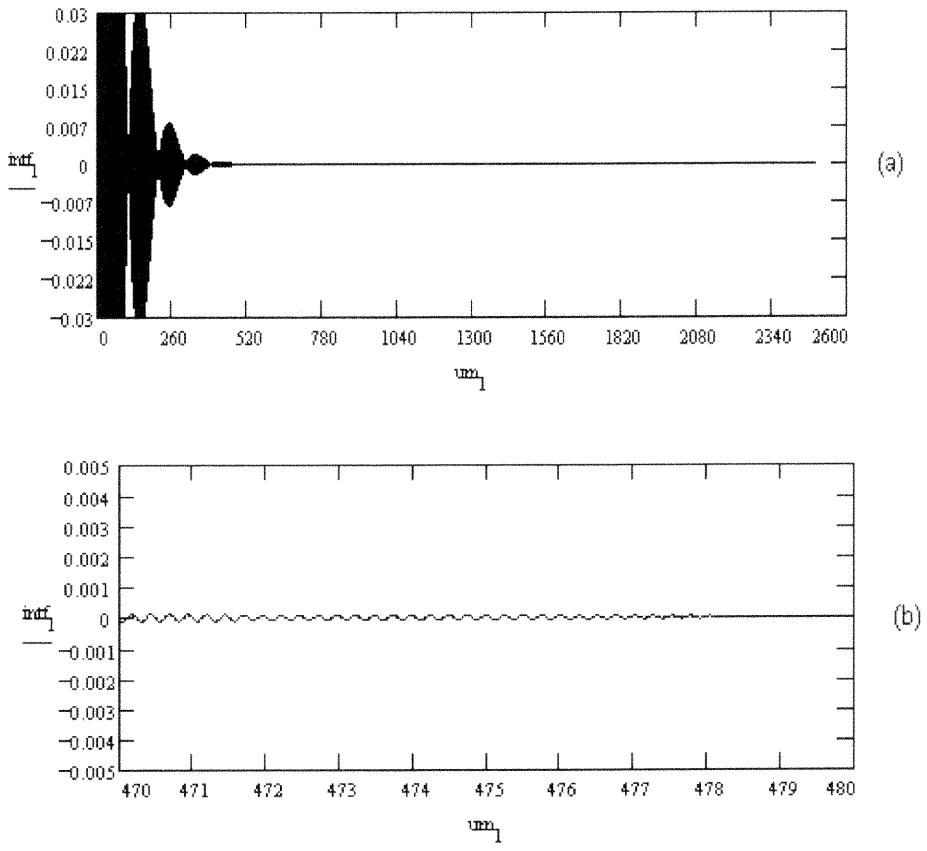

Figure 4.3 Simulated interferogram from broad source ($100cm^{-1}$ bandwidth at 253.7nm corresponding to bandwidth of 1nm) where $intf_l$ is the interferogram intensity in an arbitrary unit and um_l is the mirror displacement in the unit of micron. (a) interferogram in the range of 2μm. (b) expanded interferogram.

In the application of resonance fluorescence detection, an interferogram will be generated by linear displacement of the movable mirror of the Michelson interferometer. Light entering the Michelson would include both the excitation light and fluorescence. Hence, this moving fringe pattern contains information on both the excitation light source and fluorescence emission. Figure 4.4 shows the simulated interferogram for resonance fluorescence detection. When the light source is broad band, the intensity of its modulation upon mirror translation (i.e. its interferogram) quickly dies out as in Figure 4.3. On the

other hand, the modulation of the very narrow mercury resonance transition is presented as a much longer oscillation in the interferogram as in Figure 4.3. This offers the possibility of high sensitivity in discriminating the resonance fluorescence signal from the elastic background. Furthermore, the amplitude of the long oscillation is linearly proportional to the concentration of elemental mercury [52]. It is expected that this approach will achieve high background rejection with high optical throughput for good signal-to-noise [53, 54].

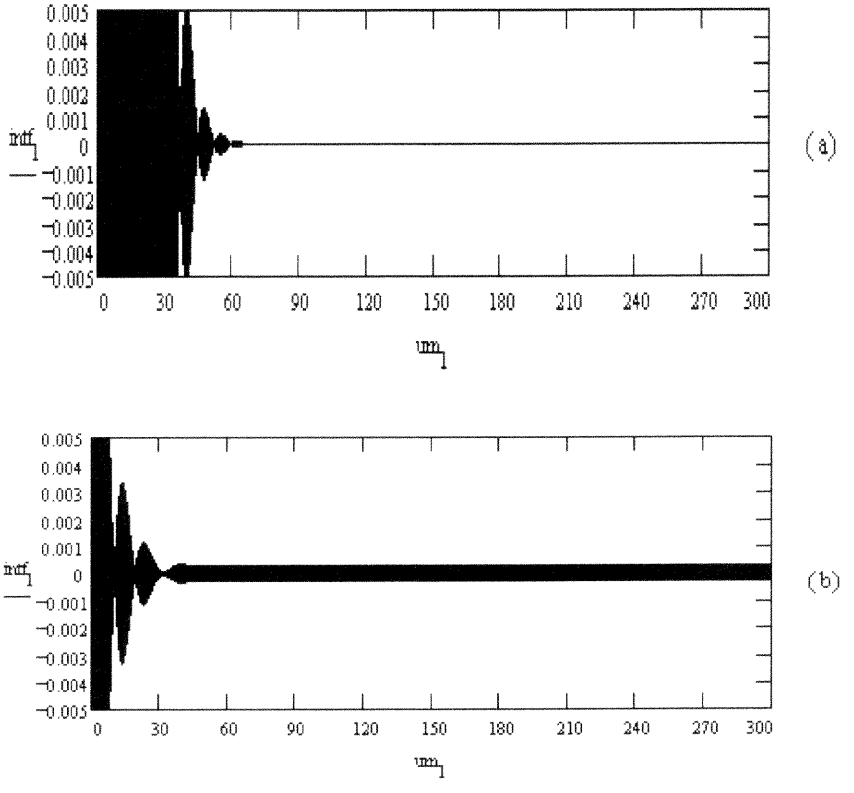

Figure 4.4 (a) Simulated interferogram from broad source (1000cm^{-1} bandwidth) (b) Simulated interferogram from narrow mercury (0.1cm^{-1} bandwidth) emission and broad source (1000cm^{-1} bandwidth) assuming that the intensity of background scattering is 1% of incident light power and mercury absorption is 10% (calculation see Appendix C) .

4.3 Experimental Apparatus

A schematic diagram of the UV interferometer is shown in Figure 4.5. The light source is a low pressure mercury pen lamp illuminating an aperture of 1.5 mm diameter. With a spectral linewidth of 0.002 nm at 253.7 nm, this lamp has relatively strong atomic mercury UV emissions. Another aperture (6 mm) was installed to confine the beam size within the diameter of the collimating lens. Light emerging from the second aperture is collimated by a quartz lens (f =15 cm) to a diameter of 7 mm. This collimating lens is mounted upon an X-Y-Z translation stage. The collimated beam then passes into the Michelson interferometer.

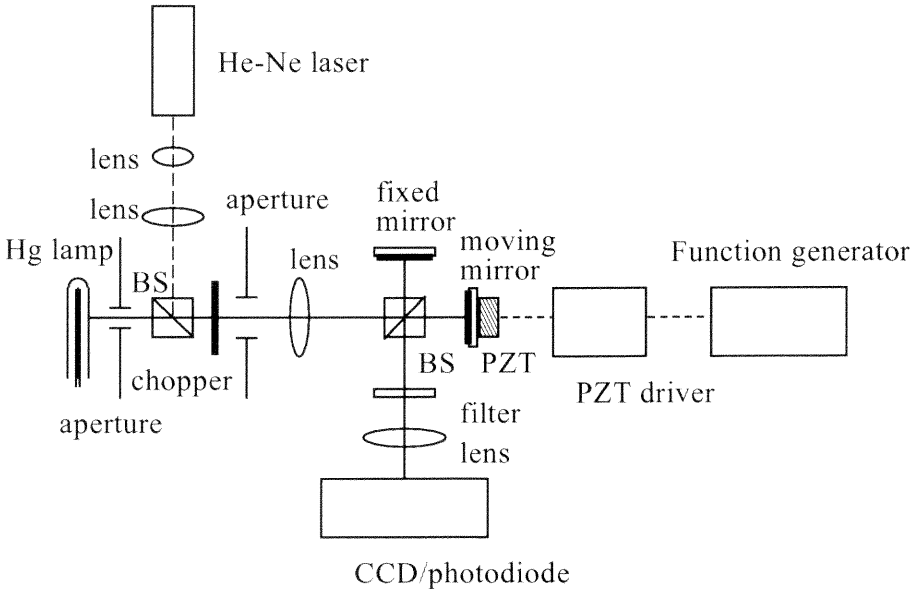

Figure 4.5. Schematic diagram of experiment setup (BS: Beamsplitter, PZT: piezoelectric actuator, IF: interference filter)

An unpolarized quartz beamsplitter cube (ESCO) rather than a beamsplitter plate is used for dividing the beam. Therefore, no compensator plate is needed in the transmitted

path. This makes the system more compact and easier to align. The beamsplitter cube has a surface accuracy of $\lambda/10$, reflected/transmitted ratio of 30/30 in the UV, and is mounted upon a precision table.

The fixed and moving plane mirrors are both flat to $\lambda/10$. The moving mirror assembly is mounted on a translation stage loaded with a piezoelectric actuator (Thorlab). This actuator is capable of precise nanometer positioning. It permits a linear voltage-displacement response to modulate the path length of the moving mirror. The basic actuator drive signal is a triangular waveform created by a function generator. At the exit of the interferometer, an interference filter (bandwidth 10 nm) isolates the desired Hg emission wavelength. Two filters are applied: 253.7 nm for UV work and 546.1 nm for visible interferometry. A quartz focusing lens (f = 8 cm) is placed after the filter in order to increase the fringe contrast which is particularly needed in the UV region.

In this setup, an optical detector is placed at a distance of 13 cm from the focusing lens. Two types of detector are used to record output information from the interferometer. An unenhanced, UV sensitive Charge Coupled Device (CCD) camera (Santa Barbara Instruments, Model ST-6) is used to capture stationary green and UV fringes without activating the actuator (i.e. the translating mirror is fixed in one position) and without the chopper. The CCD camera is operated through a interface program (Kestrelspec) in a laboratory computer. A UV sensitive photodiode (Thorlab DET 210), interfaced to a lock-in amplifier with the light beam chopped at 500 Hz, is employed to record the interferogram of moving fringes generated by scanning the movable mirror. A laboratory personal computer is interfaced to the lock-in, and displays the interferogram through a Labview data acquisition/display program.

The alignment of the interferometer is accomplished by temporarily introducing the optical beam from a helium-neon (He-Ne) laser (632.8 nm) along the direction perpendicular to the mercury lamp beam (dotted lines). The beam from the He-Ne laser is turned to be collinear with the light beam from the mercury lamp by putting a temporary beamsplitter cube before the chopper (see Figure 4.5). In order to reduce the vibration noise, the interferometer is placed on a floated optical bench.

4.4 Performances of the UV Interferometer

Figure 4.6 shows the fringe patterns from the Hg pen lamp obtained by the CCD camera, which was operated with a 0.1 second exposure time, one exposure accumulation, and a pixel resolution of 11.5μm (horizontal) × 216 μm (vertical). Figure 3.5(a) gives the fringe pattern with the interference filter centered at 546 nm, while Figure 3.5(b) gives fringes at 253.7 nm. Both patterns actually show vertical fringes. While aligning the interferometer with the He-Ne laser, symmetric circular fringes after expanding the laser beam before entering the interferometer has been obtained. In the Michelson interferometer, the two beams passing through the two arms of the interferometer must interfere with each other with a fixed phase relation throughout the beam cross section to obtain circular fringes. This is relatively easy for spatially coherent light such as a laser beam. But if the incident light is a spatially incoherent lamp (e.g. pen lamp), it becomes quite difficult especially in the short wavelength UV region. This difficulty in alignment is considered to be the main reason why interferometry in the visible and UV wavelength regions is not commonly used. In this interferometer setup, although the two mirrors are aligned to be perpendicular to each other with the He-Ne laser, they are slightly non-perpendicular

relative to the light beam from the Hg pen lamp. Therefore, vertical fringes instead of circular fringes occurred.

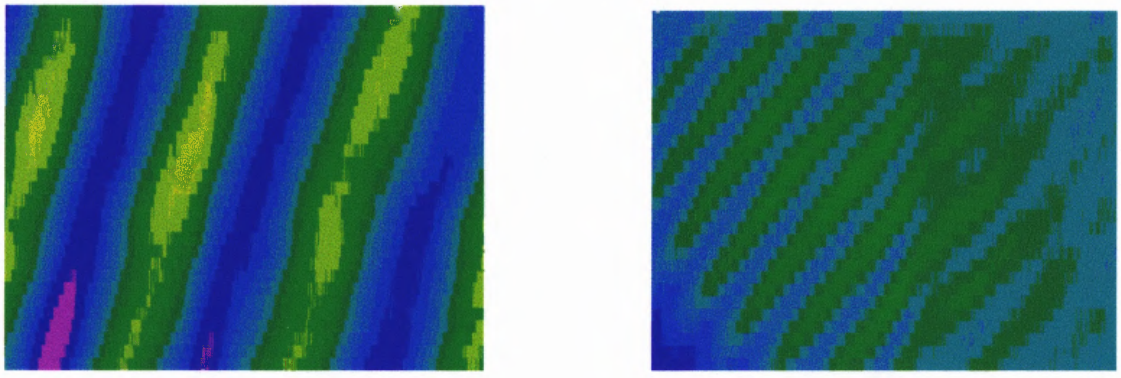

(a) (b)

Figure 4.6 CCD pictured stationary interference fringes at wavelength of 546.1nm (a) and 253.7 nm (b)

Without placing a lens at the exit of the interferometer, only the green fringes is observed using the CCD camera. The fringes at 253.7 nm have a poorer contrast than the visible fringes due to the shorter wavelength. In this experiment, about 3 fringes at 546 nm and 7 fringes at 253.7 nm in the optical active area of 9 mm × 7 mm of this CCD camera are observed. This observation is consistent with the fact that vertical fringes spacing should be proportional to the wavelength [55].

To characterize the performance of this interferometer, one point of the interferograms with the photodiode both at 546.1 nm and 253.7 nm were recorded. The interferogram is obtained by scanning one mirror of the Michelson interferometer with respect to the fixed mirror over a certain distance. In the experiment, the path length of one arm of the interferometer is modulated by the piezoelectric actuator. The actuator

driver is controlled by a function generator which outputs a 5 mHz triangle wave with a peak to peak amplitude of 4 volt, and an offset of 2 volt. The actuator driver outputs a triangle wave at the same frequency, but a peak amplitude of 120v. Under these conditions, the actuator can permit a displacement of as much as 15 μm. The spectral resolution R of the interferometer is given by [56]:

$$R = \frac{1}{2L} \tag{4.2}$$

where L is the maximum displacement of the moving mirror.

Then, the spectral resolution of this interferometer is 2.1nm at 253.7nm.

Prior to the investigation of the interferogram of the atomic mercury emissions, the dependence of the movable mirror displacement as a function of the voltages applied to the piezoelectric actuator had to be obtained first. The displacement of the piezoelectric actuator with voltage is calibrated using the interferogram obtained with the He-Ne laser, where symmetric circular fringes are observed. Figure 4.7 illustrates the interferogram with the He-Ne laser (632.8 nm) as the light source where the computer collects one data point per 0.4 second.

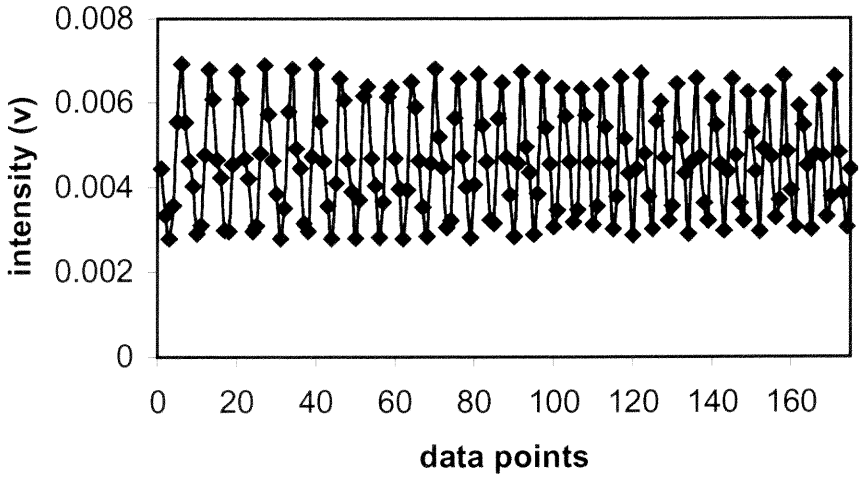

Figure 4.7 Interferogram of He-Ne laser where computer collects a data point every 0.4 second.

From the cyclic intensity distribution at the detector as a result of sweep fringes, the light wavelength λ can be retrieved from the equation [55]:

$$d = \frac{m\lambda}{2} \tag{4.3}$$

where d is the mirror displacement and m is the number of fringes that shifted. As in Figure 4.7, there are 32 fringes shifted over 68s corresponding to voltage of 81.6v to the actuator. Hence, the calibrated displacement that the actuator can provide under a voltage of 120v is:

$$\frac{0.6328 \times 32 \times 120}{81.6 \times 2} = 14.88 \ \mu m \tag{4.4}$$

Figures 4.8 shows the photodiode detected fringe intensity variation (interferogram) as a function of mirror displacement at 253.7 nm and 546.1 nm respectively. For the interferogram at 546.1 nm, the computer collected one data point per 0.4 second. But for 253.7 nm, the data acquisition rate was set at a shorter time constant,

one point per 0.1 second, in order to recover a complete modulation profile. The axis of Figure 4.8 has been calibrated by applying the translation function of the movable mirror, that is 14.88 μm displacement of the piezoelectric actuator at 120v. Applying equation 4.3, interferograms in Figure 4.8 indicate that the measured atomic emissions from the mercury pen lamp are centered at 257.9 nm and 543.6 nm, respectively. Compared with the literature atomic mercury emission spectrum, the wavelength measurement from this interferometer is accurate to within an acceptable 1.6%.

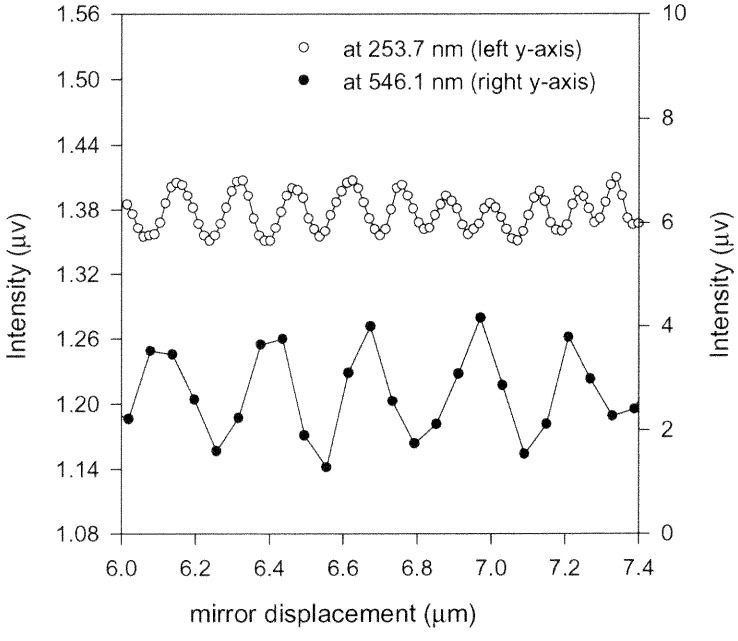

Figure 4.8 Part of photodiode detected interferograms with 546.1 nm interference filter and with 253.7 nm interference filter.

Regarding the modulation efficiency, defined as the ratio of modulation amplitude peak intensity to the center intensity, approximately 3 % at 257.9 nm and 28 % at 543.6 nm were obtained. The lower modulation efficiency for the UV results from the poorer

contrast of the UV fringes with this interferometer than that of the green fringes. It is reasonable, since the shorter wavelength requires a more demanding precision of the optomechanical components. Additionally, the fluctuation of lamp power and actuator driving may contribute to the jitter of the modulation amplitude as observed in Figure 4.8.

4.5 Limitations of UV Interferometry

The above results regarding the proved interferogram modulation from narrow mercury emissions have demonstrated the potential feasibility of UV interferometry for detection of Hg resonance fluorescence. With some further improvements in this UV interferometer system, such as a reduction of entrance aperture and better alignment of the two mirrors, its performance can be improved.

For application to resonance fluorescence detection in a supersonic jet, Figure 4.9 shows a hypothetical set-up. A narrow light source (such as a laser) is not good for detection of resonance fluorescence by UV interferometry, since its interferogram is a cosine function that does not decay as a broad source does. Therefore, a high intensity Xenon arc lamp, which provides intense broadband ultraviolet radiation, is preferred to be used for UV interferometry here.

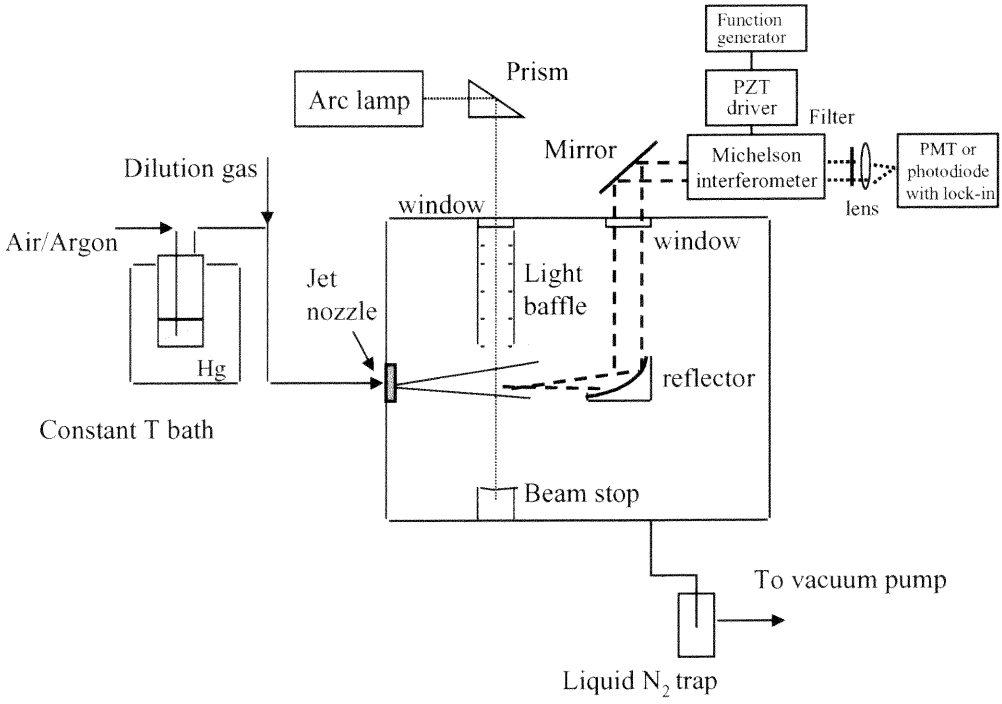

Figure 4.9 Interferometric measurement of resonance fluorescence in vacuum system

However, since the spectral range is in the UV, the required near-perfect alignment of the Michelson interferometer is a very difficult and time-consuming job. At shorter wavelengths, particular UV, vibration sometimes can severely degrade the performance of the interferometer. Furthermore, lamp as a broadband light source may not offer strong power to excite atomic fluorescence.

The following is the calculation of optical throughput of the interferometer with an available Oriel Model 6259 Xe arc lamp (500W). The irradiance of this arc lamp with collimating lens at 253.7 nm is 1.26mW nm^{-1} [31]. As 1 cm^{-1} is equivalent to $\Delta\lambda$ of 0.0065nm at 253.7 nm, the total irradiance of the lamp in $1cm^{-1}$ (the laser linewidth) range is

$$1.26\ mW\ nm^{-1} \times 0.0065\ nm = 0.008\ mW \tag{4.5}$$

Including the rear reflector in the arc lamp, the actual optical power from the lamp is:

$$1.5 \times 0.008 = 0.012\ mW \tag{4.6}$$

This power as it transmits through the interferometer can be followed in the order: 30% transmission of the UV beamsplitter at 253.7 nm; beam size reduced from a diameter of 3cm to 7mm by the aperture; 90% mirror reflection efficiency; 50% interferometer transmission of the incoming optical energy; and 80% mirror alignment efficiency (assumed). Thus, the total optical throughput for the interferometer with the arc lamp light source is estimated to be:

$$0.012 \times 0.3 \times (\frac{0.7}{3})^2 \times 0.9^2 \times 0.5 \times 0.8 = 0.06 \mu W \tag{4.7}$$

On the other hand, the beam power available from the laser system at 253.7nm with $1 cm^{-1}$ linewidth is about 1.5mW.

Hence,

$$\frac{\text{int}\,erferometry\ \ throughput}{laser\ \ throughput} = \frac{0.06\ \ \mu W}{1.5\ \ mW} = 6.3 \times 10^{-4} \tag{4.8}$$

The above calculation shows that the optical throughput of the interferometer with an arc lamp source to detect resonance fluorescence is at least four orders of magnitude less than that of a UV laser using time-gating approach. As fluorescence intensity is linearly proportional to the excitation power, the time-gating approach with laser system is more sensitive for investigation of Hg resonance fluorescence detection in a supersonic jet.

CHAPTER 5

CONCLUSIONS

5.1 Summary of Research Results

This dissertation presents a systematic study of potential methods for real-time trace detection of vapor phase elemental mercury and volatile mercury compounds in industrial stack gases. The following are the results through experimental data analysis:

(1) Laser induced photofragment fluorescence (PFF) spectroscopy is used to investigate mercury compound vapor. In the experiment, low concentrations (6 ppb to 30 ppm) of mercuric bromide ($HgBr_2$) vapor in argon are introduced to an atmospheric pressure flow cell. The PFF technique uses 222nm laser radiation to photolyze $HgBr_2$ and excite fluorescence from the resulting Hg atoms at 253.7nm. The fluorescence intensity is linear with laser fluence over the range of 45 mJ/cm^2 to 180 mJ/cm^2. An extrapolated detection limit by photomultiplier tube (PMT) plus interference filters below 1 ppb of $HgBr_2$ in the absence of air is estimated at a measurement duty cycle of 3 seconds. A linear dynamic detection range up to 0.7 ppm (11 mg/m^3) is achieved with PMT detection.

Another detection system, Charge Coupled Device (CCD) camera + monochromator combined with PFF spectroscopy for measurement of $HgBr_2$ vapor has been investigated as well. The CCD response remains linear up to 20 ppm. Observed nonlinearity of the PFF signal at higher concentrations is calculated due to mercury self-absorption. The unenhanced CCD detection limit is about 30 ppb $HgBr_2$ in the absence of air. With the same collection optics and under the same experimental conditions, the

detection limit for the PMT system is estimated to be 5 ppb with reduced boxcar averaging, but the linear dynamic range ends at 0.7 ppm. The CCD detection system offers reasonable sensitivity plus spectral information, thus enhancing PFF as a technique for the environmental monitoring of airborne mercury compounds. It is expected that the CCD detection system would be more versatile for measuring metal compound species by PFF spectroscopy in any future real-time airborne metals monitor.

(2) A compact, inexpensive ultraviolet interferometer system capable of Fourier Transform spectrochemical measurements has been studied in this doctoral research work. The interferometer is set up in a Michelson configuration. The light source in our study is a low pressure mercury pen lamp which provides strong atomic mercury emissions at 253.7nm. Fringe patterns at 253.7nm and 546.1nm are imaged by a charge-coupled-device (CCD) camera. Moving fringes are generated by precision linear displacement of the movable mirror of the Michelson interferometer. The interferograms at both ultraviolet and visible regions of the atomic mercury emission spectrum are recorded. Based on the translation function of the movable mirror, wavelength information is retrieved from the interferogram. The accuracy of the experimentally resolved wavelength at 253.7 nm is within 1.6%. The observed modulation efficiency of the moving UV fringes in the set-up is approximately 3%. The interferometer developed has potential for application in atomic emission detection in the ultraviolet, particularly

considering there is no practical, low cost commercial laser for operation at 253.7nm to date.

(3) Laser induced resonance fluorescence spectroscopy is used to detect atomic mercury vapor. To reduce fluorescence quenching, an argon gas stream containing Hg vapor is

expanded through a nozzle into a vacuum. A supersonic jet is produced over a certain axial distance. This jet is crossed with a pulsed laser beam at 253.7nm to excite atomic resonance fluorescence, which is distinguished from the elastic scattering background by time gating. Time dependent resonance fluorescence at different nozzle-to excitation distances is investigated. The time evolution of observed Hg resonance fluorescence together with background scattering are convoluted with the time response of the detector PMT. After accounting for this lag, when nozzle-to-excitation distance varies from 2mm to 20mm, a fluorescence lifetime of 77ns to 112ns is observed with a measurement accuracy of 7%. In the jet downstream region of 5mm to 20mm, the gas density is found decreasing slightly, as gas density is so low that there are no further cooling.. The Hg resonance fluorescence measured here is linear with laser beam power. A detection limit (S/N=2) of 3 ppb mercury is estimated with unfocused laser beam excitation at a jet downstream distance of 12 mm and with 3 second data integration time. The Hg resonance fluorescence in a supersonic jet is observed to remain linear with Hg concentration over the testing concentration region (up to 1.5ppm).

Total mercury, including elemental and compound, emitted from industrial incinerators ranges from 10 to 2000 $\mu g/m^3$[3], corresponding to 1 to 180 ppb. This work indicates that resonance fluorescence spectroscopy in a supersonic jet has sufficient sensitivity with linear response to measure volatile mercury vapor in most real industry stack gases. Thus, it is a promising near real-time method for continuous mercury emission monitoring. On the other hand, the measurement investigated here uses Ar as carrier gas. The quenching gas generally considered in industrial stack gas is O_2 which has stronger quenching effect to Hg than inert gas Ar. It is expected that fluorescence in

O_2 combined with supersonic jet spectroscopy will perform better compared to atmospheric measurement.

5.2 Suggestions

As for any monitoring technology, detection limit is one of the critical quality factors. To have a competitive mercury emission monitor, it is desirable that the detection limit of the instrument be in the parts per trillion level. To improve the detection limit of the PFF technique for mercury compound detection, a shorter wavelength excimer laser is a good option. The absorption cross-section of $HgBr_2$ at 193nm is three times greater than that at 222 nm. Also, the relatively high laser energy, which can be 50 times greater than the present laser system, makes the excimer quite attractive for this application.

To further improve the detection limit of the PFF technique, it can be investigated in combination with the supersonic jet as well. First, fluorescence quenching will be reduced due to reduced carrier gas density. Second, the cooling in the supersonic expansion simplifies the spectrum by putting almost all the molecules into their lowest vibrational state and lowest few rotational states, while the collisionless environment of the molecular beam removes spectral broadening. These two factors will sharpen and enhance the fluorescence spectra, leading to a better discrimination of fragment vibrational structure and better speciation of parent molecules.

For resonance fluorescence spectroscopy combined with the supersonic jet as being investigated here, it is expected that reducing the background can improve the detection limit of this technique. In the Hg detection experiment, strong physical scattering occurs. With some improvement in the light baffling and system design, background signal may

be reduced to Rayleigh scattering, which is linear with gas density. Then in the process of supersonic expansion, Rayleigh scattering drops while resonance fluorescence increases. This will yield an estimated detection limit of 10ppt [10].

In the current supersonic jet experiment, the manufactured nozzle diameter is 200 μm. This was chosen for the maintenance of one atmosphere back (supply) pressure at the nozzle inlet while keeping the source (Hg) flow in the desired saturation range. As discussed in Chapter 3, the drop of carrier gas density in the jet is a function of Mach number, which wholly depends on dimensionless axial distance x/D in the isentropic expansion region. Calculations in section 3.1.3 show that measurement combined with supersonic jet potentially has the ability to improve detection sensitivity; and for carrier gas of argon it is optimized when Mach number equals to 2, where gas density does not drop too much. For small nozzle diameter D, it means laser excitation must be very close to the nozzle exit. This introduces strong background and thus makes the optimal detection experimentally not possible. But, with larger nozzle diameters, say between 500 μm and 700 μm, laser excitation can be set closer to the nozzle. Under this condition, where gas density does not drop too much and background is not so strong, calculated optimal fluorescence detection might be practical. Increasing the nozzle diameter is an option to improvement of resonance fluorescence detection in a supersonic jet with investigating.

The excitation light source used here for real-time detection of elemental and compound mercury is a complex and expensive pulsed laser systems. In a commercial device, the excitation source should be low cost, compact, and convenient to operate, such as an excimer lamp. It is a highly efficient cold light source and emits nearly

monochromatic radiation in the UV spectrum. The available wavelengths on the market today are 126nm, 146nm, 172nm, 222nm and 308nm. Lamps with irradiance of 25mW/cm^2 (beam diameter of 30mm) with 2 nm bandwidth at 222nm are available from USHIO America, Incorporated. This lamp is a good option of light source for commercial application of PFF technique.

To date, no one has engineered a practical, low cost commercial laser for operation at 253.7nm. The strong narrow, coherent radiation at 253.7nm currently is obtained by frequency doubling of the output from either excimer laser pumped dye laser or Nd:YAG laser pumped dye laser. Though it offers strong excitation power at 253.7nm which is particular important to fluorescence detection, its high cost and bulkiness are problem for commercial detection applications. Another alternative to a pulsed laser system is interferometry using a broadband Hg arc lamp as the light source for real-time elemental mercury detection. High pressure mercury arc lamps have been used for remote Hg sensing by Differential Optical Absorption Spectroscopy method [57, 58]

In addition, the existing of strong background in Hg resonance fluorescence detection restricts the degree of improvement in detection limit that the jet cooling approach can achieve. Thus, a non-resonant laser induced fluorescence spectroscopy combined with supersonic jet expansion may be investigated as a candidate for real-time mercury species detection. In this case, excitation may be chosen at 253.7nm and fluorescence may be monitored at the weaker 435.8nm or 546.1nm emission lines of mercury.

APPENDIX A

MathCAD Calculates Interferogram of Light Source with $1cm^{-1}$ Bandwidth

$i := 0..262144$

$$f_i := \exp\left[-\left(\frac{|39432 - i|}{0.5}\right)^2\right]$$

$ip := 38000..42000$

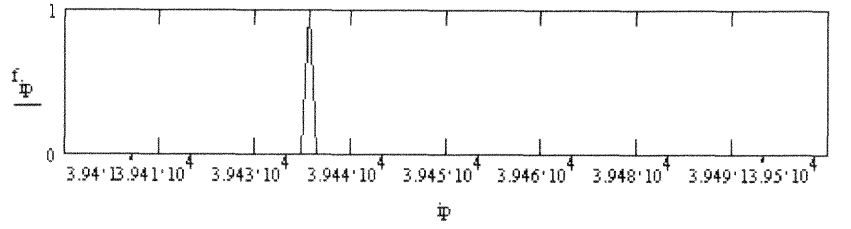

$l := 0..$

$$um_l := 1 \cdot \frac{10000}{262144} \cdot 0.5$$

$intf := ifft(f)$

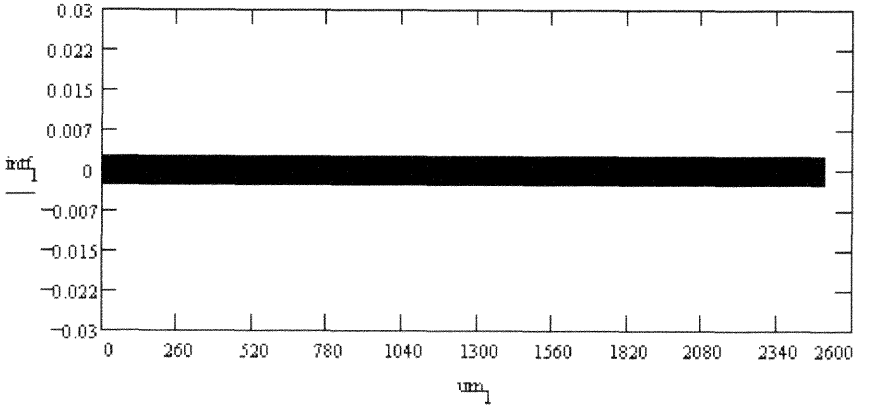

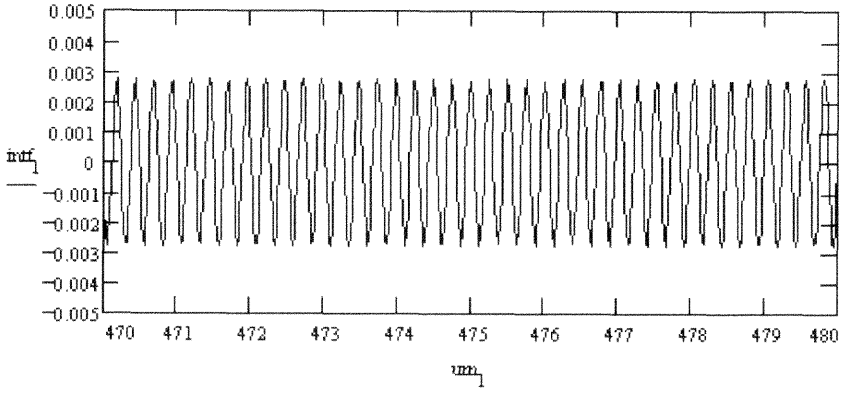

APPENDIX B

MathCAD Calculates Interferogram of Light Source with 100cm^{-1} Bandwidth

$i := 0 .. 262144$

$ip := 38000 .. 42000$

$$f_i := \exp\left[- \left(\frac{|39432 - i|}{50} \right)^5 \right]$$

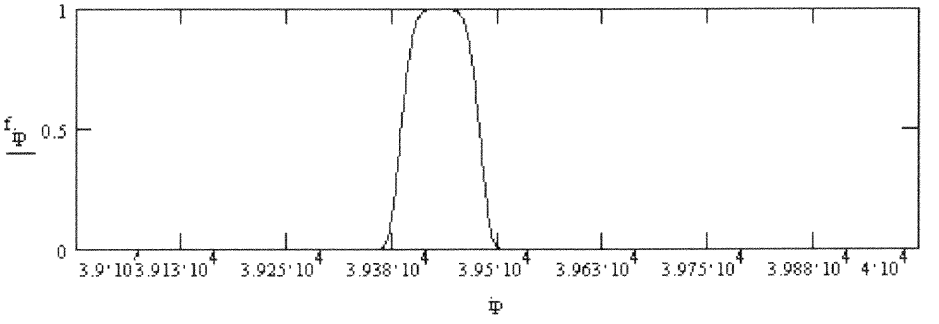

$l := 0 .. 131072$

$$um_l := 1 \cdot \frac{10000}{262144} \cdot 0.5$$

$intf := ifft(f)$

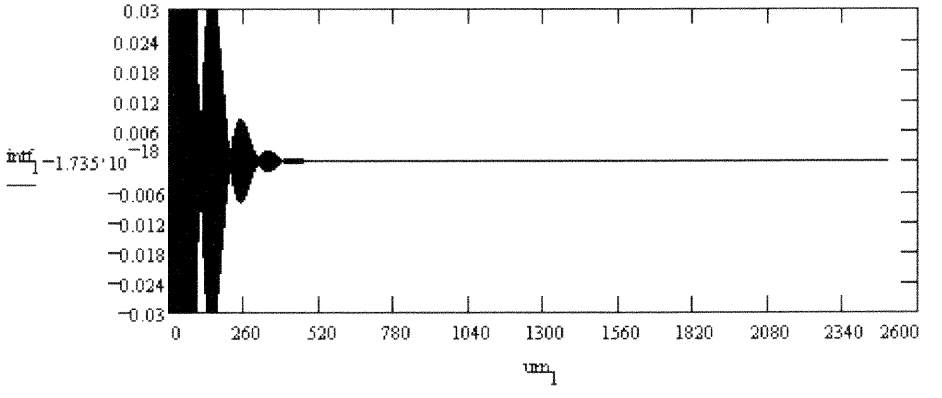

APPENDIX C

MathCAD Calculates Interferogram from Broad Background (bandwidth of 1000 cm^{-1}) and Narrow Atomic Emission (bandwidth of 0.1cm^{-1})

$i := 0..262144$

$$f_i := \exp\left[-\left(\frac{|39432 - i|}{538}\right)^5\right]$$

$ip := 38000..42000$

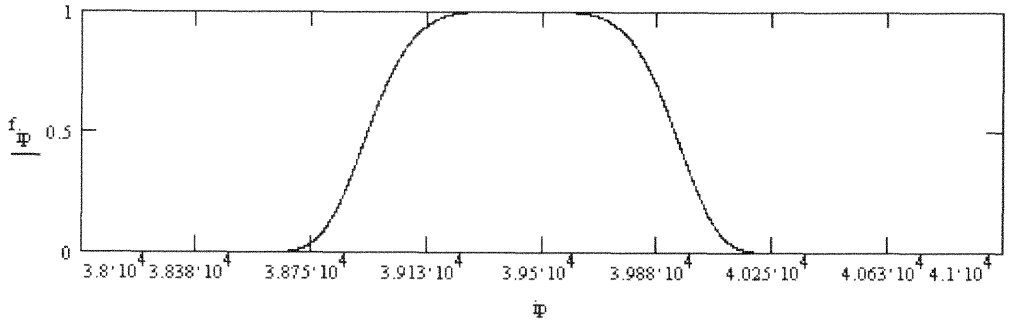

$l := 0..131072$

$$um_l := 1 \cdot \frac{10000}{262144} \cdot 0.5$$

$$f_i := f_i \left[0.01 + 0.1 \cdot \exp\left[-\left(\left|\frac{39432 - i}{0.05}\right|\right)^5\right]\right]$$

$intf := ifft(f)$

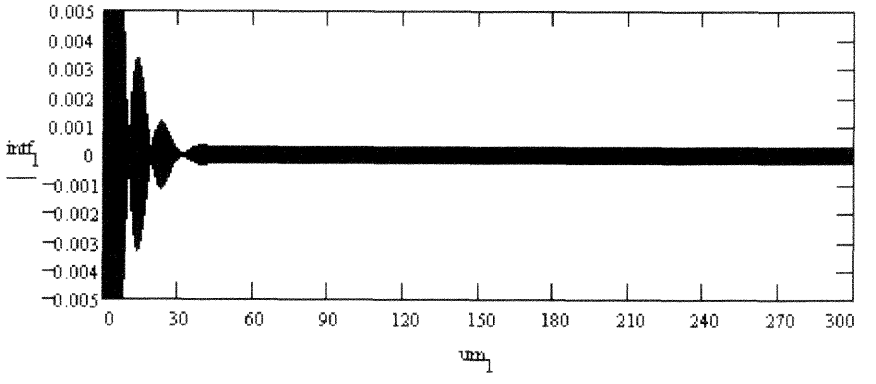

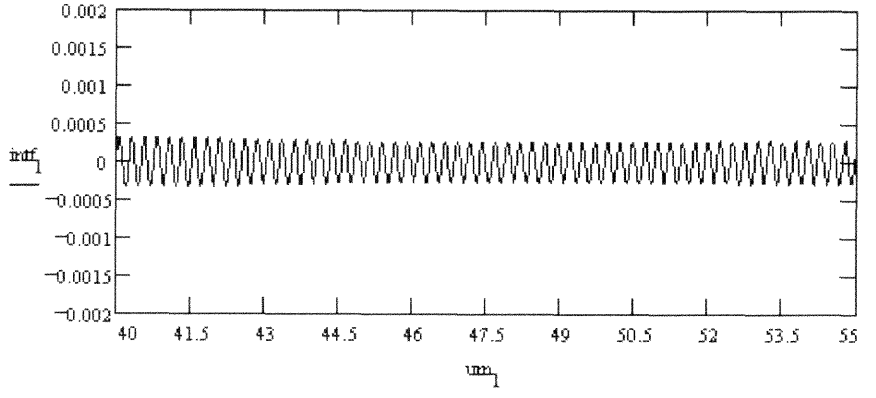

REFERENCES

1. B. Hall, P. Schager, and O. Lindquist. "Chemical reactions of mercury in combustion flue gases", *Water, Air and Soil Pollution,* **56**, 3, 1991

2. M. Stoppler, *Hazardous Metals in the Environment*, Elserier Science Publishers, 1992

3. R. Meij, "The fate of mercury in coal-fired power plants and the influence of wet flue-gas desulphurization", *Water, Air and Soil Pollution*, **56,** 21, 1991

4. W. R. Hatch and W. L. Ott, "Determination of sub-microgram quantities of mercury by atomic absorption spectrophotometry", *Anal. Chem.* **40**, 2085,1968

5. M. Horvat and V. Lupsion, "Determination of total mercury in coal fly ash by gold amalgamation cold vapor atomic absorption spectrometry", *Anal. Chim. Acta* **243**, 71, 1991

6. D. C. Baxter and W. Frech, "Determination of mercury by atomic absorption spectrometry using a platinum-lined graphite furnace for in situ preconcentration", *Anal. Chim, Acta* **225**, 175, 1989

7. R. L. Lancione and D. M. Drew, "Evaluation of ICP atomic fluorescence for the determination of mercury", *Spectrochim. Acta*, **40B**, 107, 1985

8. Tekran, Inc.,1-132 Railside Road, Toronto, Canada 1998

9. H. Edner, G. W. Faris, A. Sunesson and S. Svanberg, "Atmospheric atomic mercury monitoring using absorption lidar techniques", *Appl. Opt.* **28**, 921, 1989

10. R. Barat, A. Poulos, "Real time trace detection of elemental and compounded mercury", *Project proposal to EPA*, 1997

11. A. Eckbreth, *Laser Diagnostics for Combustion Temperature and Species*, 2nd edition, Cordon and Breach Publishers,1996

12. D. L. Andrews, ed., *Applied Laser Spectroscopy: techniques, instrumentation and applications,* New York:VCH, 1992

13. R. Barat, A. Poulos, "Detection of mercury compounds in the gas phase by laser photo-fragmentation/emission spectroscopy", *Applied Spectroscopy*, **52**, 1360, 1998.

14. C. Whitehurst and T. A. King. "Emission spectroscopy of mixed photo-dissociated mercury halides", *J.Phys. D: Appl. Phys.* **20**, 1577, 1987

15. J. B. Simeonsson, R. C. Sausa, "A critical review of laser photofragmentation/ fragment detection techniques for gas-phase chemical analysis", *Applied Spectroscopy Reviews*, **31**, 1, 1996

16. R. C. Oldenborg, S. L. Bauhcum, "Photofragment fluorescence as an analytical technique: application to gas phase alkali chlorides", *Anal. Chem.* **58**, 1430, 1986

17. B. L. Chadwick, P. G. Griffin, R. J. S. Morrison, "Multiwavelength monitoring of photofragment fluorescence after 193nm photolysis of NaCl and NaOH: application to measuring the sodium species released from coal at high temperature", *Appl. Spec.* **51**, 990, 1997

18. M. O. Rodgers, K. Asai and D. D. Davis, "Photofragmentation-laser induced fluorescence a new method for detecting atmospheric trace gases", *Appl. Opt.* **19**, 3597, 1980

19. A. J. Alfano, D. J. Benard, "Photolysis- laser induced fluorescence diagnostic for GaCl", *Appl. Opt.* **32**, 5373, 1993

20. J. Schendel, R. Hohmann, E. L. Wehry, "Laser photolytic fragmentation-fluorescence spectrometric determination of Nitromethane", *Appl. Spec.* **41**, 640, 1987

21. A. T. Poulos, "A photofragment fluorescence spectrometric method for measurement and speciation of mercury emission", *SBIR-DOE phase I final report*, 1994

22. H. Maya, "Ultraviolet absorption cross sections of HgI_2, $HgBr_2$,and tin(II) halide vapors", *The Journal of Chemical Physics*, **67**, 4976, 1977

23. C. Vandecasteele and C. B, Block, *Modern Methods for Trace Element Determination*, John Wiley & Sons, 1993

24. H. J. Emeleus and A. G. Sharpe, *Advances in Inorganic Chemistry and Radiochemistry*, Academic press, New York, 1968

25. CCD camera operating manual, Santa Barbara Instrument Group, 1996

26. CRC handbook of Chemistry and Physics, 62nd Ed.; R. C. Weast, Ed.; Boca Baton, Florida, D-190, 1981

27. J. G. Calvent, J. N. Pitts, *Photochemistry*, Wiley; New York, 74,1966

28. H. Inaba, *Laser Monitoring of the Atmosphere, Topics in Applied Physics*, Vol. 14, E.D. Hinkley, Ed.; Springer-Verlag, New York, 1976

29. H. Neij and M. Alden, "Application of two-photon laser-induced fluorescence for visualization of water vapor in combustion environments", *Appl. Opt.* **33**, 6514, 1994

30. D. Riley, L. Doyle and R. Al-Wazzan, "Trapping of radiation in a laser ablated $Yba_2Cu_3O_7$ plume", *J. Appl. Phys.* **79**, 7223, 1996

31. Oriel Instrument manual

32. A. H. Shapiro, ed., *The Dynamics and Thermodynamics of Compressible Fluid Flow*, New York: Ronald press, 1958

33. D. M. Lubman, *Lasers and Mass Spectrometry*, New York: Oxford Univ. Press, 1990

34. G. Scoles, ed., *Atomic and Molecular Beam Methods,* Oxford Univ. Press,1988

35. E. Becker, *Gas Dynamics*, Academic Press, New York, 1968

36. G. M. McCelland, "Vibrational and rotational relaxation of iodine in seeded supersonic beams", *The Journal of Physical Chemistry*, **83**, No.8, 947, 1979

37. J. B. Anderson and J. B. Fenn, "Velocity distribution in molecular beams for nozzle sources", *Phys. Fluid*, **8**, 780, 1965

38. P. W. Milonni and J. H. Eberly, *Lasers*, New York: Wiley, 1988

39. J. Sansonetti, M. L. Salit, and J. Reader, "Wavelength of spectral lines in mercury pencil lamps", *Applied Optics*, **35**, 74, 1996

40. P. S. Steven, J. H. Mather and W. H. Brune, "Measurement of tropospheric OH and HO_2 by laser-induced fluorescence at low pressure", *Journal of Geophysical Research*, **99**, 3543, 1994.

41. J. N. Dodd, W. J. Sandle and O. M. Williams, "A study of the transients in resonance fluorescence following a step or a pulse of magnetic field", *J. Phys.B:Atomic and Molecular Physics*, **35**, 74, 1996.

42. J. H. Moore, *Building Scientific Apparatus: a practical guide to design and construction*, California: Addison-Wesley, 1989

43. H. E. Gunning, S. Penzes, H. S. Sanhu and O. P. Strausz, "The interaction of mercury $6(^3P_1)$ atoms with noble gas atoms", *Journal of the American Chemical Society*, **91**:27, 7684, 1969

44. D. H. Levy, "Laser spectroscopy of cold gas-phase molecules", *Annual Review of Physical Chemistry*, 31, 2705, 1980

45. P. P. Wegerner, ed., *Molecular Beams and Low Density Gas Dynamics*, New York: M. Dekker, 1974

46. R. Campargue, "Progress in overexpanded supersonic jets and skimmed molecular beams in free-jet zones of silence", *J. Phys. Chem.*, **88**, 4466, 1984

47. R. E. Smalley, L. Wharton and D. H. Levy, "The fluorescence excitation spectrum of rotationally cooled NO_2", *The Journal of Chemical Physics*, **63**,4977,1975

48. H. H. Bauer, *Instrumental Analysis*, Allyn and Bacon Press, Boston, 1978

49. Manual of PMT, ThorEMI.

50. McPherson monochromator manual

51. P. R. Griffiths and J. A. Dehaseth, *Fourier Transform Infrared Spectrometry*, John Wiley & Sons, 1986

52. A. Poulos and R. Barat, "Sensitive remote detection of elemental mercury and mercury compound vapor by interferometric absorption spectroscopy", *Research Proposal to Hazardous Substance Management Research Center*, 1999

53. E. A. Stubley and G. Horlick, "A fourier transform spectrometer for UV and visible measurements of atomic emission sources", *Applied Spectroscopy*, **39**, 800,1985

54. R. Williams, "Application of fourier transform spectroscopy in the ultraviolet, visible, and near-IR", *Applied Spectroscopy Reviews*, **25**, 63,1989

55. E. Hecht and A. Zajac, *Optics*, Addison-Wesley, NewYork, 1974

56. R. J. Bell, *Introductory Fourier Transform Spectroscopy*, Academic Press, 1972

57. H. Edner, A. Sunesson, S.Svanberg, L. Vneus and S.Wallin, "Differential optical absorption spectroscopy system used for atmospheric mercury monitoring", *Applied Optics*, **25**, 403, 1986

58. J. M. C. Plane and C. F. Nien, "Differential optical absorption spectrometer for measuring atmospheric trace gases", *Review of Scientific Instruments*, **63**, 1867, 1992

59. V. P. Antonovich, Y. V. Zelyukova, I. V. Bezlutskaya and M. M. Novoselova, "Atomic Absorption Determination of Different Forms of Mercury", *Journal of Analytical Chemistry of the USSR*, **46**, 66, 1991

60. R. Ahmed and M. Stoeppler, "Deposition and Stability Studies of Methylmercury in Water Using Cold Vapor Atomic Absorption Spectrometry", *Analyst*, **111**, 1371, 1986

61. R. B. Costanzo and E. F. Barry, "Alternating Current Plasma Detector for Selective Mercury Detection in Gas Chromatography", *Analytical Chemistry*, **60**, 826, 1988